

Extended-Path Intensity Correlation: Microarcsecond Astrometry with an Arcsecond Field of View

Marios Galanis,^a Ken Van Tilburg,^{b,c} Masha Baryakhtar,^d and
Neal Weiner^b

^aPerimeter Institute for Theoretical Physics, Waterloo, Ontario N2L 2Y5, Canada

^bCenter for Cosmology and Particle Physics, Department of Physics, New York University,
New York, NY 10003, USA

^cCenter for Computational Astrophysics, Flatiron Institute, New York, NY 10010, USA

^dDepartment of Physics, University of Washington, Seattle WA 98195, USA

E-mail: mgalanis@perimeterinstitute.ca, kenvt@nyu.edu, mbaryakh@uw.edu,
neal.weiner@nyu.edu

Abstract. We develop in detail a recently proposed optical-path modification of astronomical intensity interferometers. Extended-Path Intensity Correlation (EPIC) [1] introduces a tunable path extension, enabling differential astrometry of multiple compact sources such as stars and quasars at separations of up to a few arcseconds. Combined with other recent technological advances in spectroscopy and fast single-photon detection, a ground-based intensity interferometer array can achieve microarcsecond resolution and even better light-centroiding accuracy on bright sources of magnitude $m \lesssim 15$. We lay out the theory and technical requirements of EPIC, and discuss the scientific potential. Promising applications include astrometric lensing of stars and quasar images, binary-orbit characterization, exoplanet detection, Galactic acceleration measurements and calibration of the cosmic distance ladder. The introduction of the path extension thus significantly increases the scope of intensity interferometry while reaching unprecedented levels of relative astrometric precision.

Contents

1	Introduction	2
2	Theory	5
2.1	Intensity interferometry review	7
2.1.1	General	7
2.1.2	Examples	10
2.2	Extended-path intensity correlation	11
2.2.1	General	11
2.2.2	Examples	15
2.3	Finite source size	16
2.4	Noise and light-centroiding precision	19
2.5	Atmospheric phases	23
3	Observatory Design	26
3.1	Overview	26
3.2	Observational Procedure	28
3.3	Photodetectors	30
3.4	Dispersive element	33
3.5	Tolerances	37
4	Applications	39
4.1	Binaries	40
4.2	Exoplanets	42
4.3	Accelerations	44
4.4	Stellar microlensing	48
4.5	Strongly lensed quasars	50
5	Conclusions	55
A	Notation	58
B	Derivations	61
B.1	Intensity correlation noise	61
B.2	Atmospheric aberration	63
C	Wave Optics	64
C.1	Primary and secondary mirrors	64
C.2	The EPIC optical system	66
C.3	Optical aberrations	72
C.4	Dispersive element	77

1 Introduction

Astrometry is the oldest science: the motions of celestial objects across the sky have been used for millennia to understand the cosmos and our place in it. In the present day, precision measurements of stellar velocities in our Galaxy and Local Group have provided invaluable information on galactic dynamics and structure formation. Relative velocities of stars in the central region of the Milky Way unveiled the supermassive black hole Sagittarius A*, while stellar parallax established the first rungs of the distance ladder used to discover the accelerated expansion of the Universe. In recent years, advances in astrometry have made possible the identification of isolated black holes [2–4] and exoplanets [5], discoveries of new stellar substructures [6–8], a clearer picture of the formation and evolution of the Milky Way [9], stringent tests of gravity [10–13], and searches for time-domain lensing by small dark matter halos and compact objects [14], to name but a few applications. Future measurements may reveal the gravitational potential of the Milky Way [15], constraints on dark matter substructure [16], and low-frequency gravitational waves [17–20]. These applications are enabled by the precision astrometry of space-based telescopes such as *Hipparcos* [21], *Gaia* [22], *Hubble Space Telescope (HST)* [23], and *James Webb Space Telescope (JWST)* [24], and of ground-based amplitude interferometers in the optical and radio bands such as GRAVITY at VLT [25], the Center for High Angular Resolution Astronomy (CHARA) [26], and the Event Horizon Telescope (EHT) [27, 28], which have reached light-centroiding precisions on the order of tens of microarcseconds.

These observatories are all contending with a practical obstacle: diffraction-limited resolution, approximately equal to the wavelength of light divided by the observatory’s effective size. For imaging telescopes, this size is the aperture diameter, whereas for interferometers it is the baseline distance: the separation between telescopes or receivers. Imaging telescopes can achieve a precision on the light centroid of a point source that far surpasses the angular resolution limit, as long as the exposure is sufficiently long, the point spread function (PSF) is stable, and other systematics are kept under control. In very long baseline interferometry (VLBI) in the radio band (up to millimeter wavelengths), receivers record the amplitude and phase of the electromagnetic field at different corners of the globe [28]. The data is then correlated offline, yielding information at an angular scale of tens of microarcseconds. The size of ground-based VLBI is already maximized, while shorter wavelengths present their own difficulties. Astronomical interferometers in the infrared and optical bands have to physically recombine the light from separate telescopes (since receiver electronics cannot keep track of the rapidly oscillating phase) and keep their separations stable to a fraction of wavelength, limiting their baselines to hundreds of meters at most [26, 29].

Intensity interferometry combines the best of both worlds—short wavelengths yet long baselines (with milder tolerance) and off-line correlation. The technique relies on second-order coherence: interference of the intensities, rather than the amplitudes, of incoming light, so only the photon arrival times have to be recorded and correlated. It was conceived theoretically by Hanbury Brown and Twiss in 1954 [30], who only two years later demonstrated the effect experimentally in the laboratory, using light from a mercury arc lamp [31]. Later in 1956, with a rudimentary setup and poor viewing conditions, Hanbury Brown used intensity interferometry to provide the first measurement of the 0.0063 arcsec angular diameter of Sirius [32], a spectacular initiation of a new method in observational astronomy. The program was then extended [33–36], and culminated with the Narrabri Stellar Intensity Interferometer (NSII) [37–39]. In the mid-1970s, the NSII reported the angular diameters of 32 bright

stars down to $30 \mu\text{as}$ precision [40, 41], as well as orbital parameters, masses, and line-of-sight distance of a close stellar binary system [42]. The advent of ever larger arrays of Imaging Atmospheric Cherenkov Telescopes (IACTs) [43–47] to detect high-energy gamma rays has spurred a recent revival of intensity interferometry [48–57]; in addition new fast photodetector technology has enabled the development of smaller telescope arrays with competitive sensitivity [58].

The advantages of intensity interferometry are unfortunately paired with two significant drawbacks. The first is the signal-to-noise ratio (SNR), as intensity correlations only receive contributions from “nearly coincident” photons in at least two receivers. Since the intensity of starlight typically fluctuates on femtosecond time scales, the much longer timing resolution of photon counters smears out the intensity correlations and reduces the fringe contrast; the NSII measurements were limited to very bright stars of magnitude below 3. The second limitation of traditional intensity interferometry is the extremely narrow field of view (FOV), which is naturally of the same parametric size as the angular resolution itself. The combination of the small SNR and FOV have limited astronomical intensity interferometry almost exclusively to studies of the emission morphology of isolated bright stars, and a few very closely separated multiple-star systems [42, 59].

In this work, we detail the *Extended-Path Intensity Correlation* (EPIC) observatory design which addresses both the low SNR and small FOV drawbacks of intensity interferometry [1]; a schematic of the design is shown in figure 1. We outline how recent technological advances in multichannel spectroscopic readout and fast single photon detection open up intensity interferometry to much fainter sources. The advantages of a multichannel spectroscopic readout were already known by Hanbury Brown [39], and its pairing with modern photodetectors was laid out clearly in ref. [50], which argued that one could achieve limiting R-band magnitudes of about 14. Spectroscopic splitting along with the introduction of beamsplitters to improve the sensitivity and information gathered from the telescopes was also proposed in [60, 61]. Here, we summarize further recent improvements in photodetection technology and provide a detailed quantitative description of a multichannel spectroscopic readout in the context of intensity interferometry.

To overcome the very narrow field of view, EPIC uses a tunable hardware modification to the constituent telescopes of an astronomical intensity interferometer array. This setup requires a pair of adjustable beamsplitters and mirrors that can add a differential path extension to the incoming light, thus superposing intensity fluctuations from sources at different locations on the celestial sphere [1].¹ The resulting variable path extension (and wavefront correction) dramatically widens the FOV of ground-based intensity interferometry, up to a few arcseconds, the isoplanatic angle of the atmosphere. This alteration would drastically increase the scope of intensity interferometry, enabling differential astrometry at an unprecedented precision and accuracy for a wide range of compact celestial light sources.

In section 2, we review the basic theory of intensity interferometry (section 2.1), describe the addition of the optical path extension (section 2.2), discuss typical celestial sources of finite angular extent (section 2.3), calculate the idealized signal-to-noise ratio and sensitivity (section 2.4), and calculate field of view limitations from atmospheric aberrations (section 2.5). We outline the technical requirements in section 3, including telescope design and array layout

¹A related technique called “time-delay interferometry” has been proposed previously in the context of gravitational radiation sensing with (amplitude) interferometric detectors of unequal arm lengths, where a path extension (i.e. geometric time delay) is introduced to eliminate laser phase noise [62]. Likewise, ref. [63] proposed to test quantum mechanics in photon coincidence experiments with a logically similar optical setup.

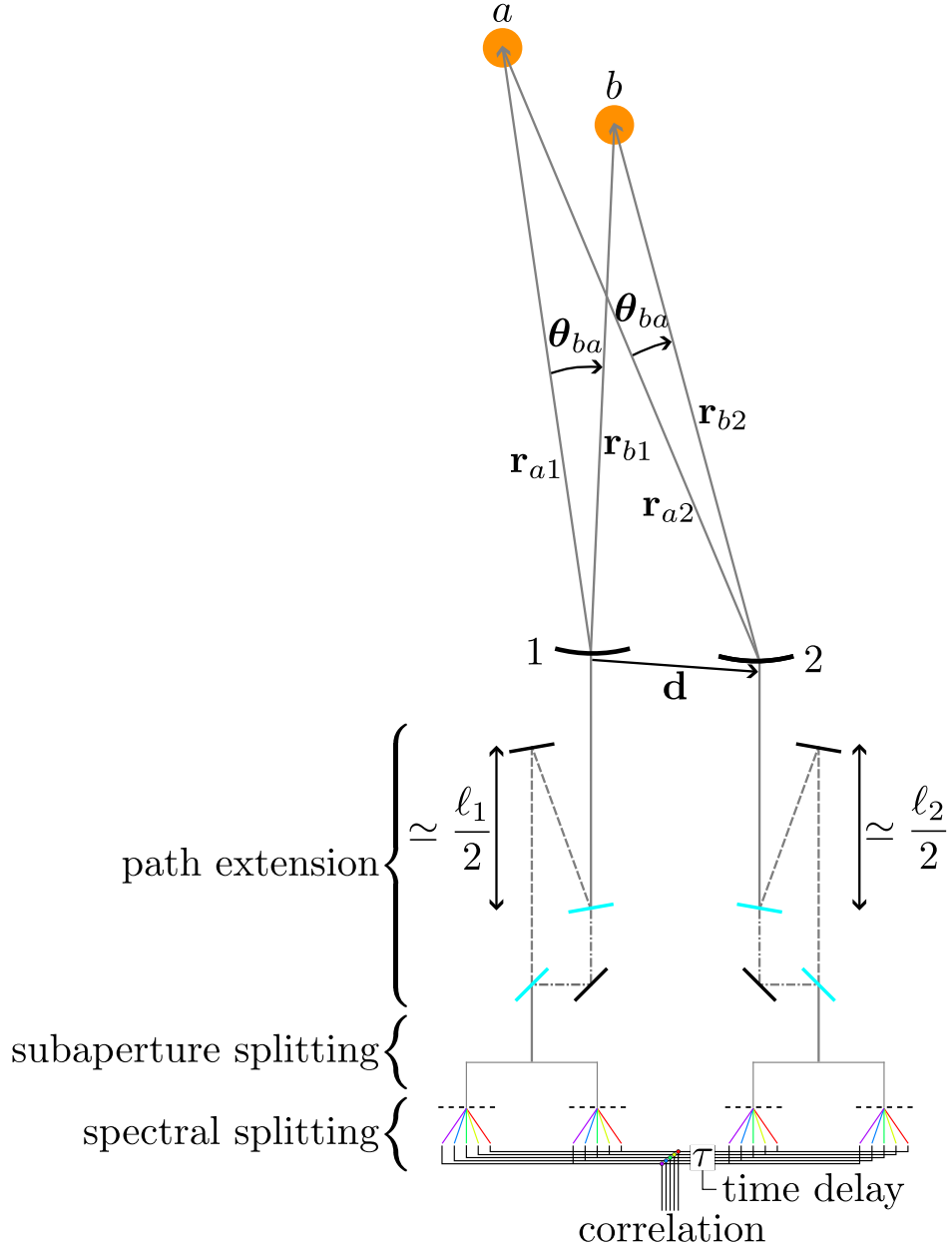


Figure 1: Diagram of an extended-path intensity correlator (EPIC). Two sources $i = a, b$ separated by an angle $\theta_{ba} = \hat{\theta}_b - \hat{\theta}_a$ are simultaneously observed by two telescopes $p = 1, 2$; the respective distances are labeled as \mathbf{r}_{ip} . In each telescope, the light from both sources is collected and collimated into the “path extension” stage, where a beamsplitter directs the light along two paths, one longer than the other by a variable amount ℓ_p , and a second beamsplitter recombines the beam. The light is then split into multiple subapertures, and a dispersive element spectrally splits the light. Ultrafast single-photon detectors record the arrival times of photons in each spectral channel, which are ultimately correlated offline after applying a time offset τ . The intensity correlations provide information on the separation θ_{ba} of the two sources as well as their angular sizes.

(section 3.1), observational procedure (section 3.2), photodetection (section 3.3), dispersive elements for spectroscopy (section 3.4), and optical tolerances (section 3.5). We propose a sample of scientific applications with EPIC in section 4: binary orbits (section 4.1), exoplanets (section 4.2), Galactic accelerations (section 4.3), stellar microlensing (section 4.4), and strongly lensed quasars (section 4.5). We conclude in section 5. The appendices contain a list of the symbols used throughout the text (appendix A), details of the derivations summarized in the text (appendix B), and a wave-optics treatment of our setup’s optical elements (appendix C).

2 Theory

The basic intensity interferometry setup consists of at least two telescopes collecting photons—and precisely recording their arrival times—from a small region of the sky. This is to be contrasted with *amplitude* interferometers, which record the electric field amplitudes as a function of time at a pair of receivers separated by a baseline \mathbf{d} . The two-point correlation function of electric field amplitudes is proportional to the “complex visibility”: the Fourier transform of the time-averaged intensity distribution of the image at angular wavenumber $\bar{k}\mathbf{d}_\perp$ conventionally decomposed into (u, v) coordinates, where \bar{k} is the mean wavenumber of the electromagnetic wave, and \mathbf{d}_\perp is the baseline vector projection perpendicular to the line of sight. Through photon collection, an *intensity* interferometer samples intensities (the square of the field amplitudes) at separate locations and compares their fluctuations. The excess correlation of the intensities $C(\mathbf{d}, \tau)$ at points separated by distance \mathbf{d} and time τ is proportional to a specific four-point function of the electromagnetic field: the square of the modulus of the complex visibility at angular wavenumber $\bar{k}\mathbf{d}_\perp$. The overall phase information is lost, which drastically degrades *global* astrometric precision, but information about relative phases is retained, thus providing excellent *differential* astrometry.

Our main new idea is to enlarge the scope (literally and figuratively) of intensity interferometry by introducing a variable, probabilistic path extension inside each constituent telescope of the intensity interferometer array while keeping the same angular resolution and light-centroiding precision. This is done by introducing additional adjustable optical elements as shown schematically in figure 2 (*left*). In a conventional intensity interferometer, the excess intensity correlation between a pair of telescopes for a point-like source at sky location $\hat{\boldsymbol{\theta}}_a$ occurs near a time offset of $\tau = -\mathbf{d} \cdot \hat{\boldsymbol{\theta}}_a / c$ with c the speed of light, depicted in figure 2 (*right*) by the black line. In an Extended-Path Intensity Correlator (EPIC), the path extension stage at telescope p splits the beam into two, one geometrically longer than the other by an amount ℓ_p . The intensity correlation fringe is thus split into 2^2 fringes, each of $1/4$ the fringe contrast, depicted as orange lines in figure 2 (*right*): the “original” fringe at $c\tau = -\mathbf{d} \cdot \hat{\boldsymbol{\theta}}_a$, one only delayed in telescope 1 at $c\tau = -\mathbf{d} \cdot \hat{\boldsymbol{\theta}}_a - \ell_1$, one only delayed in telescope 2 at $c\tau = -\mathbf{d} \cdot \hat{\boldsymbol{\theta}}_a + \ell_2$, and one delayed in both at $c\tau = -\mathbf{d} \cdot \hat{\boldsymbol{\theta}}_a + \ell_2 - \ell_1$. This procedure can be used to “superpose” the intensity correlation fringes of two sources a and b , at locations $\hat{\boldsymbol{\theta}}_a$ and $\hat{\boldsymbol{\theta}}_b$, to measure their relative angular separation $\boldsymbol{\theta}_{ba} \equiv \hat{\boldsymbol{\theta}}_b - \hat{\boldsymbol{\theta}}_a$ with extreme precision. For example, the intensity correlation fringe of source a delayed by ℓ_1 in telescope 1, and that of source b delayed by ℓ_2 in telescope 2, will coincide (and yield mutual intensity interference) when:

$$\boxed{\ell_1 + \ell_2 = \boldsymbol{\theta}_{ba} \cdot \mathbf{d}.} \quad (2.1)$$

Other permutations of fringes are also possible. In this way, the maximum angular separation for intensity interferometry can be enlarged up to the $\mathcal{O}(\text{arcsec})$ isoplanatic angle determined

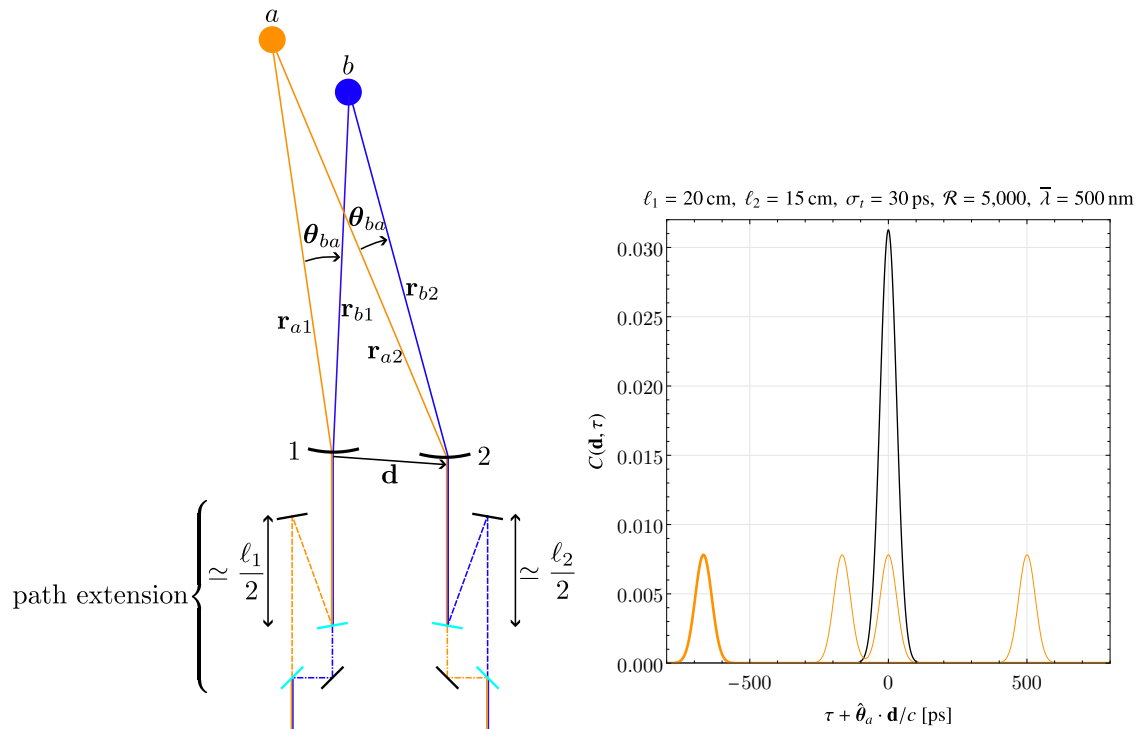


Figure 2: *Left:* Same as figure 1, but with the two-photon amplitude corresponding to the fringe in eqs. 2.25 and 2.26 color coded in the path extension stage: orange corresponds to the amplitude from source a , blue from source b . The path extensions are tuned such that $\ell_1 + \ell_2 = (r_{a2} + r_{b1}) - (r_{a1} + r_{b2}) = \boldsymbol{\theta}_{ba} \cdot \mathbf{d}$. *Right:* Excess fractional intensity correlation $C(\mathbf{d}, \tau)$ as a function timing offset τ for a single point-like source at celestial position $\hat{\boldsymbol{\theta}}_a$, for timing resolution $\sigma_t = 30$ ps, and central wavenumber $\bar{k} = 2\pi/500$ nm and spectral resolution $\mathcal{R} \equiv \bar{k}/\sigma_k = 5,000$. The black curve shows the intensity fringe of eq. 2.11 for an intensity interferometer without path extension, while the orange curve shows the four fringes of eq. 2.23 for an *extended-path* intensity correlator. The path extension retains the original main fringe at $1/4$ the contrast, but also produces three equally bright ghost fringes, as if there were 3 other images located at $\hat{\boldsymbol{\theta}}_a + \frac{\ell_1}{d} \hat{\mathbf{d}}$, $\hat{\boldsymbol{\theta}}_a - \frac{\ell_2}{d} \hat{\mathbf{d}}$, $\hat{\boldsymbol{\theta}}_a - \frac{\ell_2 - \ell_1}{d} \hat{\mathbf{d}}$, respectively. The fringe corresponding to the paths from source a shown in the *left* panel is the leftmost fringe highlighted in bold.

by atmospheric aberrations while retaining exquisite angular resolution. Hence, the dynamic range (i.e. angular separation divided by resolution) of EPIC is many orders of magnitude larger than that of traditional intensity interferometry.

In section 2.1, we present a classical description of intensity interferometry in idealized scenarios, based on but significantly extending the review of ref. [64]. More sophisticated treatments, including a quantum description and the first- and second-order coherence properties of light, can be found e.g. in ref. [65]. For a detailed review on optical stellar interferometry, see e.g. ref. [66]; for recent developments see e.g. refs. [67, 68]. In section 2.2, we describe the path extension theory of EPIC. We review basic properties of the most relevant astrophysical sources in section 2.3 in order to estimate the signal-to-noise ratio and light-centroiding precision in section 2.4. We calculate the atmospheric limitations on EPIC in section 2.5.

2.1 Intensity interferometry review

2.1.1 General

Suppose we have a single-photon detector recording a time series of photon counts impinging on a telescope. We will assume the light in the telescope is a superposition of a very large number N_θ of discrete emitters i , each emitting a large number N_k of modes α with random phases $\phi_{i\alpha}^{\text{em}}$, giving an electric field at detector p ,

$$E_p(t_p) \equiv \sum_{i=1}^{N_\theta} \sum_{\alpha=1}^{N_k} E_{i\alpha} \exp \left\{ i \left[k_\alpha (ct_p - r_{ip}) + \phi_{i\alpha}^{\text{em}} + \tilde{\phi}_{i\alpha}^{(p)}(t_p) \right] \right\} \equiv \sum_{i,\alpha} \tilde{E}_{i\alpha}^{(p)} \quad (2.2)$$

at a time t_p kept by the clock associated with each photodetector p . In the above, k_α is the wavenumber of each mode α ; $r_{ip} = |\mathbf{r}_{ip}|$ is the length of the vector $\mathbf{r}_{ip} \equiv \mathbf{r}_i - \mathbf{r}_p$ pointing from the photodetector p to the emitter i . Additional phases that may accumulate along the line of sight due to atmospheric fluctuations and telescope imperfections are denoted by $\tilde{\phi}_{i\alpha}^{(p)}(t_p)$ but will be suppressed until section 2.5 and section 3.5. As will be discussed in sections 2.5 and 3, these path-dependent phases will ultimately limit the field of view of the intensity interferometry setup and place constraints on the telescope quality. Without loss of generality, the field amplitude $E_{i\alpha}$ associated with each mode can be taken to be real; we defined the complex amplitudes $\tilde{E}_{i\alpha}^{(p)}$ in the last part of eq. 2.2 to simplify subsequent notation. Finally, we treat the field amplitudes as scalars for clarity of exposition; for unpolarized sources, intensity correlations signals are reduced by a factor of 1/2, which will be accounted for in section 2.4.

Throughout this work, we will assume that the detector separations are much smaller than the (transversely projected) separations of the sources, which are in turn taken to be much smaller than the line-of-sight distances (small angle approximation). This implies that the angular separation of two sources as observed from vantage point p ,

$$\boldsymbol{\theta}_{ij} \equiv \hat{\mathbf{r}}_{ip} - \hat{\mathbf{r}}_{jp} \simeq \hat{\boldsymbol{\theta}}_i - \hat{\boldsymbol{\theta}}_j, \quad (2.3)$$

is independent of p , and that $|\boldsymbol{\theta}_{ij}| \ll 1$. Note that this also implies that electric field magnitude $E_{i\alpha}$ is independent of p for each mode. See figure 1 for the basic geometry in the case of just two sources $i = a, b$.

The photodetectors record intensities $I_p(t_p) = \frac{1}{2}|E_p(t_p)|^2$, with expected values:

$$\langle I \rangle \equiv \langle I_p(t_p) \rangle_{\phi^{\text{em}}} = \frac{1}{2} \sum_{i,\alpha} (E_{i\alpha})^2 \rightarrow \int dk \int d\Omega \frac{dI}{dk d\Omega}, \quad (2.4)$$

where the average is taken over the emitter phases $\phi_{i\alpha}^{\text{em}}$, leaving only the ‘‘diagonal’’ terms. On the right, we have taken the continuum limit, i.e. $N_\theta, N_k \rightarrow \infty$, giving an integral over wavenumbers k and solid angle Ω over the field of view of the telescope. The expected differential intensity $\frac{dI}{dk d\Omega}$ is to be understood as a convolution of the telescope-photodetector response with the source’s intrinsic spectrum and image intensity. With our approximations and assumptions of identical photodetectors and telescopes, the intensities are independent of p . An illustration of the intensity impinging on a detector with finite time resolution is given in figure 3.

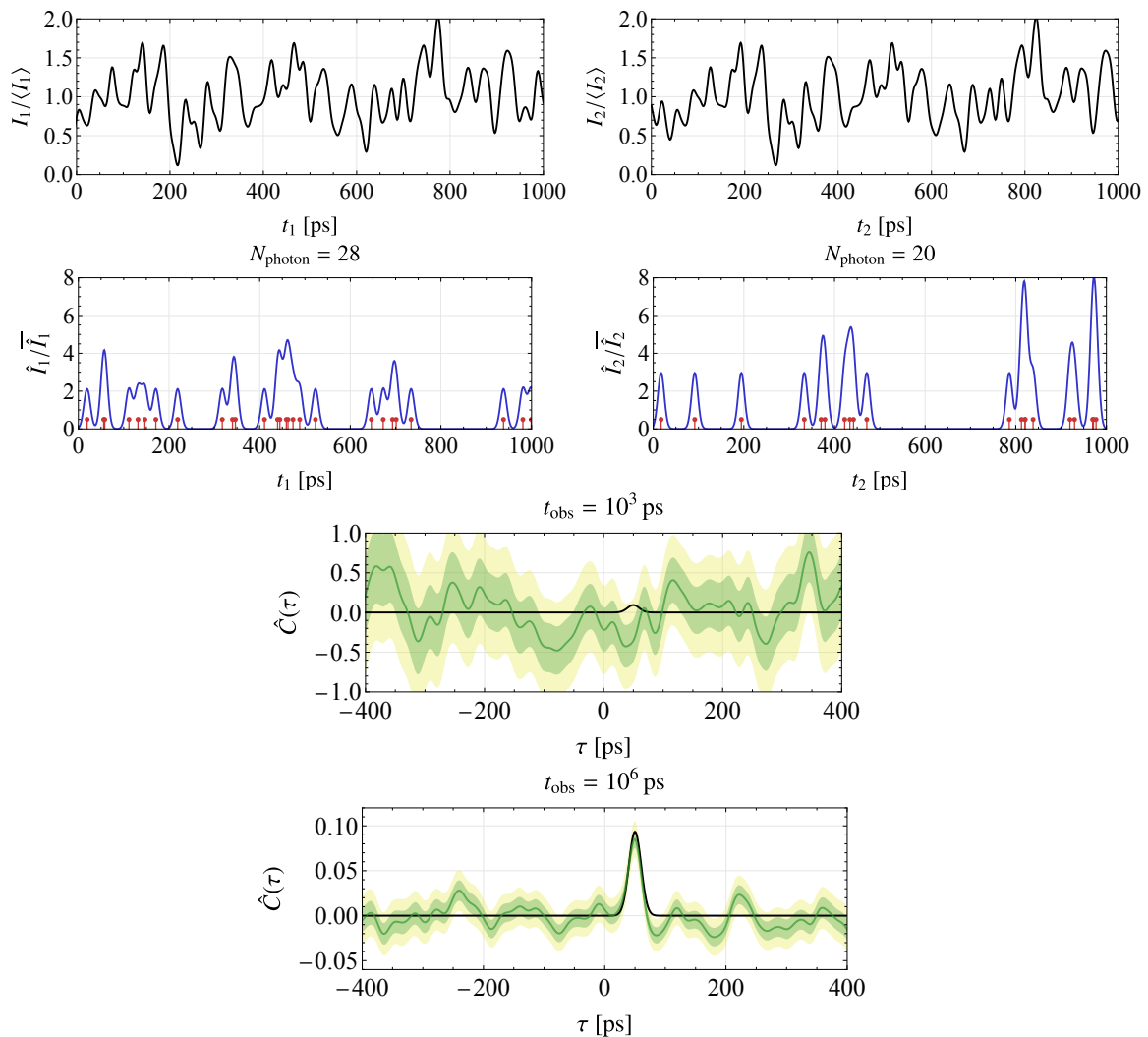


Figure 3: *First row:* Instantaneous intensity I_p normalized to the true mean intensity $\langle I_p \rangle$ from a single source as observed by two telescopes labeled $p = 1, 2$ (*left, right*), for light with a Gaussian spectrum with mean wavenumber $\bar{k} = 2\pi/500\text{ nm}$ and standard deviation $\sigma_k = \bar{k}/5000$. The true instantaneous intensity has order-unity fractional fluctuations, a coherence time of order $1/c\sigma_k$, and is *identical* in both telescopes up to a time shift of $t_2 - t_1 = 50\text{ ps}$ due to the source's wavefronts arriving earlier in telescope 1. *Second row:* Photon arrival times (red sticks) in telescope 1 (*left*) and 2 (*right*) as a function of time. The photon detection probability is directly proportional to the instantaneous intensity from the top panel(s). We plot in blue the estimated intensities \hat{I}_p (eq. 2.43) divided by their estimated time averages $\overline{\hat{I}_p}$ (cfr. eq. 2.45), assuming each telescope has a timing resolution of $\sigma_t/\sqrt{2}$ with $\sigma_t = 10\text{ ps}$. *Third Row:* Reconstructed excess fractional intensity correlation \hat{C} (green line, eq. 2.44) as a function of timing offset $\tau = t_2 - t_1$ based on the estimated intensities from the middle panels with an observation time of $t_{\text{obs}} = 10^3\text{ ps}$; green and yellow bands indicate 68% and 95% CL intervals. The true excess correlation signal $C = \langle I_1 I_2 \rangle / \langle I_1 \rangle \langle I_2 \rangle - 1$ (black) is too small to be detected. *Fourth row:* Same as in the third row, but for a much longer total observation time $t_{\text{obs}} = 10^6\text{ ps}$, whereafter the excess correlation at $\tau = 50\text{ ps}$ is detected at high significance.

The intensity correlation between two detectors $p = 1, 2$ is:

$$\begin{aligned}
\langle I_1(t_1)I_2(t_2) \rangle_{\phi^{\text{em}}} &= \frac{1}{4} \sum_{\substack{i_1, j_1 \\ i_2, j_2}} \sum_{\substack{\alpha_1, \beta_1 \\ \alpha_2, \beta_2}} \tilde{E}_{i_1 \alpha_1}^{(1)} \tilde{E}_{j_1 \beta_1}^{(1)*} \tilde{E}_{i_2 \alpha_2}^{(2)} \tilde{E}_{j_2 \beta_2}^{(2)*} \\
&= \left(\frac{1}{2} \sum_{i, \alpha} (E_{i\alpha})^2 \right)^2 + \left| \frac{1}{2} \sum_{i, \alpha} \tilde{E}_{i\alpha}^{(1)} \tilde{E}_{i\alpha}^{(2)*} \right|^2 - \frac{1}{4} \sum_{i, \alpha} (E_{i\alpha})^4 \\
&\rightarrow \langle I_1 \rangle \langle I_2 \rangle + \left| \int dk \int d\Omega \frac{dI}{dk d\Omega} e^{i[ck(t_1-t_2)-k\hat{\theta}\cdot\mathbf{d}]} \right|^2.
\end{aligned} \tag{2.5}$$

For the first term in the second line, we have kept only “diagonal” terms from the first line with $i_1 = j_1, i_2 = j_2, \alpha_1 = \beta_1$, and $\alpha_2 = \beta_2$. For the second term, we kept “off-diagonal terms” with $i_1 = j_2, \alpha_1 = \beta_2, i_2 = j_1$, and $\alpha_2 = \beta_1$. The third term of the second line subtracts off terms that we overcounted, but this is a negligible contribution in the continuum limit taken in the third line of eq. 2.5. The second term in the third line can be recognized as the modulus-squared of the complex visibility function. We also introduced the baseline vector \mathbf{d} , leading to a difference in propagation distance $r_{i_2} - r_{i_1}$ to the two photodetectors:

$$\mathbf{d} \equiv \mathbf{r}_2 - \mathbf{r}_1 = -\mathbf{r}_{i_2} + \mathbf{r}_{i_1}; \quad r_{i_2} - r_{i_1} = -\hat{\theta}_i \cdot \mathbf{d}, \tag{2.6}$$

with the latter relation holding for all sources i .

We can write the “excess fractional intensity correlation” (relative to random chance) as:

$$\begin{aligned}
C(\mathbf{d}, \tau) &\equiv \frac{\langle I_1(t)I_2(t+\tau) \rangle}{\langle I_1 \rangle \langle I_2 \rangle} - 1 \\
&= \int \frac{d^2b_1}{A_1} \int \frac{d^2b_2}{A_2} \int \frac{d(\Delta t)}{\sqrt{2\pi}\sigma_t} e^{-\frac{(\Delta t)^2}{2\sigma_t^2}} \times \left| \int dk \int d\Omega \frac{d\tilde{I}}{dk d\Omega} e^{i[k(c(\Delta t-\tau)-\hat{\theta}\cdot(\mathbf{d}+\Delta\mathbf{b}))]} \right|^2,
\end{aligned} \tag{2.7}$$

with $d\tilde{I} \equiv dI/\langle I \rangle$, shown for the example of a single source in figure 3. In the second line of eq. 2.7, we have introduced two “averaging kernels” over \mathbf{b}_1 and \mathbf{b}_2 that take into account the finite aperture sizes A_1 and A_2 of the telescopes associated with photodetectors 1 and 2, effectively smearing out the baseline \mathbf{d} between the centers of the telescopes by an amount $\Delta\mathbf{b} \equiv \mathbf{b}_2 - \mathbf{b}_1$ for each pair of points \mathbf{b}_1 and \mathbf{b}_2 on the respective telescopes’ apertures. A third averaging kernel over Δt takes into account the relative timing error of the clocks associated with photodetectors 1 and 2, around their mean offset of $\tau \equiv t_2 - t_1$. Its timing spread σ_t is

$$\sigma_t^2 = \sigma_{t_{\text{res},1}}^2 + \sigma_{t_{\text{res},2}}^2 + \sigma_{t_{\text{sync}}}^2, \tag{2.8}$$

the (quadrature) sum of the respective timing resolutions and the relative synchronization error $\sigma_{t_{\text{sync}}}$.

For a sufficiently narrow frequency spectrum around $k = \bar{k}$, and with negligible smearing and phase noise, the excess correlation of eq. 2.7 is proportional to the *square modulus of the Fourier transform of the image*, at an angular wavevector of $k\mathbf{d}_\perp$, thus providing a fiducial angular resolution

$$\sigma_{\theta_{\text{res}}} \equiv \frac{1}{\bar{k}d} = \frac{\bar{\lambda}}{2\pi d} \approx \underbrace{7.96 \times 10^{-12} \text{ rad}}_{1.64 \mu\text{as}} \left(\frac{\bar{\lambda}}{500 \text{ nm}} \right) \left(\frac{10 \text{ km}}{d} \right). \tag{2.9}$$

in the direction parallel to $\mathbf{d}_\perp \equiv \mathbf{d}(1 - \hat{\mathbf{d}} \cdot \hat{\boldsymbol{\theta}})$ (with $\hat{\boldsymbol{\theta}}$ the location of the light centroid of the image). This resolution is much better than that of very-long-baseline amplitude interferometry in the radio band (e.g. EHT [28]) at much longer wavelengths (typically $\lambda \sim 1$ mm), and than that of optical/infrared Michelson interferometry (e.g. Keck [29], CHARA [26], GRAVITY [69]) which is restricted to much shorter baselines ($d \lesssim 300$ m) because the light from both apertures needs to be physically recombined. With intensity interferometry, the correlation can be computed offline, and the detectors can in principle be placed at opposite sides of the Earth. However, as we shall see in sections 2.3 and 2.4, for $d \gg 10$ km and naively even better angular resolution, the excess correlation will be suppressed because all sufficiently bright sources for intensity interferometry have an angular size larger than 10^{-12} rad, so the fiducial estimate of eq. 2.9 is (practically) a best-case scenario.

2.1.2 Examples

Before we move on to extended-path intensity correlation (EPIC) in section 2.2, it is instructive to consider a handful of examples to gain intuition about intensity interferometry and to understand its limitation without the path extension.

The simplest example is that of a single point-like source a at a location $\hat{\boldsymbol{\theta}}_a$ on the celestial sphere with a narrow gaussian spectrum of width σ_k around a mean wavenumber \bar{k} :

$$\frac{dI}{dk d\Omega} = \frac{I(\bar{k})}{\sqrt{2\pi}\sigma_k} e^{-\frac{(k-\bar{k})^2}{2\sigma_k^2}} \delta^2(\hat{\boldsymbol{\theta}} - \hat{\boldsymbol{\theta}}_a). \quad (2.10)$$

Assuming that the planes of the apertures are oriented (sufficiently) perpendicular to the location of the source, i.e. $|\mathbf{b}_p \cdot \hat{\boldsymbol{\theta}}_a| \ll c\sigma_t$, the aperture smearing can be ignored, and we find after evaluating eq. 2.7:

$$\begin{aligned} C(\mathbf{d}, \tau) &= \int d(\Delta t) \frac{1}{\sqrt{2\pi}\sigma_t} e^{-\frac{(\Delta t)^2}{2\sigma_t^2}} \left| \exp \left\{ i\bar{k} \left(c(\Delta t - \tau) - \hat{\boldsymbol{\theta}}_a \cdot \mathbf{d} \right) - \frac{\sigma_k^2}{2} \left(c(\Delta t - \tau) - \hat{\boldsymbol{\theta}}_a \cdot \mathbf{d} \right)^2 \right\} \right|^2 \\ &= \frac{1}{\sqrt{1 + 2c^2\sigma_k^2\sigma_t^2}} \exp \left\{ -\frac{\sigma_k^2}{1 + 2c^2\sigma_k^2\sigma_t^2} \left(c\tau + \hat{\boldsymbol{\theta}}_a \cdot \mathbf{d} \right)^2 \right\}. \end{aligned} \quad (2.11)$$

Thus, we find that the intensity fluctuations at the two photodetectors are maximally correlated as long as the timing offset is chosen to be $\tau \simeq -\hat{\boldsymbol{\theta}}_a \cdot \mathbf{d}/c$, commensurate to the differential wavefront arrival time at both photodetectors. Practically, the coherence time of the light is significantly shorter than the relative timing precision, so $c\sigma_k\sigma_t \gg 1$, as we will discuss in section 2.4. Hence, the offset τ needs to be chosen around its optimal value to a precision of σ_t or better, which then produces a maximal intensity correlation of $C(\mathbf{d}, \tau = -\hat{\boldsymbol{\theta}}_a \cdot \mathbf{d}/c) \simeq 1/(\sqrt{2}c\sigma_k\sigma_t)$.

For our next example, let us take two point-like sources a and b at locations $\hat{\boldsymbol{\theta}}_a$ and $\hat{\boldsymbol{\theta}}_b$ with total flux $\langle I \rangle = I(\bar{k})$ and fractional fluxes \tilde{I}_a and \tilde{I}_b (by construction, $\tilde{I}_a + \tilde{I}_b = 1$):

$$\frac{d\tilde{I}}{dk d\Omega} = \frac{1}{\sqrt{2\pi}\sigma_k} e^{-\frac{(k-\bar{k})^2}{2\sigma_k^2}} \left[\sum_{i=a,b} \tilde{I}_i \delta^2(\hat{\boldsymbol{\theta}} - \hat{\boldsymbol{\theta}}_i) \right]. \quad (2.12)$$

We will again neglect the finite aperture spread, despite the fact that $\hat{\boldsymbol{\theta}}_i \cdot \mathbf{b}_p = 0$ cannot be maintained for both sources simultaneously, as more severe suppression effects will typically

kick in for $\boldsymbol{\theta}_{ba} \equiv \hat{\boldsymbol{\theta}}_b - \hat{\boldsymbol{\theta}}_a \neq 0$. We evaluate eq. 2.7:

$$\begin{aligned}
C(\mathbf{d}, \tau) &= \int d(\Delta t) \frac{1}{\sqrt{2\pi}\sigma_t} e^{-\frac{(\Delta t)^2}{2\sigma_t^2}} \left| \sum_{i=a,b} \tilde{I}_i e^{i\bar{k}(c(\Delta t - \tau) - \hat{\boldsymbol{\theta}}_i \cdot \mathbf{d}) - \frac{\sigma_k^2}{2}(c(\Delta t - \tau) - \hat{\boldsymbol{\theta}}_i \cdot \mathbf{d})^2} \right|^2 \\
&= \frac{1}{\sqrt{1 + 2c^2\sigma_k^2\sigma_t^2}} \left\{ \tilde{I}_a^2 e^{-\frac{\sigma_k^2}{1+2c^2\sigma_k^2\sigma_t^2}(c\tau + \hat{\boldsymbol{\theta}}_a \cdot \mathbf{d})^2} + \tilde{I}_b^2 e^{-\frac{\sigma_k^2}{1+2c^2\sigma_k^2\sigma_t^2}(c\tau + \hat{\boldsymbol{\theta}}_b \cdot \mathbf{d})^2} \right. \\
&\quad \left. + 2\tilde{I}_a\tilde{I}_b \cos[\bar{k}\mathbf{d} \cdot \boldsymbol{\theta}_{ba}] e^{-\sigma_k^2(\boldsymbol{\theta}_{ba} \cdot \mathbf{d})^2/4} e^{-\frac{\sigma_k^2}{1+2c^2\sigma_k^2\sigma_t^2}[c\tau + (\hat{\boldsymbol{\theta}}_a + \hat{\boldsymbol{\theta}}_b) \cdot \mathbf{d}/2]^2} \right\} \quad (2.13)
\end{aligned}$$

The generalization of eq. 2.13 to an arbitrary number of point-like sources is straightforward and has a similar form.

We find that the excess correlation of eq. 2.13 has ‘‘one-source’’ contributions, proportional to \tilde{I}_i^2 , of exactly the same functional form as in eq. 2.11. The last line of eq. 2.13 contains the ‘‘two-source’’ contribution, proportional to $\tilde{I}_a\tilde{I}_b$. This is the term most sensitive to the separation of the sources, as it contains the most rapidly varying phase, namely $\bar{k}\mathbf{d} \cdot \boldsymbol{\theta}_{ba}$ in the cosine argument. The two-source contribution is maximized when the timing offset is taken to be $\tau = \tau^{\text{opt}} = -(\hat{\boldsymbol{\theta}}_a + \hat{\boldsymbol{\theta}}_b) \cdot \mathbf{d}/2c$, and we find in the limit $c\sigma_k\sigma_t \gg 1$:

$$C^{\text{opt}}(\mathbf{d}) = \frac{1}{\sqrt{2}c\sigma_k\sigma_t} \left\{ (\tilde{I}_a^2 + \tilde{I}_b^2) e^{-\frac{(\boldsymbol{\theta}_{ba} \cdot \mathbf{d})^2}{8\sigma_t^2}} + 2\tilde{I}_a\tilde{I}_b \cos[\bar{k}\mathbf{d} \cdot \boldsymbol{\theta}_{ba}] e^{-\frac{\sigma_k^2(\boldsymbol{\theta}_{ba} \cdot \mathbf{d})^2}{4}} \right\}. \quad (2.14)$$

In the above eq. 2.14, we recognize three angular scales. The first and smallest is the angular resolution scale $\sigma_{\theta_{\text{res}}} = 1/\bar{k}d$ from eq. 2.9, which sets the fringe separation and thus determines the angular resolution on $\boldsymbol{\theta}_{ba} \cdot \hat{\mathbf{d}}$. The second angular scale is

$$\sigma_{\Delta\theta} = \frac{\sqrt{2}}{\sigma_k d} \approx \underbrace{5.63 \times 10^{-8} \text{ rad}}_{11.6 \text{ mas}} \left(\frac{\bar{k}/\sigma_k}{1,000} \right) \left(\frac{\bar{\lambda}}{500 \text{ nm}} \right) \left(\frac{10 \text{ km}}{d} \right), \quad (2.15)$$

which sets the dynamical range for $\boldsymbol{\theta}_{ba} \cdot \hat{\mathbf{d}}$ over which the fringes are not exponentially suppressed, i.e. the effective field of view. The third and typically largest angular scale is:

$$\sigma_{\hat{\boldsymbol{\theta}}} = \frac{2c\sigma_t}{d} \approx \underbrace{6.00 \times 10^{-7} \text{ rad}}_{124 \text{ mas}} \left(\frac{\sigma_t}{10 \text{ ps}} \right) \left(\frac{10 \text{ km}}{d} \right), \quad (2.16)$$

which determines the fiducial, *global* astrometric precision on $\hat{\boldsymbol{\theta}}_i \cdot \hat{\mathbf{d}}$ from the ‘‘one-source’’ contributions to the excess intensity correlation, independent of any pairwise angular separations $\boldsymbol{\theta}_{ij}$. In figure 4, we plot the excess correlation of eq. 2.14 for two equally bright sources, and indicate the three angular scales from eqs. 2.9, 2.15, and 2.16 for some representative parameters.

2.2 Extended-path intensity correlation

2.2.1 General

The limited (angular) dynamic range of intensity interferometry severely limits its use for differential astrometric measurements. If one wants to harness the full resolving power at

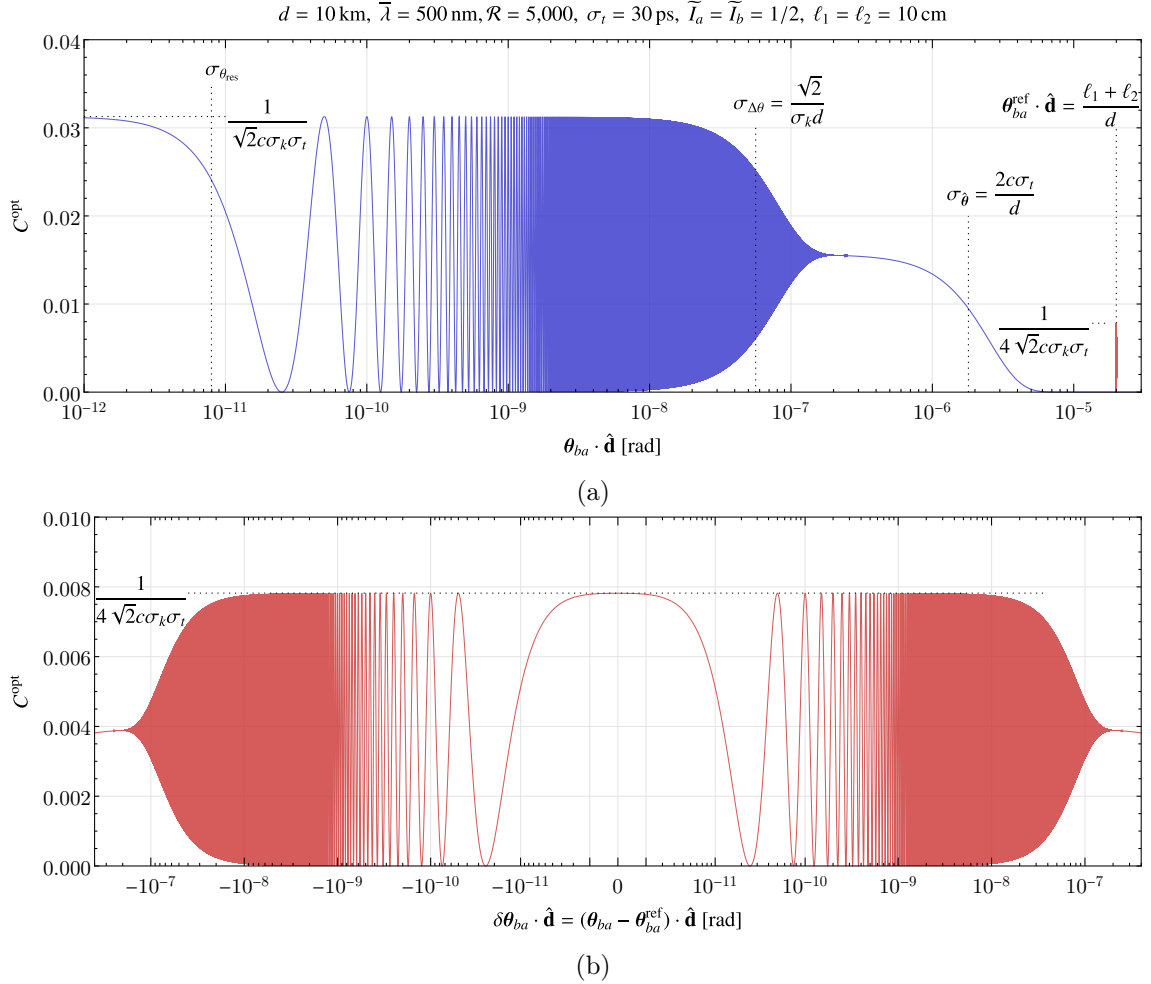


Figure 4: Excess correlation $C^{\text{opt}}(\mathbf{d})$ as a function of $\boldsymbol{\theta}_{ba} \cdot \hat{\mathbf{d}}$ for fiducial parameters of the baseline separation $d = 10 \text{ km}$, mean wavenumber $\bar{k} = 2\pi/500 \text{ nm}$ of the light, and relative timing precision $\sigma_t = 30 \text{ ps}$, for two equally bright sources: $\tilde{I}_a = \tilde{I}_b = 1/2$. The blue curve in figure 4a is eq. 2.14 for intensity interferometry *without* any path extension. The red curve (spike) in figure 4a is the excess correlation of eq. 2.28 for EPIC, with the same parameters but including geometric delays of $\ell_1 = \ell_2 = 10 \text{ cm}$, producing a ghost intensity correlation fringe of 1/4 the contrast at a reference angle $\boldsymbol{\theta}_{ba}^{\text{ref}} \cdot \hat{\mathbf{d}} = 2 \times 10^{-5} \text{ rad}$, but otherwise identical to the main fringe. A zoom-in of this ghost fringe around $\boldsymbol{\theta}_{ba} \approx \boldsymbol{\theta}_{ba}^{\text{ref}}$ is shown in figure 4b. The characteristic scales for angular resolution $\sigma_{\theta_{\text{res}}}$ (eq. 2.9), dynamic field of view $\sigma_{\Delta\theta}$ (eq. 2.15), and global astrometric precision $\sigma_{\hat{\theta}}$ (eq. 2.16) are also indicated.

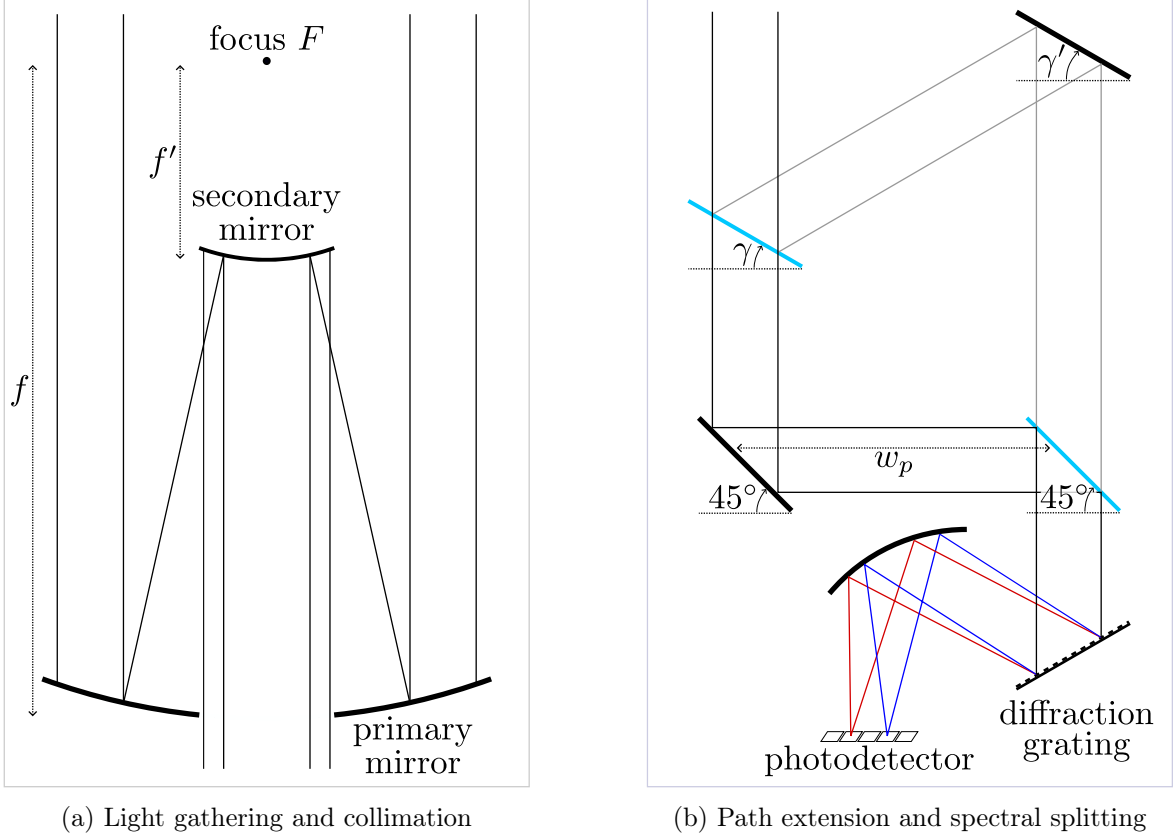


Figure 5: Schematic optical path for the path extension in a single telescope of an extended-path intensity correlator. Panel 5a: Light from a compact source is collected by a large primary mirror with focal length f , and collimated down to a narrow beam by a secondary mirror with focal length f' sharing the same focal point F as the primary. (Actual setups may have several foci, and a slit near a real pupil to select light only from the source of interest.) Panel 5b: A semi-transparent flat plate whose normal is at an angle γ relative to the collimated beam, splits the light into two optical paths (gray and black) of different path lengths (for $\gamma \simeq \gamma' \neq 45^\circ$) but undistorted wavefronts (for $\gamma = \gamma'$). The paths are recombined by another semi-transparent plate, after which the collimated beam is spectrally split by a reflective diffraction grating, and focused onto a photodetector whose pixels are read out as different spectral channels.

a resolution $\sigma_{\theta_{\text{res}}} \sim \mathcal{O}(1 \mu\text{as})$ (see eq. 2.9), the effective field of view is also tiny, of order $\sigma_{\Delta\theta} \lesssim \mathcal{O}(10 \text{ mas})$ if one has no more than $\bar{k}/\sigma_k \sim 10^4$ fringes (see eq. 2.15), which is already restrictive on the spectral width. Very few bright sources, other than tight binaries, are expected have such small relative separations. Furthermore, it is practically difficult to discriminate between the n^{th} fringe and the $(n \pm 1)^{\text{th}}$ fringe for large $n \sim kd \cdot \theta_{ba}/2\pi \gg 1$.

EPIC solves this small-separation problem, and allows for effective fields of view on the order of a *few arcseconds*. It is accomplished by modifying the optical path in at least one of the telescopes by introducing a differential path extension illustrated in figure 5. Light from the source(s) impinges on the telescope's large primary mirror (with collecting area A_p), and is then re-collimated to a narrow beam (figure 5a). This collimated light then enters the path-extension stage (top half of figure 5b), where the beam is split and recombined by a pair

of partially reflective plates, with electric-field reflectivity and transmission of ϵ and $\sqrt{1 - \epsilon^2}$, respectively. For $\gamma = \gamma'$, the two paths have a differential geometric path length of:

$$\ell_p = \frac{w_p}{\sin 2\gamma} (1 + \cos 2\gamma - \sin 2\gamma) \quad \text{for } 0 < \gamma < \pi/2, \quad (2.17)$$

which can be positive ($\gamma < \pi/4$) or negative ($\gamma > \pi/4$). It will be advantageous to have γ' deviate slightly from γ , as discussed around eqs. 2.25 and 2.26. After the path-extension stage, the light is spectrally split (bottom half of right panel), and focused onto a photodetector array, whose individual pixels each read out one spectral channel, centered at some wavenumber \bar{k} with narrow bandwidth σ_k . We discuss photodetector capabilities in section 3.3 and spectroscopic elements in section 3.4.

In such a setup, with optical losses and plate thicknesses ignored, the electric field as seen at the location of (a single pixel of) photodetector p is:

$$E_p(t_p) = \epsilon \sqrt{1 - \epsilon^2} \sum_{i=1}^{N_\theta} \sum_{\alpha=1}^{N_k} \sum_{n=0}^1 e^{-ink_\alpha \ell_p} E_{i\alpha} \exp \{i [k_\alpha (t_p - r_{ip}) + \phi_{i\alpha}^{\text{em}}]\}, \quad (2.18)$$

where $n = 0$ corresponds to the “left path” in figure 5b, and $n = 1$ to the “right path”, which have a differential geometric propagation phase due to their difference in length by ℓ_p from eq. 2.17. The expected intensity calculation proceeds exactly as in eq. 2.4, and becomes in the continuum limit:

$$\langle I_p(t_p) \rangle = 2\epsilon^2 (1 - \epsilon^2) \int dk \int d\Omega \frac{dI}{dk d\Omega} (1 + \cos k\ell_p). \quad (2.19)$$

The latter factor $(1 + \cos k\ell_p)$ is due to interference of the left and right paths: it is maximal when the ℓ_p is an integer number of wavelengths, and vanishes when ℓ_p is a half-integer number of wavelengths (corresponding to when the photodetector is at the “dark port” of the internal interferometer). The calculation of the intensity correlation is analogous to that of eq. 2.5, with the addition of a $\epsilon \sqrt{1 - \epsilon^2} (1 + e^{-ik\ell_p})$ factor for every electric field E_p :

$$\begin{aligned} \langle I_1(t_1) I_2(t_2) \rangle &= \langle I_1 \rangle \langle I_2 \rangle + \epsilon^4 (1 - \epsilon^2)^2 \\ &\times \left| \int dk \int d\Omega \frac{dI}{dk d\Omega} (1 + e^{-ik\ell_1}) (1 + e^{ik\ell_2}) e^{ik((t_1 - t_2) - \hat{\theta} \cdot \mathbf{d})} \right|^2. \end{aligned} \quad (2.20)$$

Putting together eqs. 2.7, 2.19, and 2.20, and including aperture smearing and finite relative timing resolution effects, thus yields the excess fractional intensity correlation:

$$\begin{aligned} C(\mathbf{d}, \tau) &= \frac{\epsilon^4 (1 - \epsilon^2)^2}{\langle I_1 \rangle \langle I_2 \rangle} \int \frac{d^2 b_1}{A_1} \int \frac{d^2 b_2}{A_2} \int d(\Delta t) \frac{1}{\sqrt{2\pi\sigma_t}} e^{\frac{-(\Delta t)^2}{2\sigma_t^2}} \\ &\times \left| \int dk \int d\Omega \frac{dI}{dk d\Omega} (1 + e^{-ik\ell_1}) (1 + e^{ik\ell_2}) e^{ik(c(\Delta t - \tau) - \hat{\theta} \cdot (\mathbf{d} + \Delta \mathbf{b}))} \right|^2. \end{aligned} \quad (2.21)$$

Equation 2.21 is the central formula for extended-path intensity correlation.

2.2.2 Examples

To understand the consequences of the path extension in eq. 2.21, let us again consider a single point source with a differential intensity distribution from eq. 2.10. The effective transmitted intensity at each telescope is, from eq. 2.19:

$$\langle I_p \rangle = 2\epsilon^2(1 - \epsilon^2)I(\bar{k}) \left[1 + e^{-\sigma_k^2 \ell_p^2 / 2} \cos \bar{k} \ell_p \right] \simeq 2\epsilon^2(1 - \epsilon^2)I(\bar{k}). \quad (2.22)$$

As we will see shortly, to effectively increase the field of view EPIC beyond that of conventional intensity interferometry, it is necessary to take $\sigma_k \ell \gg 1$, so that the last approximation in eq. 2.22 will hold to high precision. The excess intensity correlation for this source can be calculated from eq. 2.20, with the same approximation and with apertures perpendicular to the line of sight ($\hat{\boldsymbol{\theta}}_a \cdot \mathbf{b}_p$):

$$C(\mathbf{d}, \tau) \simeq \frac{e^{-\frac{\sigma_k^2 (c\tau + \hat{\boldsymbol{\theta}}_a \cdot \mathbf{d})^2}{1 + 2c^2 \sigma_k^2 \sigma_t^2}} + e^{-\frac{\sigma_k^2 (c\tau + \hat{\boldsymbol{\theta}}_a \cdot \mathbf{d} + \ell_1)^2}{1 + 2c^2 \sigma_k^2 \sigma_t^2}} + e^{-\frac{\sigma_k^2 (c\tau + \hat{\boldsymbol{\theta}}_a \cdot \mathbf{d} - \ell_2)^2}{1 + 2c^2 \sigma_k^2 \sigma_t^2}} + e^{-\frac{\sigma_k^2 (c\tau + \hat{\boldsymbol{\theta}}_a \cdot \mathbf{d} - \ell_2 + \ell_1)^2}{1 + 2c^2 \sigma_k^2 \sigma_t^2}}}{4\sqrt{1 + 2c^2 \sigma_k^2 \sigma_t^2}}. \quad (2.23)$$

Comparing eqs. 2.11 and 2.23, or the black and orange curves in figure 2, we can see that the effect of the path extension is to reduce the contrast of the “main” intensity fringe, at $c\tau \simeq -\hat{\boldsymbol{\theta}} \cdot \mathbf{d}$, by a factor of 4. More importantly, however, the initial fringe is now also split into four, including three other equally bright “ghost fringes”, as if there were three duplicate images of the source at locations $\hat{\boldsymbol{\theta}}_a^{\text{ghost}} = \hat{\boldsymbol{\theta}}_a + \frac{\{\ell_1, -\ell_2, -\ell_2 + \ell_1\}}{d} \hat{\mathbf{d}}$, respectively. When $\sigma_k \ell_p \gg 1$, these ghost fringes are far outside the effective field of view (relative to the main fringe) of regular intensity interferometry (cfr. eq. 2.15).

With the behavior of the extended-path intensity correlator understood for a single point source, let us see what the excess intensity correlator looks like for two point sources under influence of the path extension; evaluation of the fractional intensity correlation formula of eq. 2.20 for the two sources of eq. 2.12 gives:

$$C(\mathbf{d}, \tau) = \frac{1}{4\sqrt{1 + 2c^2 \sigma_k^2 \sigma_t^2}} \int \frac{d^2 b_1}{A_1} \int \frac{d^2 b_2}{A_2} \left\{ \sum_{i=a,b} \tilde{I}_i^2 \sum_{\ell} e^{\frac{-\sigma_k^2}{1 + 2c^2 \sigma_k^2 \sigma_t^2} [c\tau + \hat{\boldsymbol{\theta}}_i \cdot (\mathbf{d} + \Delta \mathbf{b}) + \ell]^2} \right. \quad (2.24)$$

$$\left. + 2\tilde{I}_a \tilde{I}_b \sum_{\ell, \ell'} \cos [\bar{k} ((\mathbf{d} + \Delta \mathbf{b}) \cdot \boldsymbol{\theta}_{ba} - \ell + \ell')] e^{\frac{-\sigma_k^2}{4} [\boldsymbol{\theta}_{ba} \cdot (\mathbf{d} + \Delta \mathbf{b}) - \ell + \ell']^2} e^{\frac{-\sigma_k^2 \left[c\tau + \frac{\hat{\boldsymbol{\theta}}_a + \hat{\boldsymbol{\theta}}_b}{2} \cdot (\mathbf{d} + \Delta \mathbf{b}) + \frac{\ell + \ell'}{2} \right]^2}{1 + 2c^2 \sigma_k^2 \sigma_t^2}} \right\}.$$

Each sum over ℓ and ℓ' runs over the list $\{0, \ell_1, -\ell_2, -\ell_2 + \ell_1\}$ with ℓ_1 and ℓ_2 as in eq. 2.17. The possibilities for ℓ correspond to whether the light from source a is extended nowhere, in telescope 1 only, in telescope 2 only, or in both telescopes, respectively; ℓ' runs over the same possibilities for source b . For $\boldsymbol{\theta}_{ba} \cdot \hat{\mathbf{d}} \gg \sigma_{\Delta\theta} \equiv \sqrt{2}/\sigma_k d$, the “main” differential astrometry fringe between sources a and b (corresponding to $\ell = \ell' = 0$), or really any fringe with $\sigma_k |\boldsymbol{\theta}_{ba} \cdot \mathbf{d} - \ell + \ell'| \gg 1$, is exponentially suppressed (see eq. 2.15 and figure 2).

However, even when the separation between the main images of the source is large, the apparent separation between their respective ghost images need not be. By tuning $\ell - \ell' \simeq \boldsymbol{\theta}_{ba} \cdot \hat{\mathbf{d}}$, we can overcome the field-of-view limitation of intensity interferometry. Furthermore, by making ℓ_p depend on \mathbf{b}_p , for example by a slight tilting of one of the mirrors ($\gamma \neq \gamma'$),

aperture smearing effects can be negated completely. The optimal geometric path extensions for differential astrometry with EPIC are achieved at e.g. $\ell = +\ell_1^{\text{opt}}$ and $\ell' = -\ell_2^{\text{opt}}$ with:

$$\ell_1^{\text{opt}}(\mathbf{b}_1) = \boldsymbol{\theta}_{ba}^{\text{ref}} \cdot [\rho \mathbf{d} - \mathbf{b}_1], \quad (2.25)$$

$$\ell_2^{\text{opt}}(\mathbf{b}_2) = \boldsymbol{\theta}_{ba}^{\text{ref}} \cdot [(1 - \rho) \mathbf{d} + \mathbf{b}_2]; \quad (2.26)$$

where ρ is arbitrary, and other fringe combinations of ℓ and ℓ' are also possible. This particular fringe corresponds to the amplitude depicted in figure 2. The reference separation vector $\boldsymbol{\theta}_{ba}^{\text{ref}}$ should be chosen close to the actual separation, i.e. $\delta \boldsymbol{\theta}_{ba} \equiv \boldsymbol{\theta}_{ba} - \boldsymbol{\theta}_{ba}^{\text{ref}}$ has length much less than $\sigma_{\Delta\theta}$. For maximum sensitivity, one should choose the optimal timing offset $\tau = \tau^{\text{opt}}$ that maximizes the differential astrometry fringe:

$$\tau^{\text{opt}} = -\frac{\hat{\boldsymbol{\theta}}_a + \hat{\boldsymbol{\theta}}_b - (1 - 2\rho)\boldsymbol{\theta}_{ba}^{\text{ref}}}{2} \cdot \frac{\mathbf{d}}{c}. \quad (2.27)$$

Finally, we obtain the excess fractional intensity correlation for two point sources in this optimal configuration:

$$C^{\text{opt}}(\mathbf{d}) \simeq \frac{1}{4\sqrt{2}c\sigma_k\sigma_t} \left\{ \tilde{I}_a^2 + \tilde{I}_b^2 + 2\tilde{I}_a\tilde{I}_b \cos[\bar{k}\mathbf{d} \cdot \delta\boldsymbol{\theta}_{ba}] e^{-\frac{\sigma_k^2}{4}(\mathbf{d} \cdot \delta\boldsymbol{\theta}_{ba})^2} \right\}. \quad (2.28)$$

The utility of EPIC is apparent upon comparison of eqs. 2.14 and 2.28. Without the path extension, the two-source fringes are only visible for an ultra-narrow field: $|\boldsymbol{\theta}_{ba} \cdot \hat{\mathbf{d}}| \lesssim \sigma_{\Delta\theta}$. With the path extension, the two-source fringes are visible whenever $|\delta\boldsymbol{\theta}_{ba} \cdot \hat{\mathbf{d}}| \lesssim \sigma_{\Delta\theta}$. In other words, the dynamic range has not increased, but instead of the usable field of view being centered around the locus where $\boldsymbol{\theta}_{ba} \cdot \hat{\mathbf{d}} \approx 0$, it is centered around $\boldsymbol{\theta}_{ba} \cdot \hat{\mathbf{d}} \approx \boldsymbol{\theta}_{ba}^{\text{ref}} \cdot \hat{\mathbf{d}} = \frac{\ell_1 + \ell_2}{d}$. From the point of view of the excess intensity correlation, the path extensions resulting from the beamsplitter in each telescopes according to eqs. 2.25 and 2.26 effectively produce *co-located ghost images* of sources a and b , despite their true images located at different points on the celestial sphere. Furthermore, the \mathbf{b}_p -dependence of ℓ_b^{opt} can correct for the aperture smearing at each telescope.

2.3 Finite source size

In sections 2.1.2 and 2.2.2, we have given examples of intensity correlation signals for *point-like* sources. However, once the intensity interferometer resolves either or both of the sources ($\sigma_{\theta_{\text{res}}} \lesssim \theta_j$ with θ_j the characteristic angular size of the source), the visibility is reduced. This is an important effect, because the differential light-centroiding precision between two sources scales favorably with baseline distance d until the sources are resolved, so the optimal operating point will be $\sigma_{\theta_{\text{res}}} \sim \theta_j$ (see section 2.4). We review the details of this finite-source-size effect on the intensity fringes here for the two main sources of interest—stars and quasars—but refer the reader to the classic references [35, 36] for more background, as determining stellar radii has been the primary use case of intensity interferometry so far.

We write the differential surface brightness per unit wavenumber k in a single spectral channel of bandwidth σ_k centered at $k = \bar{k}$ as:

$$\frac{dI}{dk d\Omega} = e^{-\frac{(k-\bar{k})^2}{2\sigma_k^2}} \sum_j^{\text{sources}} \left. \frac{dI_j}{dk d\Omega} \right|_{\text{thermal}}, \quad (2.29)$$

where the pre-factor approximates the effect of a (Gaussian) spectral filter, and we assume that the sources j are optically thick thermal emitters, whose intrinsic differential surface brightness

$$\left. \frac{dI_j}{dk d\Omega} \right|_{\text{thermal}} = \frac{\hbar c^2}{4\pi^3} \frac{k^3}{e^{\hbar ck/k_B T_j(\hat{\theta} - \hat{\theta}_j)} - 1} \quad (2.30)$$

depends only on the temperature function $T_j(\hat{\theta} - \hat{\theta}_j)$ with $\hat{\theta}_j$ taken to be the light centroid of the source and k_B the Boltzmann constant. The excess fractional intensity correlation signals of eqs. 2.7 and 2.21 contain integrals of the form:

$$\int dk \int d\Omega \frac{dI}{dk d\Omega} e^{-ik\hat{\theta} \cdot \mathbf{d}} \simeq I(\bar{k}) \int dk \frac{e^{-\frac{(k-\bar{k})^2}{2\sigma_k^2}}}{\sqrt{2\pi}\sigma_k} \sum_j e^{-ik\hat{\theta}_j \cdot \mathbf{d}} \tilde{I}_j(\bar{k}) \mathcal{F}_j(\bar{k}, \mathbf{d}) \quad (2.31)$$

where we have defined the total flux $I(\bar{k})$ in the channel centered at \bar{k}

$$I(\bar{k}) \equiv \sum_j I_j(\bar{k}) = \sum_j \int d\Omega \frac{\hbar c^2}{2^{3/2}\pi^{5/2}} \frac{\sigma_k \bar{k}^3}{e^{\hbar c\bar{k}/k_B T_j(\hat{\theta})} - 1}, \quad (2.32)$$

and the fractional fluxes $\tilde{I}_j(\bar{k}) \equiv I_j(\bar{k})/I(\bar{k})$. The ‘‘form factor’’ is

$$\mathcal{F}_j(\bar{k}, \mathbf{d}) \equiv \frac{\int d\Omega e^{-i\bar{k}\mathbf{d} \cdot \hat{\theta}} \left[e^{\hbar c\bar{k}/k_B T_j(\hat{\theta})} - 1 \right]^{-1}}{\int d\Omega \left[e^{\hbar c\bar{k}/k_B T_j(\hat{\theta})} - 1 \right]^{-1}} \quad (2.33)$$

and is equal to unity for point-like sources, i.e. $\mathcal{F}_j(\bar{k}, \mathbf{d}) \rightarrow 1$ as $\bar{k}d\theta_j \rightarrow 1$, and is the implicit limit we have worked in for the examples in sections 2.1.2 and 2.2.2.

Incorporating finite-size effects is straightforward upon inspection of eq. 2.31: for every (fractional) flux factor $\tilde{I}_j(\bar{k})$ of a source j in a spectral channel centered at \bar{k} , one is to insert also the form factor $\mathcal{F}_j(\bar{k}, \mathbf{d})$ from eq. 2.33. For example, the excess fractional correlation for two sources a and b from eq. 2.28 is modified to:

$$C^{\text{opt}}(\mathbf{d}) \simeq \frac{1}{4\sqrt{2}c\sigma_k\sigma_t} \left\{ \tilde{I}_a(\bar{k})^2 |\mathcal{F}_a(\bar{k}, \mathbf{d})|^2 + \tilde{I}_b(\bar{k})^2 |\mathcal{F}_b(\bar{k}, \mathbf{d})|^2 + 2\tilde{I}_a(\bar{k})\tilde{I}_b(\bar{k}) \text{Re} \left\{ \mathcal{F}_a(\bar{k}, \mathbf{d})\mathcal{F}_b^*(\bar{k}, \mathbf{d}) e^{i[\bar{k}\mathbf{d} \cdot \delta\boldsymbol{\theta}_{ba}]} \right\} e^{-\frac{\sigma_k^2}{4}(\mathbf{d} \cdot \delta\boldsymbol{\theta}_{ba})^2} \right\}. \quad (2.34)$$

The suppression of the one-source terms $|\mathcal{F}_j(\bar{k}, \mathbf{d})|^2 \rightarrow 0$ as $\bar{k}d\theta_j \rightarrow \infty$ in the first line of eq. 2.34 is how stellar diameters can be determined. Not surprisingly, the finite source sizes also suppress the two-source term in the second line. Note that $\mathcal{F}_a\mathcal{F}_b^*$ is in general a complex number that can give an additive contribution to the phase of interest, namely $\bar{k}\mathbf{d} \cdot \delta\boldsymbol{\theta}_{ba}$. For sources that are reflection-symmetric along the axis defined by \mathbf{d} projected onto the celestial sphere, which is guaranteed for *any* baseline orientation as long as the source is spherically symmetric, the form factor is real and does not contribute to the phase. Even if \mathcal{F}_j is not real, its phase can be modeled and estimated from the one- and two-source intensity fringes. We assume that this is done at sufficient fidelity and will ignore this phase hereafter.

As we will see in section 2.4, differential astrometry with intensity interferometry is best performed on compact sources with high surface brightness, so stars and quasars are the most suitable targets. Let us compute the flux and form factor of eqs. 2.32 and 2.33 for these two types of objects. For simplicity, we model stars as single-temperature disks

$$T_s(\hat{\theta}) = T_s \Theta_H(\theta_s - \theta) \quad (2.35)$$

where the temperature equals T_s on the disk of angular radius $\theta_s = R_s/D_s$, with R_s and D_s the physical stellar radius and line-of-sight distance. This gives a flux per spectral channel of

$$I_s(\bar{k}) = \frac{\hbar c^2}{(2\pi)^{3/2}} \frac{\sigma_k \bar{k}^3 \theta_s^2}{e^{\hbar c \bar{k}/k_B T_s} - 1}, \quad (2.36)$$

and a simple form factor

$$\mathcal{F}_s(\bar{k}, \mathbf{d}) = \frac{2J_1(\bar{k}d\theta_s)}{\bar{k}d\theta_s} \quad (2.37)$$

which scales as $-\sqrt{8/\pi} \cos(\bar{k}d\theta_s + \pi/4)/(\bar{k}d\theta_s)^{3/2}$ at $\bar{k}d\theta_s \gg 1$.

For quasars, we assume the emission is also optically thick with a local temperature function of:

$$T_q(\hat{\theta}) = \frac{T_{500}}{1+z_q} \left(\frac{R_{500}}{R} \right)^{3/4} = T_{500} \left(\frac{\theta_{500}}{\theta} \right)^{3/4} \quad (2.38)$$

where $T_{500} = 28,776$ K is the temperature corresponding to a wavelength of $\lambda = 500$ nm, and R_{500} is the physical radius (in the quasar's local frame) at which this temperature is achieved. The apparent angular radius $\theta_{500} = R_{500}/[D_q(1+z_q)^{4/3}]$ is where this temperature is achieved in the *observer's* frame, after accounting for the redshift of the quasar z_q and its angular diameter distance D_q . This model is a simplified version of the emission from a face-on accretion disk in the model of ref. [70], with temperature function in the quasar's frame:

$$T_q(R) = T_{q,0} \left(\frac{R_{\text{isco}}}{R} \right)^{3/4} \left[1 - \left(\frac{R_{\text{isco}}}{R} \right)^{1/2} \right]^{1/4}, \quad (2.39)$$

with $T_{q,0}$ is a reference temperature given by

$$T_{q,0} = \left(\frac{3G^2 M_{\text{BH}}^2 m_p f_{\text{Edd}}}{2c\sigma_B \sigma_T \eta_q R_{\text{isco}}^3} \right)^{1/4} \approx 3.33 \times 10^5 \text{ K} \left(\frac{f_{\text{Edd}}}{\eta_q} \right)^{1/4} \left(\frac{10^9 M_\odot}{M_{\text{BH}}} \right)^{1/4} \left(\frac{GM_{\text{BH}}/c^2}{R_{\text{isco}}} \right)^{1/4} \quad (2.40)$$

with M_{BH} the black hole mass, m_p the proton mass, f_{Edd} the bolometric luminosity relative to the Eddington luminosity, η_q the bolometric luminosity relative to the accretion rate, $\sigma_B = (\pi^2/60)k_B^4/\hbar^3 c^2$ the Stefan–Boltzmann constant, $\sigma_T = (8\pi/3)(\hbar^2/c)\alpha^2/m_e^2$ the Thomson scattering cross-section, and R_{isco} the innermost stable circular orbit within the accretion disk (equaling $6GM_{\text{BH}}/c^2$ for a non-spinning black hole, and GM_{BH}/c^2 for a maximally spinning black hole). The apparent angular radius of the accretion disk is $\theta_{\text{isco}} = R_{\text{isco}}/D_q$.

In the simplified model of eq. 2.38, the observed flux from the quasar per spectral channel is then:

$$I_q(\bar{k}) = \frac{\xi_q \hbar c^2}{(2\pi)^{3/2}} \sigma_k \bar{k}^{-1/3} \left(\frac{k_B T_{500}}{\hbar c} \right)^{8/3} \theta_{500}^2, \quad (2.41)$$

with $\xi_q = \Gamma(11/3)\zeta(8/3) \approx 5.15$, and the form factor is:

$$\mathcal{F}_q(\bar{k}, \mathbf{d}) = \xi_q^{-1} \int_0^\infty dy \frac{2y}{\exp y^{3/4} - 1} J_0 \left[\left(\frac{k_B T_{500}}{\hbar c} \right)^{4/3} \bar{k}^{-1/3} d \theta_{500} y \right]. \quad (2.42)$$

This form factor depends on \bar{k} and d through the combination $a = (k_B T_{500}/\hbar c)^{4/3} \bar{k}^{-1/3} d \theta_{500}$; when $a \ll 1$, the form factor goes to unity, while for $a \gg 1$, it is approximately $\mathcal{F}_q \approx 0.3a^{-5/4}$. This is a slightly less severe suppression ($\propto d^{-5/4}$) than the form factor scaling for a star ($\propto d^{-3/2}$).

2.4 Noise and light-centroiding precision

In this section, we estimate the statistical noise on our primary observable—the excess intensity correlation of eq. 2.21—allowing us to calculate the signal-to-noise ratio (SNR) and light-centroiding precision for different sources. We postpone a discussion of phase errors and other systematic errors to section 3.

The data collected by each photodetector p are arrival times $\{t_i\}$ for N_p photons, from which one can build a simple estimator \hat{I}_p (the hat indicates that it is a data-driven *estimate*) of the instantaneous intensity at time t_p :

$$\hat{I}_p(t_p) = \frac{\hbar c \bar{k}}{\eta_p A_p} \sum_{i=1}^{N_p} \frac{e^{-\frac{(t_p - t_i)^2}{\sigma_t^2}}}{\sqrt{\pi} \sigma_t}. \quad (2.43)$$

Above, \bar{k} is the mean wavevector of the light (assumed to be observed in a fractionally narrow band), η_p is the photodetection efficiency (excluding transmissivity and reflectivity factors from the splitter and combiner in section 2.2), and A_p is the telescope's aperture area. The effective timing precision *per photodetector* is taken to be $\sigma_t/\sqrt{2}$ with σ_t from eq. 2.8, so that relative photon arrival times, i.e. $t_2 - t_1$, have relative timing precision σ_t . An unbiased, optimal estimator of the excess fractional intensity correlation between two detectors, time averaged over a time interval t_{obs} , is then:

$$\hat{C}(\mathbf{d}, \tau) = \frac{\overline{\hat{I}_1(t) \hat{I}_2(t + \tau)}}{\hat{I}_1(t) \hat{I}_2(t + \tau)} - 1. \quad (2.44)$$

The overline signifies time-averaging according to:

$$\overline{f(t)} \equiv \int_{t-t_{\text{obs}}/2}^{t+t_{\text{obs}}/2} \frac{dt'}{t_{\text{obs}}} f(t'), \quad (2.45)$$

for any time-dependent observable $f(t)$. The expectation value of the estimator in eq. 2.44 is $\langle \hat{C} \rangle = C$ with C from eq. 2.21; further details can be found in appendix B.1. (We assume that the time dependence of C during t_{obs} is negligible.)

The estimator for the intensity correlation in eq. 2.44 only receives contributions when photodetectors 1 and 2 each record photons with relative times of arrival (given a fixed offset τ) separated by $\mathcal{O}(\sigma_t)$ or less. Most photons detected at photodetector 1 will not have such a “simultaneous” photon at photodetector 2, and the excess fractional correlation is small numerically (of order $C \sim 1/c\sigma_k\sigma_t \ll 1$), so obtaining a high SNR requires sufficiently bright sources and long observation times, so that $N_p \gg 1$. In what follows, we can therefore safely neglect Poisson fluctuations in the *total number* N_p of photons, and only consider the arrival times $\{t_i\}$ as random variables. We further assume

$$\frac{1}{c\bar{k}} \ll \frac{1}{c\sigma_k} \ll \sigma_t \ll t_{\text{reset}} \ll \frac{t_{\text{obs}}}{N_p}, \quad (2.46)$$

though modifications of the formulae below for weak or reversed hierarchies are not difficult. Equation 2.46 is equivalent to assuming a strong hierarchy of time scales, in ascending order: the period of light ($1/c\bar{k}$), the coherence time of the light ($1/c\sigma_k$), the relative timing precision (σ_t), the reset time of the photodetector (t_{reset}), and the typical time between photon counts (t_{obs}/N_p). With those assumptions, it is straightforward to calculate the expected estimated intensity:

$$\langle \hat{I}_p \rangle = \frac{\hbar c \bar{k}}{\eta_p A_p} \frac{N_p}{t_{\text{obs}}} \equiv \langle I_p \rangle, \quad (2.47)$$

and, more tediously, the statistics-limited standard deviation on \hat{C} :

$$\sigma_{\hat{C}} \simeq \sqrt{\frac{\text{Var} \left\{ \hat{I}_1 \hat{I}_2 \right\}}{\langle I_1 \rangle \langle I_2 \rangle}} \simeq \sqrt{\frac{t_{\text{obs}}}{\sqrt{4\pi}\sigma_t} \frac{1}{\sqrt{N_1 N_2}}} = \sqrt{\frac{1}{\sqrt{4\pi}\sigma_t t_{\text{obs}}} \frac{\hbar c \bar{k}}{\sqrt{\eta_1 \eta_2 A_1 A_2}} \frac{1}{\sqrt{\langle I_1 \rangle \langle I_2 \rangle}}}. \quad (2.48)$$

We provide derivations of eqs. 2.47 and 2.48 in appendix B.1.

We can estimate $\sigma_{\hat{C}}$ numerically by using the flux-per-channel formula from eq. 2.32. If one has n_p^{arr} telescopes at site $p = 1, 2$, the noise is reduced by a factor of $1/\sqrt{n_1^{\text{arr}} n_2^{\text{arr}}}$ by averaging at each of the two sites. Finally, we correct for the suppression due to the two uncorrelated polarizations of light from unpolarized sources by multiplying by 1/2 the total signal-to-noise ratio (SNR) on the excess fractional intensity correlation:

$$\text{SNR} = \frac{1}{2} \sqrt{n_1^{\text{arr}} n_2^{\text{arr}} \sum_{\bar{k}} \left(\frac{C(\mathbf{d}, \tau)}{\sigma_{\hat{C}}} \right)_{\bar{k}}^2}, \quad (2.49)$$

where the sum is over channels with different \bar{k} separated from each other by more than σ_k , e.g. with a logarithmic spectral spacing between channels of the form $e^{2n\sigma_k/\bar{k}}$ for integer n . In figure 6, we plot $\sigma_{\hat{C}}$ from eq. 2.48 for a single pair of telescopes ($n_p^{\text{arr}} = 1$) as a function of \bar{k} for thermal spectra of four different reference stars, convoluted with a narrow spectral filter of width σ_k . For the parameters plotted in figure 6, the integrated signal-to-noise ratio over 6,020 logarithmically spaced channels between $\bar{\lambda} = 1 \mu\text{m}$ and $\bar{\lambda} = 300 \text{nm}$ from eq. 2.49 is $\text{SNR} = \{93, 432, 371, 91\}$ for the white dwarf, main sequence, red giant, and blue giant stars, respectively. Likewise, for the fiducial quasar shown in pink in figure 6, the integrated SNR equals 2.2, despite $\sigma_{\hat{C}} > C \simeq 1/2\sqrt{2}c\sigma_k\sigma_t$ in any one spectral channel.

For differential astrometry using EPIC, the relevant term in C is reduced by a factor of 1/4 (cfr. eq. 2.28), while the observed fluxes $\propto \langle I_p \rangle$ are reduced by a factor of 1/2 per

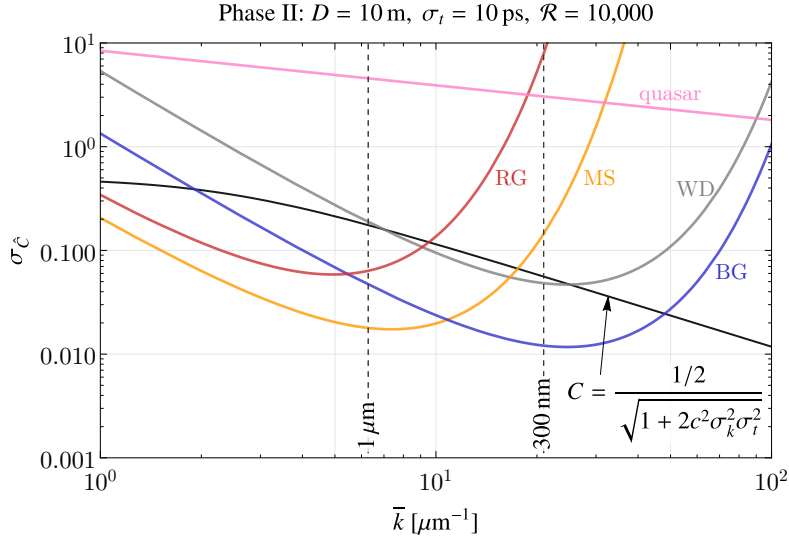


Figure 6: Single-channel precision $\sigma_{\hat{c}}$ from eq. 2.48 on the excess intensity correlation, as a function of wavenumber \bar{k} (for reference, the wavelength range of $\bar{\lambda} = [300 \text{ nm}, 1 \mu\text{m}]$ is indicated by black, dashed, vertical lines). The light gray, yellow, red, and blue curves correspond to a white dwarf (“WD”, $T = 20,000$ K, $D = 10$ pc, $R = 10^{-2} R_{\odot}$), Sun-like main sequence star (“MS”, $T = 6,000$ K, $D = 100$ pc, $R = 1 R_{\odot}$), red giant (“RG”, $T = 4,000$ K, $D = 5$ kpc, $R = 10^2 R_{\odot}$), and blue giant (“BG”, $T = 20,000$ K, $D = 5$ kpc, $R = 10 R_{\odot}$), respectively. The pink curve shows $\sigma_{\hat{c}}$ for a quasar at redshift $z_q = 1$ with optical radius $R_{500} = 10^{16}$ cm (eq. 2.38). We assume telescope parameters from Phase II in table 1, and an integration time $t_{\text{obs}} = 10^4$ s. The solid black line indicates the single-source excess fractional correlation (eq. 2.11). The integrated SNR of eq. 2.49 between $1 \mu\text{m}$ and 300 nm is $\{93, 432, 371, 91, 2.2\}$ for these sources $\{\text{WD}, \text{MS}, \text{RG}, \text{BG}, \text{quasar}\}$.

source if $\epsilon = 1/\sqrt{2}$ (cfr. eq. 2.22), reducing the total SNR by a factor of $1/8$ (compared to not having any path extension at all). We note though that compared to figure 6, this flux loss is compensated by observing *two* sources simultaneously. In addition, with the use of a polarizing beamsplitter, one could theoretically recover a factor of $\sqrt{2}$ in SNR and light-centroiding precision [39, 71]. Likewise, one could recover an extra factor of 2 from the second output port of the beam recombiner (by also recording light going to the right from the last semi-transparent plate in figure 5b).

The main application of EPIC is to measure the separation—and especially their change over time—between the light centroids of two point-like sources. This can be achieved at a precision better than $\sigma_{\theta_{\text{res}}}$ from eq. 2.9 if the differential astrometry fringe of eq. 2.28 is detected at high SNR. Denote by $\sigma_{\delta\theta}$ the precision to which the light-centroid separation $\boldsymbol{\theta}_{ba} \cdot \hat{\mathbf{d}}$ along the baseline direction can be measured. A standard error propagation calculation on eq. 2.34 then yields a light-centroiding precision of

$$\sigma_{\delta\theta} = 2 \left[n_1^{\text{arr}} n_2^{\text{arr}} \sum_{\bar{k}} \left(\frac{\sigma_{\theta_{\text{res}}} \sigma_{\hat{c}}}{|\sin(\bar{k}\mathbf{d} \cdot \boldsymbol{\delta}\boldsymbol{\theta}_{ba})| \tilde{I}_a \tilde{I}_b |\mathcal{F}_a \mathcal{F}_b^*|} \right)^{-2} \right]^{-1/2} \quad (2.50)$$

when combining all channels labeled by \bar{k} , between $k_{\text{min}} < \bar{k} < k_{\text{max}}$. In the limiting case of two identical detectors ($n_1^{\text{arr}} = n_2^{\text{arr}} = 1$, $\eta_1 = \eta_2 = \eta$, $A_1 = A_2 = A$, etc.), fixed spectral

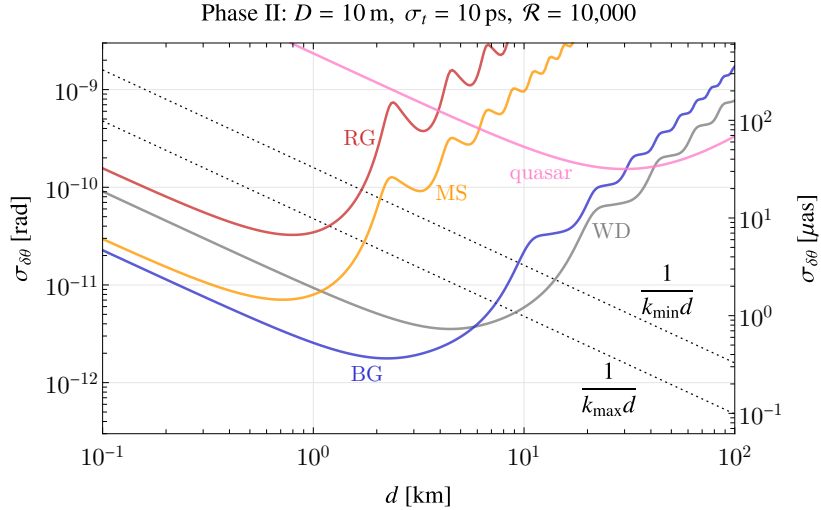


Figure 7: Light-centroiding precision $\sigma_{\delta\theta}$ from eq. 2.51 as a function of baseline distance d (assuming optimal alignment, i.e. $\mathbf{d} \cdot \boldsymbol{\theta}_{ba} = d\theta_{ba}$) between *identical* stars and quasars, indicated by color and contours (in units of μas). The parameters for the telescopes (Phase II in table 1), stars, and quasars are the same as in figure 6.

resolution (\bar{k}/σ_k independent of \bar{k}), and identical, unpolarized, sources a and b , we find:

$$\sigma_{\delta\theta} \simeq \frac{2^{13/2}\pi^{5/4}\hbar^3 c^3}{k_B^3} \frac{1}{\eta A d_{\parallel}} \sqrt{\frac{\sigma_t}{t_{\text{obs}}}} \sqrt{\frac{\sigma_k}{\bar{k}}} \left\{ \frac{1}{T_s^3 \theta_s^2} \left[\int_{x_{\min,s}}^{x_{\max,s}} dx \frac{x^5}{(e^x - 1)^2} \mathcal{F}_s^4(x k_B T_s / \hbar c, \mathbf{d}) \right]^{-1/2} \right. \\ \left. \frac{1}{T_{500}^3 \theta_{500}^2} \left[\int_{x_{\min,500}}^{x_{\max,500}} dx x^{-1/3} \mathcal{F}_q^4(x k_B T_{500} / \hbar c, \mathbf{d}) \right]^{-1/2} \right\}, \quad (2.51)$$

where $x_{\min,s} \equiv \hbar c k_{\min} / k_B T_s$ and $x_{\min,500} \equiv \hbar c k_{\min} / k_B T_{500}$, and similarly for $x_{\max,s}$ and $x_{\max,500}$. To get to eq. 2.51 from eq. 2.50, we approximated $\sin^2(\bar{k}\mathbf{d} \cdot \boldsymbol{\delta}\boldsymbol{\theta}_{ba}) \sim 1/2$, and turned the sum over \bar{k} into an integral according to $\sum_{\bar{k}} \rightarrow \int d\bar{k} / 2\sigma_k$. The functions \mathcal{F}_s and \mathcal{F}_q are defined in eqs. 2.37 and 2.42, respectively. The effective baseline d_{\parallel} is the magnitude of the baseline vector component of \mathbf{d} parallel to the source separation $\boldsymbol{\theta}_{ba}$.

The factors outside the curly brackets in eq. 2.51 are in the observer's control: higher efficiencies η , larger collecting areas A , better timing precision σ_t , longer observation times t_{obs} , and higher spectral resolution \bar{k}/σ_k generally improve the light-centroiding precision. Inside the curly brackets, we have provided the expression relevant for astrometry between two identical stars (top line) of temperature T_s and angular radius θ_s , and two identical quasar images (bottom line) with apparent angular optical radius of θ_{500} . Light centroiding precision improves for higher-temperature sources (higher T_s), and for sources that subtend larger angles on the sky (larger θ_s in the case of stars, or θ_{500} for quasars).

In figure 7, we plot the light-centroiding precision of eq. 2.51 for the same 4 stars and fiducial quasar, and instrumental parameters as in figure 6; e.g. the gray curve is the differential astrometric light-centroiding precision between two identical white dwarfs of $T_s = 10^4$ K with $R_s = 10^{-2} R_{\odot}$ at $D_s = 10$ pc. We can see that the astrometric error scales as $\sigma_{\delta\theta} \propto 1/d_{\parallel}$ until the sources are resolved, so there is an optimum baseline distance d_{opt} . For quasars, the

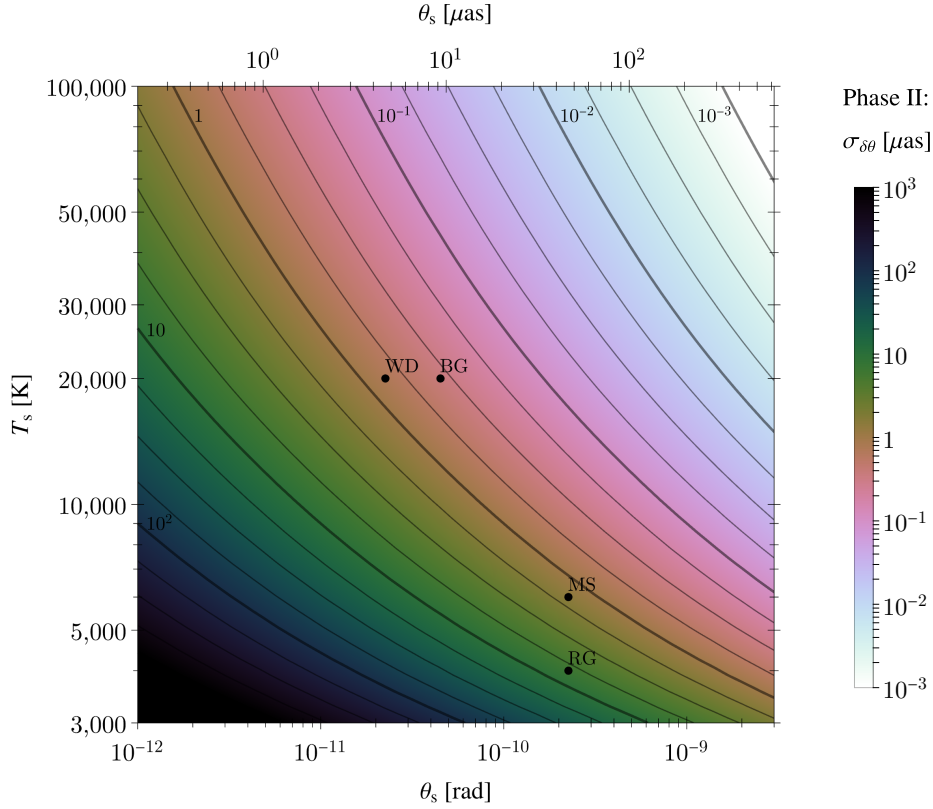


Figure 8: Light-centroiding precision $\sigma_{\delta\theta}$ from eq. 2.51 between two identical stars of angular size $\theta_s = R_s/D_s$ and temperature T_s , at the optimal baseline distance d^{opt} for a Phase II EPIC (see table 1).

optimum baseline distance is just a simple linear function of θ_{500} :

$$d_{\text{opt,q}} \approx 2.31 \text{ km} \left(\frac{10^{-11} \text{ rad}}{\theta_{500}} \right) \quad (2.52)$$

where we assumed $k_{\text{min}} = 2\pi/(1000 \text{ nm})$ and $k_{\text{max}} = 2\pi/(300 \text{ nm})$. In figure 8, we display the light-centroiding precision at this optimal baseline distance d_{opt} , assuming $d = d_{\parallel}$ for stellar sources as a function of θ_s and T_s . We show the equivalent quantity in figure 19 for quasars as a function of θ_{500} , assuming the optimum baseline of eq. 2.52.

2.5 Atmospheric phases

In this section, we outline the effects of non-negligible propagation phases on EPIC at “large” angles. We compute the size of the atmospheric aberration and its resulting limitation on the field of view of EPIC.

Let us start with the same electric field as in eqs. 2.2 and 2.18, but retain the phases $\tilde{\phi}_{i\alpha}^{(p)}(t_p)$ *not* intrinsic to the source but accumulated along the path from the source i to the detector p for a mode of frequency k_α :

$$E_p(t_p) = \epsilon \sqrt{1 - \epsilon^2} \sum_{i=1}^{N_\theta} \sum_{\alpha=1}^{N_k} \sum_{n=0}^1 e^{-ink_\alpha \ell_p} E_{i\alpha} \exp \left\{ i \left[k_\alpha (ct_p - r_{ip}) + \phi_{i\alpha}^{\text{em}} + \tilde{\phi}_{i\alpha}^{(p)}(t_p) \right] \right\}, \quad (2.53)$$

In the continuum limit, the relevant extended-path intensity correlator is modified to:

$$C(\mathbf{d}, \tau) = \frac{\epsilon^4 (1 - \epsilon^2)^2}{\langle I_1 \rangle \langle I_2 \rangle} \int \frac{d^2 b_1}{A_1} \int \frac{d^2 b_2}{A_2} \int d(\Delta t) \frac{1}{\sqrt{2\pi}\sigma_t} e^{-\frac{(\Delta t)^2}{2\sigma_t^2}} \quad (2.54)$$

$$\times \left| \int dk \int d\Omega \frac{dI}{dk d\Omega} (1 + e^{-ik\ell_1}) (1 + e^{ik\ell_2}) e^{i[k(c(\Delta t - \tau) - \hat{\boldsymbol{\theta}} \cdot (\mathbf{d} + \Delta \mathbf{b})) + \tilde{\phi}^{(1)}(t, \hat{\boldsymbol{\theta}}, k) - \tilde{\phi}^{(2)}(t + \tau, \hat{\boldsymbol{\theta}}, k)]} \right|^2,$$

which should be regarded as the generalization of eq. 2.21 to account for propagation phases. The limit towards conventional intensity interferometry is attained in the limit $\ell_p \rightarrow 0$. The expected intensities $\langle I_p \rangle$ are unchanged from eq. 2.19.

For two point-like sources a and b , we find

$$C^{\text{opt}}(\mathbf{d}) \simeq \frac{1}{4\sqrt{2}c\sigma_k\sigma_t} \left\{ \tilde{I}_a^2 + \tilde{I}_b^2 + 2\tilde{I}_a\tilde{I}_b \cos \left[\bar{k}\mathbf{d} \cdot \boldsymbol{\delta}\boldsymbol{\theta}_{ba} + \Delta\tilde{\phi}^{(1,2)}(\bar{k}, \hat{\boldsymbol{\theta}}_a, \hat{\boldsymbol{\theta}}_b) \right] e^{-\frac{\sigma_k^2}{4}(\mathbf{d} \cdot \boldsymbol{\delta}\boldsymbol{\theta}_{ba})^2} \right\} \quad (2.55)$$

as the generalization of 2.28 for example. In the above, we have defined the doubly-differential noise phase:

$$\Delta\tilde{\phi}^{(1,2)}(\bar{k}, \hat{\boldsymbol{\theta}}_a, \hat{\boldsymbol{\theta}}_b) \equiv \tilde{\phi}^{(1)}(\bar{k}, \hat{\boldsymbol{\theta}}_a) + \tilde{\phi}^{(2)}(\bar{k}, \hat{\boldsymbol{\theta}}_b) - \tilde{\phi}^{(1)}(\bar{k}, \hat{\boldsymbol{\theta}}_b) - \tilde{\phi}^{(2)}(\bar{k}, \hat{\boldsymbol{\theta}}_a), \quad (2.56)$$

whose time dependence we have implicitly suppressed (since the relevant quantity is its time average).

We are particularly interested in calculating the atmospheric contribution to the doubly-differential phase of eq. 2.56 due to the fluctuating index of refraction along the light paths. Denote by $n[\bar{k}, \mathbf{x}_{ip}(s)]$ the deviation of the index of refraction from its mean at wavenumber \bar{k} along the path from detector p to source i : $\mathbf{x}_{ip}(s) \equiv \mathbf{r}_p + \hat{\boldsymbol{\theta}}_i s$ with $0 < s < r_{ip}$. The total refractive phase accumulation along the path is:

$$\tilde{\phi}^{(p)}(\bar{k}, \hat{\boldsymbol{\theta}}_i) = \bar{k} \int_0^{r_{ip}} ds n[\bar{k}, \mathbf{x}_{ip}(s)]. \quad (2.57)$$

We have explicitly subtracted out the mean index of refraction, so $\langle n[\bar{k}, \mathbf{x}(s)] \rangle_{\text{atm}}$ vanishes by construction along any path $\mathbf{x}(s)$ through the atmosphere, and thus also the corresponding $\langle \tilde{\phi} \rangle_{\text{atm}}$. This subtraction of the mean can be done to a sufficient fidelity, down to an effective precision less than a millimeter, corresponding to $\lesssim 3$ ps delay [72–74].

However, there are *fluctuations* in n , as measured by the structure function [75–78]:

$$D_n(r) \equiv \langle (n[\mathbf{r}' + \mathbf{r}] - n[\mathbf{r}'])^2 \rangle_{\text{atm}} = C_n^2(h)r^{2/3} \quad \text{for } l_0 \ll r \ll L_0, \quad (2.58)$$

where we have dropped the dependence on \bar{k} for notational simplicity. The structure function does not depend on the reference position \mathbf{r}' except through the slow dependence on altitude h in the atmosphere. The two-thirds scaling follows from Kolmogorov's ansatz for turbulence, and is an *overestimate* both above the outer scale $L_0 \sim 10^{1\pm 1}$ m (where $D_n(r)$ asymptotes to a constant $\langle n^2 \rangle$) and below the inner scale $l_0 \sim 10^{-2.5\pm 0.5}$ m (where $D_n(r) \approx r^2$). The constant C_n has dimensions of $[\text{length}]^{-1/3}$, depends on the weather, and typically decreases with altitude. Typical values are $C_n \sim 10^{-8} \text{ m}^{-1/3}$ for altitudes between 1–10 km, as depicted in figure 20 for the SLC night model [79]. Also useful is the correlation function

$$B_n(r) \equiv \langle n[\mathbf{r}' + \mathbf{r}]n[\mathbf{r}'] \rangle_{\text{atm}}. \quad (2.59)$$

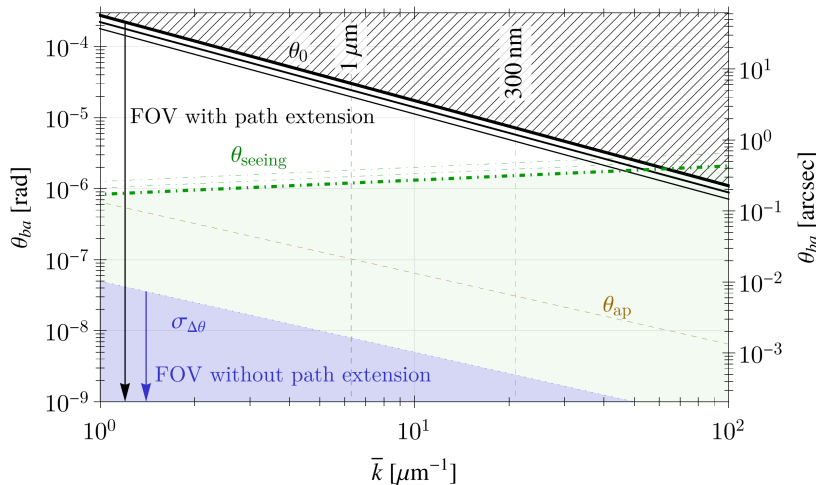


Figure 9: Isoplanatic patch angle θ_0 (black solid lines) as a function of wavenumber \bar{k} for three different zenith angles $\gamma = \{0^\circ, 45^\circ, 60^\circ\}$. Atmospheric refraction suppresses the intensity fringe for differential astrometry at an angle θ_{ba} as $\exp\{-\theta_{ba}/\theta_0\}^{5/3}$ (cfr. eq. 2.62). The blue dotted line indicates the dynamic range $\sigma_{\Delta\theta}$ of eq. 2.15 for intensity interferometry without path extensions at $d = 100$ km and $\bar{k}/\sigma_k = 5,000$. The effective field of view (FOV) for traditional intensity interferometry is $\sigma_{\Delta\theta}$, while it is as large as θ_0 for EPIC, an increase by more than three orders of magnitude at the chosen parameters. We plot the angular size θ_{seeing} of the seeing disk from eq. 2.63 as green dash-dotted lines ($\gamma = \{60^\circ, 45^\circ, 0^\circ\}$) above this line, two sources can be resolved from a ground-based observatory at an excellent site without adaptive optics. The brown dashed line indicates the critical angle θ_{ap} above which wavefront errors need to be taken into account for a 4 m aperture diameter (the \mathbf{b}_p dependence in eq. 2.55).

The structure function can be expressed in terms of the correlation function as $D_n(r) = 2[B_n(0) - B_n(r)]$.

The doubly differential atmospheric refraction phase from eq. 2.56 is a (rapidly) fluctuating quantity with expected standard deviation:

$$\sigma_\phi^{\text{atm}} \equiv \sqrt{\left\langle \left[\Delta\tilde{\phi}^{(1,2)}(\bar{k}, \hat{\theta}_a, \hat{\theta}_b) \right]^2 \right\rangle_{\text{atm}}} \simeq \sqrt{2} \left(\frac{\theta_{ba}}{\theta_0(\bar{k}, \gamma)} \right)^{5/6}, \quad (2.60)$$

where γ is the angle of the sources away from zenith (assumed to be the same for both detector locations, a reasonable assumption for baselines smaller than Earth's radius $d \ll R_\oplus$), and θ_0 is the *isoplanatic patch angle* [80, 81]:

$$\theta_0(\bar{k}, \gamma) \equiv \left[2.9\bar{k}^2 \int ds C_n^2(s \cos \gamma) s^{5/3} \right]^{-3/5} \approx 2.7 \text{ arcsec} \left(\frac{\bar{\lambda}}{500 \text{ nm}} \right)^{6/5} \cos^{5/8}(\gamma). \quad (2.61)$$

In the latter numerical estimate, we have used the SLC night model. We derive eq. 2.60 in appendix B.2. This fluctuating atmospheric phase suppresses the fringe of differential astrometry as $\int d(\Delta\tilde{\phi}) (\sqrt{2\pi}\sigma_\phi^{\text{atm}})^{-1} e^{-i\Delta\tilde{\phi}^2/2(\sigma_\phi^{\text{atm}})^2} e^{-i\Delta\tilde{\phi}} = e^{-(\sigma_\phi^{\text{atm}})^2/2}$, which when applied

to eq. 2.28 gives:

$$C^{\text{opt}}(\mathbf{d}) \simeq \frac{1}{4\sqrt{2}c\sigma_k\sigma_t} \left\{ \tilde{I}_a^2 + \tilde{I}_b^2 + 2\tilde{I}_a\tilde{I}_b \cos[\bar{k}\mathbf{d} \cdot \delta\boldsymbol{\theta}_{ba}] \exp \left\{ - \left[\frac{\theta_{ba}}{\theta_0(\bar{k}, \gamma)} \right]^{5/3} \right\} e^{-\frac{\sigma_k^2}{4}(\mathbf{d} \cdot \delta\boldsymbol{\theta}_{ba})^2} \right\}. \quad (2.62)$$

with any other contributions to $\Delta\tilde{\phi}^{(1,2)}(\bar{k}, \hat{\boldsymbol{\theta}}_a, \hat{\boldsymbol{\theta}}_b)$ other than from the atmosphere ignored. Thus, any source separation smaller than the isoplanatic patch angle, i.e. $\theta_{ba} \lesssim \theta_0(\bar{k}, \gamma)$, can be considered acceptable.

The atmospheric phase error σ_ϕ^{atm} for intensity interferometry is dominated by atmospheric turbulence in the *upper* atmosphere, as the quantity $h^{8/3}C_n^2(h)$ typically peaks near $h \sim 10$ km. Therefore, the altitude of the telescopes plays only a minor role, and the observations can be taken near sea level, even in comparatively poor atmospheric conditions. This is to be contrasted with the size of the seeing disk:

$$\theta_{\text{seeing}}(\bar{k}, \gamma) = 0.92 \bar{k}^{-1/5} \left[\int ds C_n^2(s \cos \gamma) \right]^{3/5} \approx \frac{0.29 \text{ arcsec}}{\cos^{3/5} \gamma} \left(\frac{500 \text{ nm}}{\lambda} \right)^{1/5}, \quad (2.63)$$

where the SLC night model was used again to obtain the (optimistic) numerical estimate. At excellent observing sites, the seeing is smaller than the isoplanatic angle, so suitable sources can be resolved from the ground with some idea of their separation before EPIC is performed.

3 Observatory Design

In this section, we discuss the technical aspects of the extended-path intensity correlation technique. We begin by outlining the telescope design and array layout (section 3.1), and sketch out the operational protocol of an EPIC observation (section 3.2). We focus on two technological advances on the original intensity interferometry setup that allow us to perform intensity interferometry (including EPIC) on fainter sources than previously possible: fast photodetectors and readout electronics (section 3.3) and spectroscopic splitting (section 3.4). The required tolerances on the optically active surfaces and timing are summarized in section 3.5; a detailed conceptual design report is left for future work.

3.1 Overview

Telescopes

Each telescope within our proposed intensity interferometer array is essentially a stellar spectrograph with moderately high spectral resolution, an “internal amplitude interferometer” to create the path extension, and relatively loose optical tolerances (see section 3.5 below). Due to the high photon statistics required to tease out the weak intensity correlation, each telescope should have a large aperture and be equipped with ultra-fast photodetection electronics. The telescope design is illustrated in figure 5. The fiducial photodetection efficiency is taken to be $\eta = 0.5$, while other reference specifications—the aperture diameter D , timing resolution σ_t , spectral resolution \mathcal{R} , and number n_{arr} of telescopes per array site—are shown in table 1. No gains are expected from a spectral resolution higher than $\sqrt{2c\bar{k}}\sigma_t \approx 5 \times 10^4$ at $\bar{k} = 2\pi/(500 \text{ nm})$ and $\sigma_t = 10$ ps, cfr. eq. 2.11, which corresponds to a timing precision sufficiently fast to fully resolve the coherence time of the light in the spectral channel centered at a wavelength of 500 nm. Larger apertures are not inconceivable, especially given the

	D	σ_t	\mathcal{R}	n_{arr}	$\sigma_{\delta\theta}$ [μas]	$\sigma_{\hat{\theta}}$ [arcsec]	$\sigma_{\Delta\theta}$ [arcsec]
Phase I	4 m	30 ps	5,000	1	22.3	5.24	0.164
Phase II	10 m	10 ps	10,000	1	1.46	1.75	0.327
Phase III	10 m	3 ps	20,000	10	0.0564	0.524	0.656

Table 1: Fiducial EPIC array parameters in the near, medium, and long term (Phases I, II, and III): aperture diameter D , relative timing precision σ_t , spectral resolution \mathcal{R} , and number n_{arr} of telescope pairs sharing the same baseline. We assume a photodetection efficiency of $\eta = 0.5$ on top of the beamsplitters’ reflectivity/transmission coefficients. We quantify their performance by the optimum light-centroiding precision $\sigma_{\delta\theta}$ after an integration time $t_{\text{obs}} = 10^4$ s for a pair of Sun-like stars at a distance of 100 pc as well as the characteristic global astrometric precision $\sigma_{\hat{\theta}}$ and angular dynamic range $\sigma_{\Delta\theta}$ (at the optimum centroiding baseline). For such source pair, the optimum (projected) baseline distance is $\hat{\theta}_{ba} \cdot \mathbf{d} \approx 0.71$ km, corresponding to a fiducial angular resolution of $\sigma_{\theta_{\text{res}}} \approx 23 \mu\text{as}$ at $\bar{\lambda} = 500$ nm for all three EPIC Phases.

low to moderate tolerances required on the most of the optical surfaces, in particular the primary mirror. Large steerable telescopes with aperture diameters of 10–30 m are already in operation or construction for Cherenkov cosmic ray imaging [43–47].

Variable path extension

The main conceptual difference between an ordinary spectrograph and a constituent telescope of an EPIC array is that the latter requires an internal beamsplitter and recombiner (with unequal path lengths). In light of eqs. 2.25 and 2.26, to cover all possible source separations θ_{ba} up to the isoplanatic patch angle θ_0 of eq. 2.61, the internal interferometer of each telescope p should have the capability to create a differential optical path length of

$$\ell_p \sim \frac{\theta_{ba}d}{2} \lesssim \frac{\theta_0 d}{2} \sim 5 \text{ cm} \left(\frac{\theta_0}{2 \text{ arcsec}} \right) \left(\frac{d}{10 \text{ km}} \right). \quad (3.1)$$

This can be achieved by a corresponding tuning of the width w_p of the internal interferometer (at fixed γ and γ'), cfr. figure 5 and eq. 2.17. The precision to which ℓ_p is *adjustable* should be on the order of a wavelength, so that the intensity interferometer can operate near the main (ghost) fringe, to adjust θ_{ba}^{ref} such that $\delta\theta_{ba} \cdot \hat{\mathbf{d}} \sim \sigma_{\theta_{\text{res}}}$, and to correct for aperture smearing, i.e. the slightly different angle of incidence between the wavefronts from each source (the \mathbf{b} -dependence in eqs. 2.25 and 2.26). (In fact, as long as the aperture smearing effects are corrected to sub-wavelength precision, $|\delta\theta_{ba} \cdot \mathbf{d}| \lesssim \sigma_{\Delta\theta}$ is also acceptable.) Aperture smearing is negated by taking $\gamma' - \gamma$ equal to $\theta_{ba}f/2f'$ and with a relative tilt in the same direction as $\hat{\theta}_{ba}$ (see figure 5 and appendix C.2).

The positioning and control of the path extension require sub-wavelength tolerances over tens of centimeters, which are mild compared to what has been demonstrated in laboratory and observatory settings [82, 83]. For example, in the CHARA interferometer, a laser metrology unit controls the mirrors to a root-mean-squared error of 10–20 nm over distances of tens of meters [26], while mirrors in adaptive optics systems achieve similar or better control over smaller distances and angles [84, 85].

Array configuration

In this work, we primarily consider the case of a single pair of telescopes separated by a distance \mathbf{d} . Interesting science can be obtained from a single pair of telescopes (section 4), but the potential of an intensity interferometry array can grow quadratically with the number of telescopes in the array. This quadratic scaling can be made precise: the signal-to-noise ratio on the excess intensity correlation scales linearly with the number of telescope pairs n^{arr} sharing the same baseline in the array (eq. 2.49), so for the same light-centroiding precision $\sigma_{\delta\theta}$ (eq. 2.50), the required integration time t_{obs} scales as $1/(n^{\text{arr}})^2$. Equivalently, the light-centroiding precision can thus improve as $\sigma_{\delta\theta} \propto 1/n_{\text{arr}}$ for fixed integration time.

For a fixed number of telescopes, the optimal layout of an EPIC array is determined by the interplay of several considerations [86]. First, the optimal projected baseline separation falls in the 1 km–100 km range, primarily depending on the angular size of the source (and more weakly on source temperature). Second, the array should ideally have dense coverage in the (u, v) plane for faithful “image” reconstruction of the emission region(s). Third, the array should have sensitivity to many (pairs of) sources of varying angular sizes and locations on the sky. Fourth, the SNR should be maximized.

The first three considerations dictate that, for a source at zenith, the telescopes should be distributed along the boundary of (a slightly perturbed) Reuleaux triangle [87], a curved triangle of constant width (and the constant-width curve with the least rotational symmetry), with an overall size determined by the maximum desired baseline. This configuration creates the most uniform sampling (exact uniformity being impossible [88]) in a circular disk in Fourier space, suitable for image reconstruction [89] and for detecting sources of varying angular sizes. Because such a telescope arrangement has a near-isotropic response, it is a good compromise for a source not exactly at zenith, and for Earth rotation synthesis and lower-elevation observations (third consideration). Slight, random perturbations from the perfectly symmetric Reuleaux triangle shape further break rotational symmetry, though ring- or ellipse-like configurations may be more desirable for low-declination observations [90].

However, the fourth consideration favors some built-in degeneracy for an EPIC array layout (e.g. in a square lattice or Y-shaped configuration) due to the aforementioned n_{arr} scaling of the signal-to-noise ratio for degenerate baselines. Furthermore, studies for optimal interferometric configurations have focused largely on the case of narrow-bandwidth radio interferometers; an EPIC array with good spectroscopic capabilities would have a broadband response, i.e. any *single* baseline would densely cover a “radial spoke” in Fourier space over an octave or more, which may affect the optimal array layout, and is an interesting topic for future study.

3.2 Observational Procedure

In sections 2.4 and 4, we implicitly assume that the source separation vector $\boldsymbol{\theta}_{ba}$ is already roughly known, and then study the ultimate light-centroiding capabilities and applications of a pair of EPIC telescopes. In practice, however, $\boldsymbol{\theta}_{ba}$ may only be predetermined to some precision $\sigma_{\delta\theta}^{(0)}$ from prior observations. If this precision is of order the intrinsic angular resolution (or better), i.e. $\sigma_{\delta\theta}^{(0)} \lesssim \sigma_{\theta_{\text{res}}}$, then the EPIC telescopes can adjust their path extensions of eqs. 2.25 and 2.26 to have the reference angle $\boldsymbol{\theta}_{ba}^{\text{ref}}$ within about one fringe (or a few fringes) of the true separation $\boldsymbol{\theta}_{ba}$. In this case, the light-centroiding sensitivity estimates of section 2.4 apply directly.

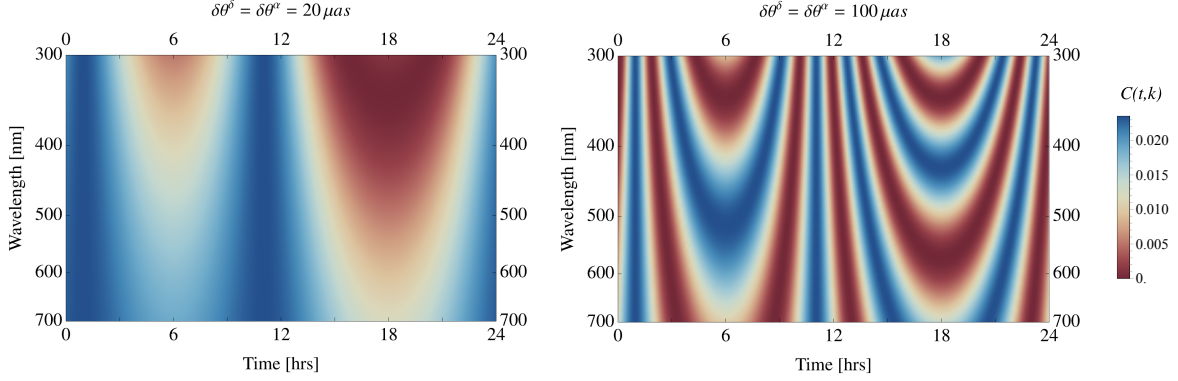


Figure 10: The expected excess fractional intensity correlation between two sources a, b of equal brightness, as a function of time and wavelength. We assume a mismatch of the reference position θ_{ba}^{ref} and the true position θ^{ba} of $\delta\theta_{ba}^{\alpha} = \delta\theta_{ba}^{\delta} = 20 \mu\text{as}$ (left) and $100 \mu\text{as}$ (right), baseline vector components $(d_x, d_y, d_z) = (1 \text{ km}, 0.5 \text{ km}, 0.5 \text{ km})$, spectral resolution $\mathcal{R} = 5,000$, and $\sigma_t = 10 \text{ ps}$.

The majority of stars and quasars on which EPIC is applicable should have good global astrometry in the *Gaia* catalog [22], which is essentially complete up to the apparent magnitudes $m_V \lesssim 15$ of interest. *Gaia* DR4 and DR5 will provide time-averaged sky localization expected at the $\mathcal{O}(20 \mu\text{as})$ level for these bright sources [91]. Relative astrometry for two sources at this precision will typically be better than Phase I’s resolution, and not much worse than the optimal resolutions of Phase II and III. This prior knowledge should thus be sufficient to unambiguously perform extended-path intensity correlation, i.e. determine $\theta_{ba} \cdot \mathbf{d}$ from the set of excess fractional intensity correlations C in each spectral channel [1].

To understand how an EPIC measurement would work in practice, let us study the time dependence of the correlator over the course of an observing night. We choose variable path extensions $\ell_1^{\text{opt}}(t)$ and $\ell_2^{\text{opt}}(t)$ according to eqs. 2.25 and 2.26 so that the $\theta_{ba}^{\text{ref}}(t)$ is consistent with the prior astrometry on the source from *Gaia*. Due to the latter’s finite precision, we will generally not satisfy eq. 2.1 *exactly*, and instead have a time-dependent difference:

$$\theta_{ba}(t) \cdot \mathbf{d}(t) - [\ell_1^{\text{opt}}(t) + \ell_2^{\text{opt}}(t)] = \delta\theta_{ba}(t) \cdot \mathbf{d}(t), \quad (3.2)$$

with $\delta\theta_{ba}(t) = \theta_{ba}(t) - \theta_{ba}^{\text{ref}}(t)$ of characteristic size $\sigma_{\delta\theta}^{(0)}$. The differential astrometric information in an EPIC observation enters through the fringes in eq. 2.28, which are proportional to:

$$\cos[k\delta\theta_{ba}(t) \cdot \mathbf{d}(t)] = \cos\left(k \left[\delta\theta_{ba}^{\delta} d_z \cos(\text{dec}) + \mathcal{A} \sin\left(\frac{2\pi t}{\text{day}} + \Phi\right) \right]\right), \quad (3.3)$$

where \mathcal{A} is defined as $\mathcal{A}^2 \equiv (d_x^2 + d_y^2) \left[(\delta\theta_{ba}^{\alpha})^2 \cos^2(\text{dec}) + (\delta\theta_{ba}^{\delta})^2 \cos^2(\text{ra}) \right]$, and Φ as $\tan \Phi \equiv \left[-\delta\theta_{ba}^{\alpha} d_y \cos(\text{dec}) + \delta\theta_{ba}^{\delta} d_x \sin(\text{dec}) \right] / \left[\delta\theta_{ba}^{\alpha} d_x \cos(\text{dec}) + \delta\theta_{ba}^{\delta} d_y \sin(\text{dec}) \right]$. The component(s) d_z (d_x, d_y) is the baseline projection towards the celestial North pole (lie in celestial equator plane), and “ra” and “dec” refer to the right ascension and declination of the source pair, while superscripts α and δ denote components along ra and dec.

As eq. 3.3 makes clear, the time variation in the argument of the correlator is coming almost exclusively from the term with amplitude \mathcal{A} (proportional to the magnitude of the

baseline in the equatorial plane) and sidereal frequency. The phase contribution from this change over an observation time t_{obs} is approximately:

$$\mathcal{O}(1) \times \left(\frac{\sqrt{d_x^2 + d_y^2}}{1 \text{ km}} \right) \left(\frac{500 \text{ nm}}{\lambda} \right) \left(\frac{\sqrt{(\delta\theta^\alpha)^2 \cos^2 \theta_a^\delta + (\delta\theta^\delta)^2 \sin^2 \theta_a^\delta}}{20 \mu\text{as}} \right) \left(\frac{t_{\text{obs}}}{10 \text{ hours}} \right). \quad (3.4)$$

In other words, for baselines at non-vanishing latitudes and with reference positions with *Gaia* uncertainties, one can expect order-unity variation in the intensity correlation throughout an observing night, with smaller wavelengths experiencing faster “fringe scanning”. We depict this effect in figure 10, where over the course of 24 hours, the excess fractional intensity correlation in each spectral channel would sweep from left to right. In practice, one would chop up the observation period into shorter intervals, such that the correlation is constant in each interval separately. The source separation $\delta\theta_{ba}$ can be extracted from fitting to the correlation in these time intervals across all spectral channels.

In some cases, the prior knowledge on the source separation may be significantly worse than the angular resolution of the EPIC pair of telescopes, but practically always better than their dynamic range: $\sigma_{\theta_{\text{res}}} \ll \sigma_{\delta\theta}^{(0)} < \sigma_{\Delta\theta}$. Poorly known separations can occur when sources are within 0.3 arcsec of each other (e.g. photometric or spectroscopic binaries, double stars, or unresolved multiple images of a strongly lensed quasar) so that they are typically not resolved in standard imaging telescopes, either due to diffraction or seeing limitations. Because the map $C \mapsto \bar{k}\mathbf{d} \cdot \theta_{ba}$ is multivalued with roughly \mathcal{R} fringes, a measurement on the correlation C in each spectral channel can correspond to $\mathcal{O}(\sigma_{\delta\theta}^{(0)}/\sigma_{\theta_{\text{res}}})$ physically viable solutions, no matter how high the signal-to-noise ratio. This (discrete) degeneracy in parameters can, in principle be broken by combining the information from all spectral channels, but this procedure can be computationally demanding given the large data volume and the motion of Earth and the source, both of which change the dot product angle $\hat{\mathbf{d}} \cdot \theta_{ba}$.

In a large *array* of EPIC telescopes, one can perform a logarithmic search for the separation vector θ_{ba} . One could use a pair of nearby EPIC telescopes (with small d or serendipitously small $\mathbf{d} \cdot \hat{\theta}_{ba}$) whose angular resolution $\sigma_{\theta_{\text{res}}}^{(1)}$ is of order the prior uncertainty $\sigma_{\delta\theta}^{(0)}$ on the source separation; this first pair of EPIC telescopes would then improve the relative light-centroiding precision to $\sigma_{\delta\theta}^{(1)}$, an improvement over $\sigma_{\theta_{\text{res}}}^{(1)} \sim \sigma_{\delta\theta}^{(0)}$ by a factor roughly equal to the SNR (see eq. 2.50). A second pair of telescopes with a larger projected baseline $\mathbf{d} \cdot \hat{\theta}_{ba}$ and corresponding resolution $\sigma_{\theta_{\text{res}}}^{(2)} \sim \sigma_{\delta\theta}^{(1)}$ could then improve the light-centroiding precision to $\sigma_{\delta\theta}^{(2)}$, and so on. An EPIC array could thus “zoom in” on the source separation quite efficiently, reaching its ultimate operating point near the main fringe with only a logarithmically large number of steps, since the relative centroiding precision improves as $\mathcal{O}(\text{SNR}^n)$ after n iterations. Fortunately, this should be possible in Reuleaux triangle, circular, and Y-shaped array configurations, which have centrally condensed response functions, i.e. dense Fourier coverage at small spatial frequencies [87, 90]. This protocol would be robust but bring some overhead to the observation time of any new pair of unresolved sources.

3.3 Photodetectors

The foremost requirement for (extended-path) intensity interferometry is a very fast photon counter. The fringe contrast scales as $C \propto 1/\sigma_t$ and the overall SNR as $\propto 1/\sqrt{\sigma_t}$, where σ_t is the standard deviation for the differential photon arrival time, which includes the timing resolution of both detectors, readout electronics, and synchronization errors, cfr. eqs. 2.8.

The timing precision of photodetectors is conventionally quantified by their time jitter t_{jitter} , the full width at half maximum (FWHM) of the signal curve as a function of time. For ease of comparison, we assume the signal curve is Gaussian, and take the standard deviation for a single detector’s timing resolution to be $t_{\text{res}} = t_{\text{jitter}}/(2\sqrt{2\ln 2})$. Assuming the readout electronics are not the bottleneck and both telescopes share the same type of photodetector, then the *relative* timing precision from eq. 2.8 will be $\sigma_t \simeq t_{\text{jitter}}/(2\sqrt{\ln 2}) \approx 0.72 t_{\text{jitter}}$.

In addition, we require that the photodetectors have a sufficiently small reset time t_{reset} , i.e. the “dead time” the detector needs to revert to its original state after a single-photon absorption event. The classes of photodetectors with the best timing jitters typically cannot distinguish between single-photon or multiphoton events (in contrast to photon-number-resolving devices). A reset time (much) smaller than the typical time separation between photon events (in each spectral channel) is thus necessary to have a high duty cycle and not wash out intensity fringe correlations. For most sources under consideration and our assumed telescope parameters (table 1), sub-microsecond reset times $t_{\text{reset}} \lesssim 1 \mu\text{s}$ should be sufficient, see figure 11 for example.

Thirdly, we desire a high quantum efficiency η_p (cfr. eq. 2.43) to maximize the SNR (eq. 2.49) and light-centroiding precision (eq. 2.51). The fact that each photodetector pixel is only responsible for reading out a narrow bandwidth is advantageous in this regard, as each pixel can be tuned to maximize the photodetection efficiency in that particular spectral channel.

Finally, photodetectors in general will have spurious events at rate known as the dark count rate (DCR), which may arise intrinsically (e.g. from electronic noise) or environmentally (from cosmic rays, blackbody radiation, stray light, etc.). Some environmental backgrounds can be partially shielded by an appropriate spectral filter on the pixels, as each pixel of the photodetector only needs to read out a narrow band. However, the tolerances on the DCR are somewhat loose, as the relatively large photon flux from the sources of interest constitutes our main source of statistical noise: in the sea of incoming photons, we are searching for those very rare photon pairs that simultaneously (after correcting for propagation differences) impinge on both telescopes. The DCR is not the limiting factor when below the sources’ combined photon flux. If larger, it would reduce the intensity correlation fringe contrast, as the DCR would give false positives that are uncorrelated between the two telescopes.

The above four requirements point towards to two possible technologies for single-photon detectors, namely superconducting nanowire single photon detectors (SNSPDs) and single photon avalanche diodes (SPADs), also known as Geiger mode avalanche photodiodes (GmAPD). The present state of the art for these two classes of devices is summarized below.

Given the demonstrated technology and the real-world applications of both SNSPDs and SPADs outside pristine laboratory conditions, we are optimistic that arrays of photodetectors tailored to the needs of multichannel intensity interferometry are feasible. In figure 11, we plot the photon rate in a single spectral channel of an EPIC Phase II telescope, for the same benchmark source pairs as in figure 6, showing that these rates fall between achievable DCRs and inverse reset times t_{reset}^{-1} . Ultrafast photon detection over a large array of pixels (each optimized at different wavelengths) has not been a priority of most current research efforts, but it is clear from our summaries below that the requisite technology exists, and that there is no obstacle preventing its further development. Our proposal offers unique prospects for using this cutting-edge technology for a novel use case in astronomy, and we hope the exciting scientific applications (section 4) will further intensify research and development in this area.

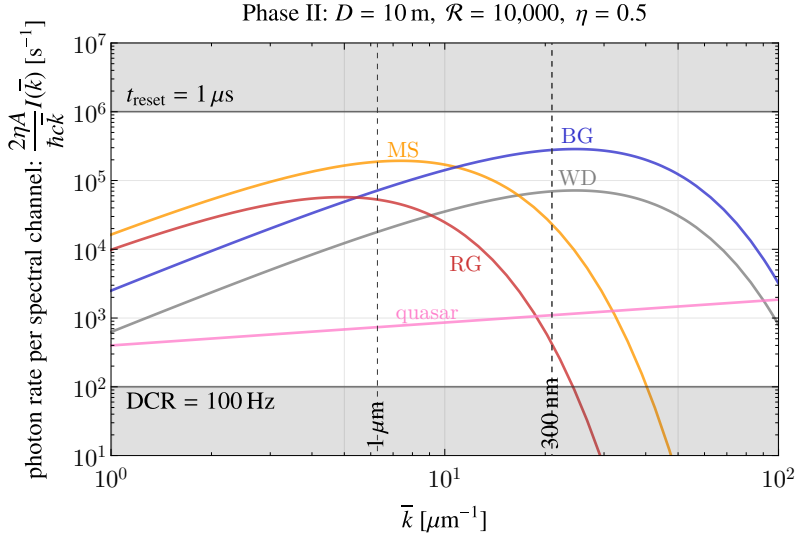


Figure 11: Rate of recorded photons per spectral channel incident on the aperture of one telescope. We use the same parameters as in figure 6 for the source pairs and Phase II detectors (also in table 1). The upper shaded region corresponds to photon rates in excess of 10^6 s^{-1} , where significant sensitivity loss would occur (due to missed photon counts) for a photodetector reset time of $t_{\text{reset}} = 1 \mu\text{s}$. Likewise, the lower shaded region corresponds to source photon rates below the dark count rate (DCR) of the photodetector, where loss of fringe contrast and thus sensitivity would occur because dark counts from electronic noise are uncorrelated. If N_{subap} subapertures are used, then photon rates are reduced by a factor of N_{subap}^{-1} , weakening the reset time constraint but tightening the DCR requirement.

Superconducting Nanowire Single Photon Detectors

Single photon detection with superconducting nanowires, first developed about two decades ago, is a technique with extraordinary promise for quantum optics and many other applications, owing to picosecond-level timing jitter, sub-millihertz DCR, near-unity quantum efficiency, sub-nanosecond recovery times [92, 93], and ability to operate from the infrared (IR) to optical range [94] and even in the ultraviolet (UV) [95]. The physical principle upon which SNSPDs operate is simple: after absorption of a single photon by the superconducting nanowire, a large number of Cooper pairs are broken, inducing a local hotspot in the normal, non-superconducting phase. A bias current is applied so that this hotspot subsequently expands due to Joule heating, further increasing the resistance, generating a voltage pulse that can be amplified and registered with room-temperature electronics. The energy of the hotspot is made to dissipate quickly thereafter to return the nanowires back to their superconducting state.

The system timing jitter for single SNSPDs has steadily improved over the last decade, from 18 ps (15 ps intrinsic) [96] to as low as 2.6 ps for 400 nm and 532 nm visible light with a niobium nitride (NbN) nanowire at 0.9 K operating temperatures [94], with possible further improvements. Recently, SNSPDs have made further advances, from the UV to the IR. A UV SNSPD with an active area of $56 \mu\text{m}$ in diameter was demonstrated to have a timing jitter down to 62 ps, a system efficiency of up to 84% for narrowband designs, a DCR of 0.25 counts/hr, and detector dead time less than 250 ns [95]. On the other side of the spectrum,

a free-space coupled NbN SNSPD was shown to have a 14 ps time jitter, a DCR below 0.1 Hz, a system efficiency of up to 84%, with an active area of $22 \times 15 \mu\text{m}^2$ at 1550 nm wavelengths [97]. Optimization of the system’s design and fabrication can push photodetection efficiencies as high as 98% [98], and with tungsten silicide (WSi) nanowires, the energy threshold can be lowered to perform single-photon detection at 10 μm wavelengths.

Multiplexing SNSPDs into arrays with many pixels—while simultaneously retaining their exquisite performance—presents new challenges. To date, the largest realized SNSPD array consists of 32×32 pixels with a row-column multiplexing architecture [99], optimized at 1550 nm with an area of $1.6 \times 1.6 \text{ mm}^2$ ($0.96 \times 0.96 \text{ mm}^2$ active area) and operated at 0.73 K, which exhibited a timing jitter of at least 250 ps. Due to the small filling factor and low pixel efficiency, the combined system efficiency was only 8%, but there are clear paths to improve these factors [99], and other thermal-coupling array designs may be scaled into the megapixel range [100]. The array cannot distinguish between photons that impinge on the detector with a relative arrival time less than the timing jitter. Saturation of the photodetector array restricts the maximum apparent brightness of sources, as we illustrate in figure 11. We should note that lab measurements using this array were done over second-long timescales, so scaling up to hours of observation is yet to be demonstrated. Finally, we note that a *single* nanowire alone can serve *multiple* pixels using time-of-flight information: ref. [101] reports a 50 ps timing jitter at 405 nm and MHz photon counts, with one wire resolving 590 effective pixels. Large SNSPD arrays with active areas up to $3.1 \times 3.1 \text{ mm}^2$ have been considered for use in exoplanet transit spectroscopy [102] (e.g. on the Origins space telescope [103]), for which exceptional photometric stability is required in the IR range of 2.8–20 μm .

Single Photon Avalanche Photodiodes

A SPAD is a diode operated well above its reverse-bias breakdown voltage. Because of the very large internal electric field, a single photoelectron is accelerated to energies sufficiently high to ionize other electrons in its path, thus creating a self-sustaining avalanche, which is registered as a “click” (hence the Geiger mode monicker). The detector’s dead time is set by the timescale for quenching the avalanche current and restoring it back to the operating bias.

Already in 2008, single SPADs 20 μm in diameter could reach efficiencies up to 42% with a timing jitter of 39 ps, kHz-level DCR, and reset times of about 600 ns [104]; ten years later, these performance numbers were improved with a 10–80 μm diameter bipolar-CMOS-DMOS SPAD to $t_{\text{jitter}} \approx 28$ ps, $\eta = 70\%$, $t_{\text{reset}} = 50$ ns at 820 nm and operating temperature of -20°C [105]. The envelope continues to be pushed, with reports of 8.7 ps timing jitters up to MHz count rates [106], and further improvements on the horizon.

SPADs have been assembled into arrays as large as 256×256 , with demonstrated timing jitters of 300 ps, reset times of 100 ns, 70% efficiency, and DCR of 10 Hz [107]. These arrays can be manufactured to support Gbit/s data rates (relevant for telecommunications), which is on the order of the photon fluxes relevant even for Phase 3 dishes of EPIC. [107]. The Europa Lander astrobiology mission is to be equipped (as part of its LIDAR system) with a 2048×32 array of Si SPADs with a DCR of 4.5 kHz, peak detection efficiency of 70% at 532 nm [108], and timing jitter target of 250 ps [109]; a smaller 1024×32 version for the Europa Lander Sensor Array brought the latter figure down to 33 ps [110].

3.4 Dispersive element

As discussed in section 3.3, despite major leaps in timing resolution of modern single-photon counters, the relative timing uncertainty σ_t is still much larger than the period of electro-

magnetic waves in the optical band. The fringe contrast in intensity interferometry increases with decreasing spectral width σ_k (eq. 2.11). For a (point-like) source with a broad spectrum, we thus have $C \sim 1/c\sigma_k\sigma_t$, but the flux is reduced as $I \propto \sigma_k$. For a *single* spectral channel, this implies that the SNR is independent of σ_k (eq. 2.48). However, by combining *multiple* spectral channels of width σ_k across an ϵ -fold around wavenumber \bar{k} , the signal-to-noise ratio can be enhanced as $\text{SNR} \propto (\bar{k}/\sigma_k)^{1/2} = \mathcal{R}^{1/2}$, as derived in eq. 2.49. The most natural way to spectrally split the incoming light is via a dispersive prism or a diffraction grating, as in modern spectrographs. In the following, we perform a simplified analysis of this spectroscopic procedure and note some associated challenges unique to intensity interferometry.

The main (and perhaps surprising) result of this section is that the intensity correlation for a multichannel intensity interferometer can receive an additional suppression for large-aperture telescopes and excellent spectral and timing resolution. Without mitigating solutions discussed below, the excess fractional intensity correlation in any one spectral channel parametrically scales as:

$$C \sim \min \left\{ 1, \frac{1}{c\sigma_k\sigma_t}, \frac{\theta_{\text{diff}}}{\theta_{\text{seeing}}} \right\}, \quad (3.5)$$

which is also depicted in figure 12. Comparing to e.g. eq. 2.11, the fractional correlation is limited by the ratio of the diffraction-limited angle $\theta_{\text{diff}} \equiv 2\pi/\bar{k}D$ of a single telescope to the seeing angle θ_{seeing} (eq. 2.63). This correlation ceiling would be the limiting factor for the large-aperture telescopes with high spectral resolution and exquisite timing resolution in all three EPIC Phases of table 1. We conclude this section with possible solutions that can recover the sensitivity assumed throughout section 2, i.e. remove the $\theta_{\text{diff}}/\theta_{\text{seeing}}$ ceiling in eq. 3.5.

In order to illustrate this potential suppression as lucidly as possible, we study the following simplified setup: a plane wave incident on a grating of size Nd_g , with d_g the periodicity of the grating and N the number of (illuminated) slits. We concern ourselves only with the first diffraction peak focused onto a photodetector array, of which a single pixel records the wavenumbers $k \in [\bar{k} - \sigma_k/2, \bar{k} + \sigma_k/2]$, with $\sigma_k \equiv \bar{k}/\mathcal{R}$. In appendix C, we carry out the full calculation within scalar diffraction theory in great detail, from the point of incidence on the primary mirror to the photodetector array.

The electric field at wavenumber k far away from a diffraction grating is given by the standard result [111]:

$$E_k(\theta_F, t) \propto A_k \frac{\sin(k\theta_F Nd_g/2)}{\sin(k\theta_F d_g/2)} e^{-ikt}, \quad (3.6)$$

with $\theta_F \equiv x_F/f_c$, where x_F is the physical linear coordinate on the photodetector, f_c the focal length of the camera which focuses the collimated light from the grating onto the photodetector, and A_k the field amplitude at wavenumber k . The first diffraction peak at wavenumber \bar{k} occurs at $\theta_F \simeq \bar{\theta}_F \equiv 2\pi/(\bar{k}d)$ (in the small-angle approximation). We are free to redefine $\theta_F \rightarrow \bar{\theta}_F + \theta_F$ so that $\theta_F = 0$ corresponds to the center of the pixel corresponding to the spectral channel centered at \bar{k} . This pixel subtends a small angular width equal to $\bar{\theta}_F/\mathcal{R}$. With this redefinition of θ_F and expanding $\sin x \simeq x$ at $x \ll 1$, the electric field has the form:

$$E_k(\theta_F, t) \propto A_k \frac{\sin[k\theta_F Nd_g/2 + \pi N(k/\bar{k} - 1)]}{k\theta_F Nd_g/2 + \pi N(k/\bar{k} - 1)} e^{-ikt}. \quad (3.7)$$

Writing the intensity correlation as $C = \frac{\langle I_1(0)I_2(t) \rangle}{\langle I_1 \rangle \langle I_2 \rangle} - 1 \equiv \frac{\mathcal{N}}{\mathcal{D}}$, we find for the numerator \mathcal{N} and denominator \mathcal{D} :

$$\mathcal{N} \propto \int \frac{dt}{\sigma_t} \iint d\theta_{\text{F}}^{(1)} d\theta_{\text{F}}^{(2)} \iint dk dk' E_k(\theta_{\text{F}}^{(1)}, 0) E_{k'}^*(\theta_{\text{F}}^{(1)}, 0) E_k^*(\theta_{\text{F}}^{(2)}, t) E_{k'}(\theta_{\text{F}}^{(2)}, t), \quad (3.8)$$

$$\mathcal{D} \propto \left| \int d\theta_{\text{F}} \int dk |E_k(\theta_{\text{F}}, 0)|^2 \right|^2, \quad (3.9)$$

where the superscript (p) labels the telescope $p = 1, 2$ location of the pixel. For simplicity, we incorporate the relative timing uncertainty via a uniform distribution of width σ_t . Both expressions contain four factors of the electric field in eq. 3.7. The numerator involves products of electric fields with different wavenumbers k and k' at each telescope. In contrast, the denominator is simply the product of the average intensities at each telescope, involving products of electric fields with the *same* wavenumber at each telescope. A heuristic understanding of the suppression effect is thus that large pixels—larger than the diffraction limit—contain several spatially non-overlapping electromagnetic modes with *independent* temporal fluctuations, so that $C = \mathcal{N}/\mathcal{D}$ does *not* attain the limit $C \rightarrow 1$ as $\sigma_t \rightarrow 0$.

We can gain some (analytic) intuition by taking the size of the pixels to be large (formally infinite) while simultaneously endowing A_k with (uniform) support only over a wavenumber range of width σ_k .² In this limit, which turns out to be a reasonable approximation, we find (see appendix C.4):

$$C = \frac{\mathcal{N}}{\mathcal{D}} \simeq \frac{2}{\sigma_k^2} \int_0^{\sigma_k} d\sigma (\sigma_k - \sigma) e^{-\frac{1}{2}\sigma^2\sigma_t^2} \left[\frac{\sin \sigma/\sigma_d}{\sigma/\sigma_d} \right]^2. \quad (3.10)$$

This integral consists of a convolution of two effective “filters”: one Gaussian filter with a bandwidth σ_t^{-1} , and one sinc-squared filter with bandwidth $\sigma_d \equiv \bar{k}/(\pi N)$. In the limit of poor timing resolution, $(c\sigma_t)^{-1} \ll \sigma_d$, the latter filter is nearly unity over the integration range, and we recover the standard result $C \sim 1/c\sigma_k\sigma_t$ (from e.g. eq. 2.11). However, in the opposite limit $(c\sigma_t)^{-1} \gg \sigma_d$ of good timing resolution, it is the Gaussian filter that is unity, yielding $C \sim \pi\sigma_d/\sigma_k \ll 1/c\sigma_k\sigma_t$.

The pixel corresponding to the spectral channel centered on \bar{k} subtends an angle $\bar{\theta}_{\text{F}}/\mathcal{R}$ to capture wavenumbers in the range $k \in [\bar{k} - \sigma_k/2, \bar{k} + \sigma_k/2]$, but it also needs to be sufficiently large to contain the entire seeing disk of the source(s). Atmospheric aberrations cause a spatial spread (which furthermore fluctuates on millisecond time scales) on the order of the magnified seeing angle $\theta_{\text{seeing}}f/f'$. The illuminated area of the grating has a linear size Nd_{g} which is related to the aperture diameter D of the telescope by the same (inverse) magnification factor (the focal length ratio of primary and secondary mirrors): $Nd_{\text{g}} = Df'/f$. These relations imply that containment of the seeing disk is equivalent to:

$$\frac{\bar{\theta}_{\text{F}}}{\mathcal{R}} \gtrsim \frac{f}{f'} \theta_{\text{seeing}} \Leftrightarrow \frac{N}{\mathcal{R}} \gtrsim \frac{\theta_{\text{seeing}}}{\theta_{\text{diff}}} \approx 40 \left(\frac{D}{4 \text{ m}} \right) \left(\frac{500 \text{ nm}}{\bar{\lambda}} \right) \left(\frac{\theta_{\text{seeing}}}{1 \text{ arcsec}} \right), \quad (3.11)$$

which is nothing more than the usual requirement in spectroscopy that gratings have to be oversized in practice to account for seeing, since atmospheric fluctuations reduce the grating’s

²In practice, the spectral width σ_k of the pixel is linearly proportional to its angular size, so this limit is not physical—we only provide it for illustrative purposes.

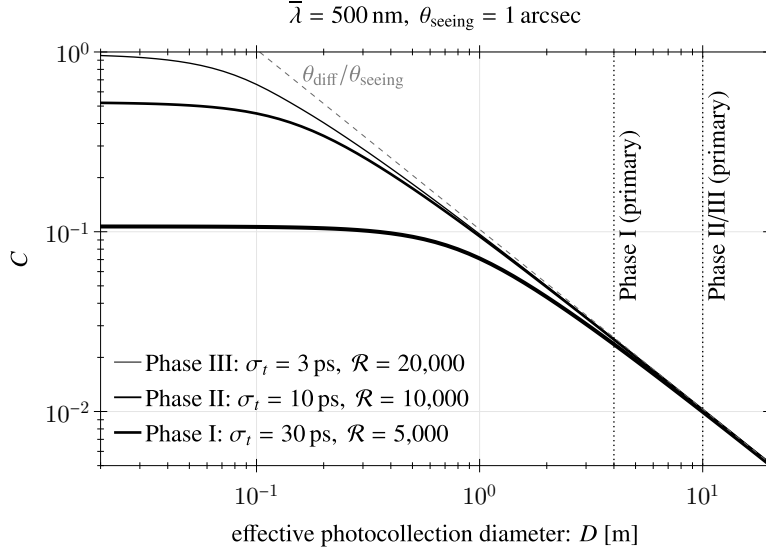


Figure 12: Intensity correlation of eq. 3.10 for a single pixel whose central wavelength is $\bar{\lambda} = 500$ nm, as a function of the effective linear size of the photocollection element, and assuming a seeing angle of $\theta_{\text{seeing}} = 1$ arcsec. We plot this correlation for the timing and spectral resolutions σ_t and \mathcal{R} assumed for Phases I, II, and III of EPIC. The horizontal axis can be read either as the diameter of the primary mirror (vertical black dashed lines) for a setup with only one photodetector array, or as the linear subaperture size in the spectroscopic direction (see “Potential Solutions” below). The spectroscopic suppression of $C \sim \theta_{\text{diff}}/\theta_{\text{seeing}}$ (gray dashed line) is the limiting factor for $D \gtrsim 2\pi c\sigma_t/\mathcal{R}\theta_{\text{seeing}}$. The ideal subaperture size is roughly this threshold value: 1 m, 0.2 m, and 0.1 m for EPIC Phases I, II, and III, corresponding to a number of subapertures of $N_{\text{subap}} \sim 4, 50, 100$.

nominal resolution N to the much smaller effective resolution \mathcal{R} . When this inequality is saturated— $N/\mathcal{R} \simeq \theta_{\text{seeing}}/\theta_{\text{diff}}$ —then the suppression found in eq. 3.10 is equal to:

$$C \leq \frac{\pi\sigma_d}{\sigma_k} \simeq \frac{\theta_{\text{diff}}}{\theta_{\text{seeing}}}, \quad (3.12)$$

i.e. the parametric upper bound stated in eq. 3.5 in the beginning of the section. In figure 12, we show that Phase I of EPIC would already be limited by (and saturate) eq. 3.12, and thus not achieve its theoretical SNR without modification; the suppression would be even worse for Phases II and III.

Potential solutions

There are at least two (and possibly more) straightforward solutions to mitigate this spectroscopic suppression, albeit at the expense of additional complexity and cost.

The first and simplest strategy is to use multiple N_{subap} subapertures in each EPIC telescope, since the correlation ceiling from eq. 3.12 scales as $C \propto \theta_{\text{diff}}$ and thus with the inverse linear size of photocollection. One could take the configuration from figure 5b, and after the path-extension stage, geometrically split the light with N_{subap} separate gratings, focusing mirrors, and photodetector arrays. Each photodetector array would thus have a smaller effective photocollection size (in the spectroscopic direction), and operate near its nominal

fringe contrast of $C \sim 1/c\sigma_k\sigma_t$ with the appropriate subaperture number $N_{\text{subap}} \sim 4, 50, 100$ for Phases I, II, III, respectively (see figure 12).³ The advantages of this approach are that tolerances on the primary and secondary mirrors are not severe, and that the photodetector reset time constraints are relaxed by a factor N_{subap}^{-1} . The disadvantage (besides cost and complexity) is that the photodetector DCR requirements are more stringent by the same factor N_{subap}^{-1} .

A second potential solution is the employment of adaptive optics (AO), a well-established technology to recover the diffraction limit of the telescope by using wavefront sensors and thin deformable mirrors to cancel atmospheric aberrations. AO is already in use on many spectrographs (see ref. [113] for a review). In an EPIC context, this would allow for pixel sizes $\bar{\theta}_F/\mathcal{R} \simeq \theta_{\text{diff}}$, for which the spectroscopic suppression from eq. 3.12 does not occur. The advantage of this approach is that it can allow for even higher spectral resolutions ($\mathcal{R} \gtrsim 100,000$) and correspondingly larger fringe contrast C . This elegant approach would however require tight tolerances on the polishing of *all* optically active surfaces, and come at considerable cost especially for large apertures.

Besides those brute-force approaches, there may exist a method to correct for these intra-pixel dispersive phases with clever optical configurations, possibly consisting of arrays of microlenses and/or micropisms, which have demonstrated lenslet pitch on the order of tens of microns to fit SNSPD or SPAD pixel sizes [114]. Any such optical elements would have to cancel the relative propagation phases of a fractional wavenumber range of order $1/\mathcal{R}$, i.e. “undo” the spectral splitting within the pixel itself so that $\mathcal{N} \simeq \mathcal{D}$ in the limit $\sigma_t \rightarrow 0$ in eqs. 3.8 and 3.9.⁴ We have checked that simple modifications—defocusing, recollimating the light onto the pixel, irregular gratings, or a non-co-phased segmented mirror—by themselves do not resolve the spectroscopic suppression. We leave investigations of possible clever optical configurations to future work.

3.5 Tolerances

Optical tolerances

One of the attractive features of intensity interferometry is the mildness of the required tolerances on the telescope optics, in stark contrast to the tight tolerances for imaging telescopes and (especially optical) amplitude interferometers. In the simplest realization of intensity interferometry, without spectral splitting nor path extension, the primary requirement is that the wavefronts in either telescope do not acquire relative path differences (or equivalently, time delays) larger than the relative timing resolution σ_t of the photodetectors. The phototubes used at the NSII in the 1970s had electronic bandwidths on the order of 60 MHz [37] or timing resolutions of $\sigma_t \sim 10$ ns. This poor timing translated to a tolerance on the order of a meter on the location of the receivers, and was therefore clearly not the limiting factor of the observatory. Even for our Phase III parameter of $\sigma_t = 3$ ps, significant loss of contrast can be avoided as long as there are no relative path differences greater than a millimeter, about 4–5 orders of magnitude above the sub-wavelength rms error needed for conventional diffraction-

³A related technique involves correlation of sub-pupil intensities to perform aperture synthesis [112].

⁴A minimal configuration would be a diverging lens to recollimate the beam, a corrective dispersive element such as a micropism, and potentially a final refocusing lens, all directly above each pixel. A simple calculation of the requirements of the micropism dictates resolving power $b \frac{dn}{d\lambda} = N$, where b is the base of the prism and n its index of refraction, which should be accurate to about one part in N/N_{eff} , where $\sigma_t \equiv \bar{k}/\pi N_{\text{eff}}$, i.e. $N_{\text{eff}} \sim 15,000$ for a 10 ps timing resolution. The feasibility of achieving this on the scale of individual pixels is left to future study.

limited astronomical observations. For the same reason, intensity interferometry is also quite immune to atmospheric distortions and delays (section 2.5).

The elements with the most stringent tolerances of (multichannel) EPIC fall into two categories: those that may cause differential phases to the light from both sources, and those with common effects. The path extension belongs to the former, as it is designed to (spatially) split the light from both sources: the two-photon amplitude depicted in the left panel of figure 2 corresponds to the fringe useable for wide-angle differential astrometry (cfr. eqs. 2.25 and 2.26). Therefore, the relative path length ℓ_p needs to be *known* in each telescope $p = 1, 2$ to a fraction of a wavelength. In principle, it needs to be *adjustable* to within a range of order σ_k^{-1} from the optimal values of eqs. 2.25 and 2.26 to maintain fringe contrast, though it is advisable in practice to keep it well within that range to avoid fringe confusion. These considerations apply to the two beamsplitters and two reflecting flat mirrors of the path extension module. We provide a simple analysis of the beamsplitters in appendix C.2, where we also elaborate on additional phases from the splitters' finite width and index of refraction, which also need to be characterized to achieve optimal operation of an EPIC interferometer.

Optical elements that affect the light of both sources simultaneously—the primary and secondary mirrors, diffraction grating, and camera—should be positioned and polished well enough for the resulting image to fit within the pixel corresponding to each spectral channel, so that the desired spectral resolution \mathcal{R} is achieved. This tends to be a significantly stricter requirement than the aforementioned polishing to within σ_t ; numerically, it amounts to upper bounds on primary aberrations of $\mathcal{O}(\text{few } \mu\text{m})$ for the parameters under consideration. This is a much looser requirement than on conventional imaging telescopes aiming to achieve diffraction-limited resolution: tolerances on an EPIC telescope are looser by a factor of about $f'D/f\bar{\lambda}\mathcal{R} \sim 200$ for $D = 10\text{ m}$, $\bar{\lambda} = 500\text{ nm}$, $f/f' = 10$ and $\mathcal{R} = 10,000$, the fiducial parameters for EPIC Phase II. We provide a more detailed account on effects from aberrations in appendix C.3. These less restrictive tolerances imply that some of the expensive and time-consuming aspects of conventional large-mirror polishing could be skipped [115], helping to make the cost-effective construction of large EPIC arrays a realistic goal.

As we explained in section 3.4, our assumed spectral resolution in combination with exquisite timing resolution may lead to a suppression in fringe contrast that has to be mitigated. The tolerance requirements mentioned above are for optical configurations than can correct for this intra-pixel dispersion. If one decides to solve the issue raised in section 3.4 via multiple sub-apertures, then the requirement is that the aberrations yield an image for a point source that is no larger than the seeing disk. If one employs adaptive optics instead, then the aberration requirements tighten to those of a conventional imaging telescope operated at the diffraction limit.

Geodety, synchronization, and calibration

Extracting astrometrically useful information (such as the angle θ_{ba} between two sources) from the intensity correlation C requires excellent geodety and synchronization—a precise knowledge of the relative positions (i.e. baseline $\mathbf{d} = \mathbf{r}_2 - \mathbf{r}_1$) and times (i.e. timing offset $\tau = t_2 - t_1$) at each telescope. These techniques have been developed in support of VLBI programs over decades and continue to improve [116, 117].

Geological shifts, tides, and Earth's precession and nutation can cause drifts in the relative positions of the telescopes to each other as well as to the celestial reference frame, typically on the order of centimeters per year [117]. Accurate geodetic data are thus key for accurate measurements, since the baseline \mathbf{d} is to be known to a precision of $c\sigma_t$ (about

1 cm for Phase I, and 1 mm for Phase III, cfr. table 1). On the 1 km–100 km scale of the baselines considered here, the requirements are somewhat less stringent compared to VLBI. In particular, for sources observed near zenith, the vertical motion of Earth’s surface, which is less precisely known, contributes subdominantly to the differential astrometric phase of interest ($\bar{k}\boldsymbol{\theta}_{ba} \cdot \mathbf{d}$). The VLBI global geodetic measurements are planned to improve by an order of magnitude compared to current precision as part of the next-generation VLBI Global Observing System (VGOS) [118, 119], which is currently being implemented. A geodetic analysis of the data from a recent demonstration of a subset of the VGOS system yielded a root-mean-square deviation of the baseline length residuals about the weighted mean of 1.6 mm [120]. The expected improvements will result in residual path length errors of order a millimeter, or timing precision of a few picoseconds across the globe [121], sufficient for the anticipated tolerances for EPIC.

The fast photon detection and short intensity fluctuation times set stringent requirements on the timing stability of the telescopes. In particular, the timing offset between the two telescopes needs to be known to a precision better than the quadrature sum of the photodetectors’ timing resolutions (cfr. eq. 2.8) in order to be a subleading cause for fringe contrast loss. A relative synchronization of $\sigma_t \lesssim 10$ ps over an integration time of $t_{\text{obs}} = 10^4$ s corresponds to a required Allan deviation of 10^{-14} . For shorter baselines, it may be possible to achieve this by sharing a common frequency reference, but for longer baselines, each telescope (site) needs to be equipped with its own high-precision atomic clock. Allan deviations at this level are achievable with commercially available hydrogen masers, both active [122] and passive [123], and are employed and tested by e.g. the Event Horizon Telescope [28].

If $\text{SNR} > 1$ can be achieved on the intensity correlation fringe on shorter integration times with large apertures and/or bright sources, the requirements on the timing stability can be relaxed, making possible the use of cheaper rubidium [124, 125] or cesium [126] frequency standards, which in commercial packages can have Allan deviations down to $\mathcal{O}(10^{-13})$. We note that in addition to the time-delayed (ghost) intensity correlation fringe at e.g. $\ell = \ell_1^{\text{opt}}$ and $\ell' = -\ell_2^{\text{opt}}$ most useful for relative astrometry, one can also employ the “main” intensity correlation fringe in the first line of eq. 2.24, which has about *four* times the contrast of the ghost fringe and can thus be detected *sixteen* times faster (at the same SNR). This main fringe can be used to self-calibrate and tease out any drifts in baseline and time difference, and can therefore ensure the telescopes’ clocks remain synchronized over the course of the observation.

Finally, each telescope’s optical path and path extension needs to be calibrated and regularly monitored. This can be done experimentally with a known light source (e.g. laser) at the other “input ports” on the right of the beamsplitters in figure 5b. A calibration should measure (frequency-dependent) phase shifts from propagation *within* the beamsplitter, the distance w_p , and angles γ and γ' . Likewise, the mapping of pixels to wavelengths needs to be established, but this is a standard procedure in spectroscopy, and can be performed by observation of a bright source with a known spectrum.

4 Applications

Historically, stellar intensity interferometry has mainly been used to investigate the morphology of bright emission regions. In particular, one can determine stellar radii and shapes (projected on the celestial sphere) to high precision, and study star spots, stellar winds, and limb darkening, which are all quantified by the form factors $\mathcal{F}(\bar{k}, \mathbf{d})$ in eq. 2.34. For more

information, we refer the reader to the classic intensity interferometry papers on this subject cited in section 1. Emission region morphology studies of *single sources* are also possible in an extended path intensity correlator, *at the same time as differential astrometric measurements between two sources*. For example, one can collect data for differential astrometry on two sources a and b , and afterwards select the appropriate fringe by adjusting τ for the desired application. For differential astrometry, one would use τ equal to that of eq. 2.27, while the emission morphology of source $j = a, b$ could be investigated by taking e.g. $\tau = -\hat{\boldsymbol{\theta}}_j \cdot \mathbf{d}/c$ (cfr. eq. 2.24), as well as potentially other fringe combinations.

In this section, we present a (partial) science case for the differential astrometry capabilities of an extended-path intensity correlator (see ref. [127] for a general overview). The path-extension modification of an intensity interferometer increases its effective field of view up to a few arcseconds, limited by atmospheric fluctuations, cfr. figure 9. This (literally and figuratively) increases the scope of stellar intensity interferometry, enabling *extreme-precision differential astrometry between two widely separated sources*, with the hierarchy: $\sigma_{\delta\theta} \ll \sigma_{\text{res}} \ll \theta_{ba} \lesssim \theta_0$. In other words, the light-centroiding precision $\sigma_{\delta\theta}$ from eq. 2.51 is much better than the angular resolution $\sigma_{\theta_{\text{res}}}$ from eq. 2.9, which can be orders of magnitudes smaller than the source separation θ_{ba} . The fringe is still detected at maximum contrast as long as the sources are separated by less than the isoplanatic angle θ_0 from eq. 2.61.

We identify five use cases where differential astrometry between two bright sources with EPIC has the potential to provide unprecedented accuracy and precision, opening up new prospects for astrophysical and cosmological measurements. The five use cases are: binary-orbit characterization (section 4.1), exoplanet detection (section 4.2), stellar acceleration measurements (section 4.3), stellar microlensing (section 4.4), and quasar microlensing by low-mass dark matter halos (section 4.5). This last signature is entirely new, and will be explored in more detail in a follow-up paper [128]. This list of applications is almost certainly not exhaustive, but hopefully sufficient to motivate research and development in support for EPIC Phase I and subsequent Phases with larger apertures and arrays and/or better spectroscopy and timing.

4.1 Binaries

Differential astrometry over a narrow field of view is ideally suited to characterization of binary orbits, since the two sources are automatically nearby, and orbital measurements only demand good precision on the *relative* separation of the sources. Close binary characterization and distance measurement was already achieved in the early days of intensity interferometry [42]. Our EPIC setup allows for observation of binary pairs that are much more widely separated and fainter.

With data only from an intensity interferometer, the period P and all angles (including inclination) of the binary orbit can be determined. With additional spectroscopic radial-velocity measurements of each of the binary constituents, the full Keplerian orbit can be fixed without degeneracies, including the masses M_a , M_b , and the line-of-sight distance D_s to the binary. We first review some basic notation of binary orbits, and then present mock analyses on potential binary targets.

Let $\mathbf{r} \equiv \mathbf{r}_b - \mathbf{r}_a \equiv \{x, y, z\}$ be the relative separation between the two sources in the observer's frame, with z denoting the line-of-sight direction. In this frame, we can describe any Keplerian orbit of period P with the six orbital elements: semi-major axis a , eccentricity

e , inclination i , longitude of ascending node Ω , argument of periapsis ω , and true anomaly ν :

$$x = r [\cos \Omega \cos(\omega + \nu) - \sin \Omega \sin(\omega + \nu) \cos i]; \quad (4.1)$$

$$y = r [\sin \Omega \cos(\omega + \nu) + \cos \Omega \sin(\omega + \nu) \cos i]; \quad (4.2)$$

$$z = r [\sin(\omega + \nu) \sin i]. \quad (4.3)$$

The separation r evolves as $a(1-e^2)/(1+e \cos \nu)$. With that substitution, all time dependence is encapsulated through the variation of the true anomaly ν , which is related to the eccentric anomaly E , and to the mean anomaly \mathcal{M} evolving linearly in time t as:

$$\nu = 2 \arctan \left\{ \sqrt{\frac{1+e}{1-e}} \tan \frac{E}{2} \right\}; \quad E - e \sin E = \mathcal{M} = \frac{2\pi}{P}(t - t_0), \quad (4.4)$$

where t_0 is the reference epoch.

With 7 or more purely astrometric measurements (ideally spaced out roughly evenly over the orbit) obtained by an intensity interferometer, which can only measure the projected angles on the sky, namely $\{x/D_s, y/D_s\}$, one can fit for the six “dimensionless” orbital elements $\{a/D_s, e, i, \Omega, \omega, t_0/P\}$ and one dimensionful quantity, the orbital period $P = 2\pi a^{3/2}(GM)^{-1/2}$ with $M = M_a + M_b$ the total mass. However, there would always remain one size-distance-mass degeneracy along the “direction” $a \propto D_s \propto (GM)^{1/3}$. This final degeneracy can be broken with radial velocity measurements of the constituents: \dot{z}_a and \dot{z}_b . Their difference $\dot{z}_b - \dot{z}_a = \dot{z}$ constrains the ratio $\sqrt{a/GM}$ independent of D_s , while their ratio \dot{z}_b/\dot{z}_a (after subtracting out the time-averaged mean radial velocity of the binary’s center of mass) constrains the mass ratio M_a/M_b in direct proportionality.

As a simplified example, we perform a Markov Chain Monte Carlo (MCMC) analysis on a mock data set reminiscent of the spectroscopic binary W0135-052 composed of an unresolved but detached pair of DA white dwarfs [129, 130]. The parameters of this system are: binary period $P = 1.556$ day, effective temperatures $T_a = 7450 \pm 500$ K, $T_b = 6920 \pm 500$ K, component masses $M_a = 0.47 \pm 0.05 M_\odot$ and $M_b = 0.52 \pm 0.05 M_\odot$, velocity semi-amplitudes $K_a = 76.5$ km/s and $K_b = 66.3$ km/s, and a parallax-based distance $D_s = 12.35 \pm 0.43$ pc. The masses are only estimated after measurements of the surface gravity and assumptions about the stellar composition and mass-radius relation [130].

For simplicity, we assumed “truth parameters” for the mock data set of $P = 1.556$ day, $D_s = 12.35$ pc, velocity semi-amplitudes of $K_a = 76.5$ km/s and $K_b = 66.3$ km/s, primary mass $M_a = 0.47 M_\odot$, secondary mass $M_b = M_a K_a / K_b = 0.5423 M_\odot$, ignored the systemic line-of-sight radial velocity, and assumed a circular orbit ($e = 0$, ω undefined) with inclination $i = 0.886$ rad = 50.8° and longitude of ascending node $\Omega = 0$. We set $t_0 = 0$, and simulated 40 measurements taken over 40 days (1 day between each epoch), with astrometric precision of $\sigma_{\delta\theta} = 5.6 \times 10^{-11}$ rad along a random axis in $(x/D_s, y/D_s)$ space, and radial velocity precision of $\sigma_{\dot{z}_i} = 1$ km/s, both per epoch. This astrometric precision is in line with the expectation for this binary for EPIC Phase I, and the spectroscopic precision to that of refs. [131, 132]. We show mock data for these truth parameters in figure 13.

In figure 14, we show the results of a MCMC parameter estimation of $\{a, i, \Omega, M_a, M_b, D_s\}$ based on the mock data from figure 13. For this system, the “astrometric angles” such as a/D_s , i , and Ω can be determined at 10^{-3} rad level of precision, whereas the dimensionful quantities M_i , a , and D_s separately are slightly less tightly constrained (but still at a precision of about 0.5% or better fractionally) due to the limited spectroscopic precision. Nevertheless, it is clear that even with these conservative assumptions, binary mass and distance measurements

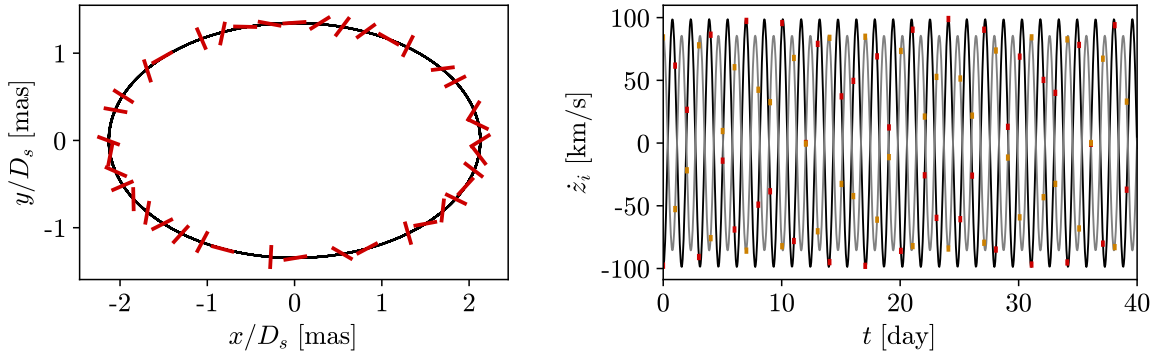


Figure 13: Mock data (red/orange points with error bars) for astrometric (left panel) and spectroscopic (right panel) measurements of the doubly-degenerate binary WD0135-052A/B. The EPIC Phase I astrometric uncertainties $\sigma_{\delta\theta} = 5.6 \times 10^{-11}$ rad are magnified by a factor of 10 for clarity.

should be possible at unprecedented precision. For example, observations of WD0135-052A/B (or other similar nearby systems [133]) with results as depicted in figure 14 would yield valuable constraints on the mass-radius relation of white dwarfs [134–136], as the same intensity interferometry observations would also yield both of the white dwarfs’ radii. With EPIC Phase II, differential astrometric precision of about $\sigma_{\delta\theta} \approx 5.6 \times 10^{-12}$ rad should be possible (cfr. figure 8), while the spectroscopic precision of $\sigma_{z_i} \sim 10$ m/s should be possible with dedicated observations by modern instruments such as ESPRESSO at the VLT [137]. A similar observation run with such capabilities should be able to characterize all orbital parameters at a fractional precision of 10^{-4} .

This type of analysis can give even more striking results on very bright stars. For example, the spectroscopic binary γ^2 Velorum, comprising a O-type blue supergiant and a Wolf-Rayet (WR) star at $D_s = 379 \pm 4$ pc. An astrometric precision per epoch of $\sigma_{\delta\theta} \sim 10^{-13}$ rad should already be achievable with EPIC Phase I, and radial velocity precision of $\sigma_{z_i} \sim 20$ m/s per epoch should also be possible on such a bright binary, yielding component masses with a fractional precision at or below the 10^{-4} level. At that level (or better), one could conceivably start to measure the mass loss rate of the WR star at $10^{-4} M_\odot/\text{yr}$, and obtain even more precise line-of-sight distance and semi-major axis. These “spectro-geometric” distance determinations on binaries involving red giants and/or Cepheid variables may also help calibrate the cosmic distance ladder independently, though not to very large line-of-sight distances.

4.2 Exoplanets

In the previous section, we have seen that EPIC can be a powerful tool for characterizing binary orbits, or orbits of more complicated triple/quadruple systems, comprising *visible* constituents. However, as long as there are two visible sources—either a visible binary or a double star from an accidental chance alignment—one can search for anomalous astrometric deviations due to invisible dark companions. This includes exoplanet searches, as outlined in [1]. Depending on the eccentricity and inclination of the exoplanet orbit, the gravitational attraction from the exoplanet will introduce an additional astrometric wobble on its host star, which will trace out an ellipse projected onto the celestial sphere (on top its unperturbed

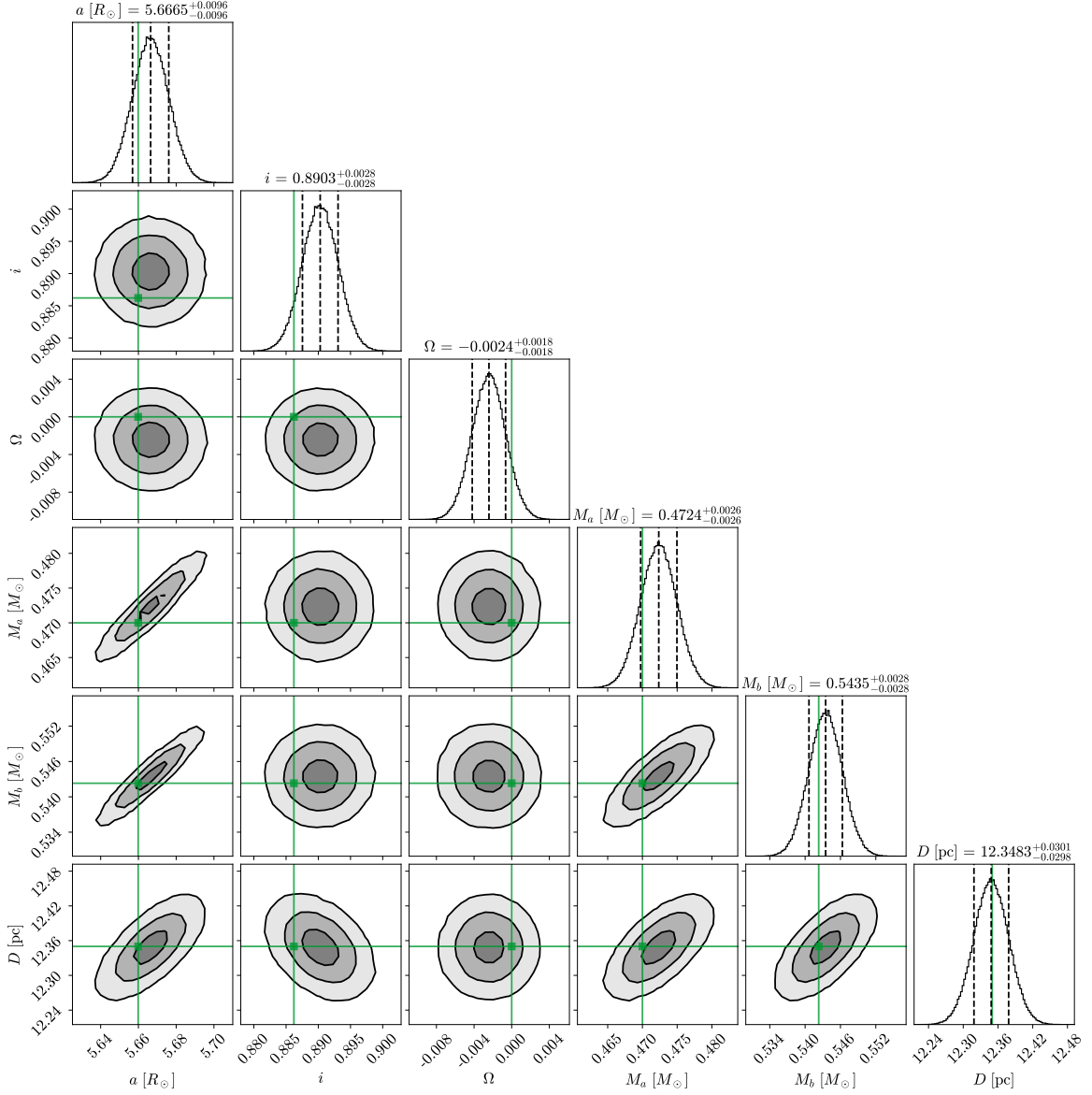


Figure 14: MCMC posteriors on the parameters $\{a, i, \Omega, M_a, M_b, D_s\}$ for a (restricted) binary orbit of WD0135-052A/B, based on the mock data of figure 13. The truth parameters are indicated by green lines (and squares). The contours are $n = 1, 2, 3$ sigma contours (levels $1 - e^{-n^2/2}$) for the 2D slices, and the vertical black dashed lines indicate the 16%, 50%, and 84% quantiles (also quoted numerically in the titles) in the 1D histograms.

motion). For the special (but most motivated) case of a circular orbit with mass M_p , semi-major axis a_p , inclination i_p , period P_p , and reference epoch t_0 , the magnitude of the host star’s astrometric wobble is:

$$\Delta\theta_a \simeq \frac{M_p}{M_a} \frac{a_p}{D_a} \sqrt{1 - \sin^2 i_p \sin^2 \left(2\pi \frac{t - t_0}{P_p} \right)}. \quad (4.5)$$

The host star’s mass is M_a and its line-of-sight distance D_a .

The method of looking for anomalous astrometric deviations of stellar light centroids has not been the most prolific exoplanet discovery technique historically, but the *Gaia* satellite has already found dozens of candidates in early data releases [5], and is expected to find thousands [138] of high-mass planets, preferentially at large semimajor axis a_p around nearby stars, due to the scalings of eq. 4.5. In figure 15, we plot the expected sensitivity of *Gaia* at its fifth data release (DR5) containing ten years of observations, for a Sun-like star at $D_a = 20$ pc in dashed blue. The sensitivity contour corresponds to a final-mission sensitivity of $\sigma_{\Delta\theta_a} \approx 7 \mu\text{as}$, and a $3\text{-}\sigma$ detection threshold, for orbits shorter than the mission duration, i.e. $a_p \lesssim 4.6$ AU.

An EPIC setup can surpass this sensitivity by a couple of orders of magnitude for nearby stars, or alternatively, extend the volume over which the technique is applicable. For a pair of Sun-like stars at $D_a = 20$ pc, the per-epoch light centroiding precision is $\sigma_{\delta\theta} \approx \{4.5, 0.29, 0.011\} \mu\text{as}$ for EPIC Phases {I, II, III}. With $N_{\text{obs}} = 300$ observations (e.g. a cadence of about one per month over 30 years), the final wobble sensitivity is of order $\sigma_{\Delta\theta_a} \approx \{0.26, 0.017, 0.00065\} \mu\text{as}$, indeed better than *Gaia* by a large factor for this particular application (for nearby stars, with a companion in close proximity). We show contours of $3\text{-}\sigma$ sensitivity as blue regions in figure 15 for $D_a = 20$ pc. Earth-Sun-like systems ($M_a = M_\odot$, $M_p = M_\oplus$, and $a_p = 1$ AU) should be observable by EPIC Phase II at distances of $D_a \lesssim 20$ pc ($D_a \lesssim 400$ pc by Phase III), as long as a sufficiently bright reference star is nearby.

The exoplanet parameter space accessible to an EPIC is complementary to that of other methods. Exoplanet transits causing repeating, temporary dips in the host star’s brightness have been detected from the ground [141, 142] and especially with the *Kepler* satellite [143], which has produced the largest exoplanet catalog to date; the approximate parameter space is depicted by purple lines in figure 15. These surveys have a moderate bias toward small semimajor axes due to the higher transit frequency. Likewise, many exoplanets are detected via the radial velocity (RV) they impart on their host star [144], but this method also favors small semimajor axes, as the radial velocity scales as $\dot{z}_a \sim \sqrt{GM_p^2/M_a a_p}$. We plot the RV detection sensitivity for precisions of 3 m s^{-1} in solid orange, and 0.3 m s^{-1} in dashed orange. Direct imaging also favors large planets far away from their host star (red) [145]. Finally, chance alignments of exoplanetary systems with background stars can lead to detection of even very low-mass systems; the approximate sensitivity with ground-based observations is depicted in solid green, and with space-based observations (e.g. *Nancy Grace Roman Space Telescope*) in dashed green, following ref. [146].

4.3 Accelerations

The exquisite astrometric light-centroiding of EPIC enables precise measurements of the relative transverse angular accelerations between two stars, and thus of the difference in their gravitational potential gradient (or at least two components thereof). This is a *direct, local*

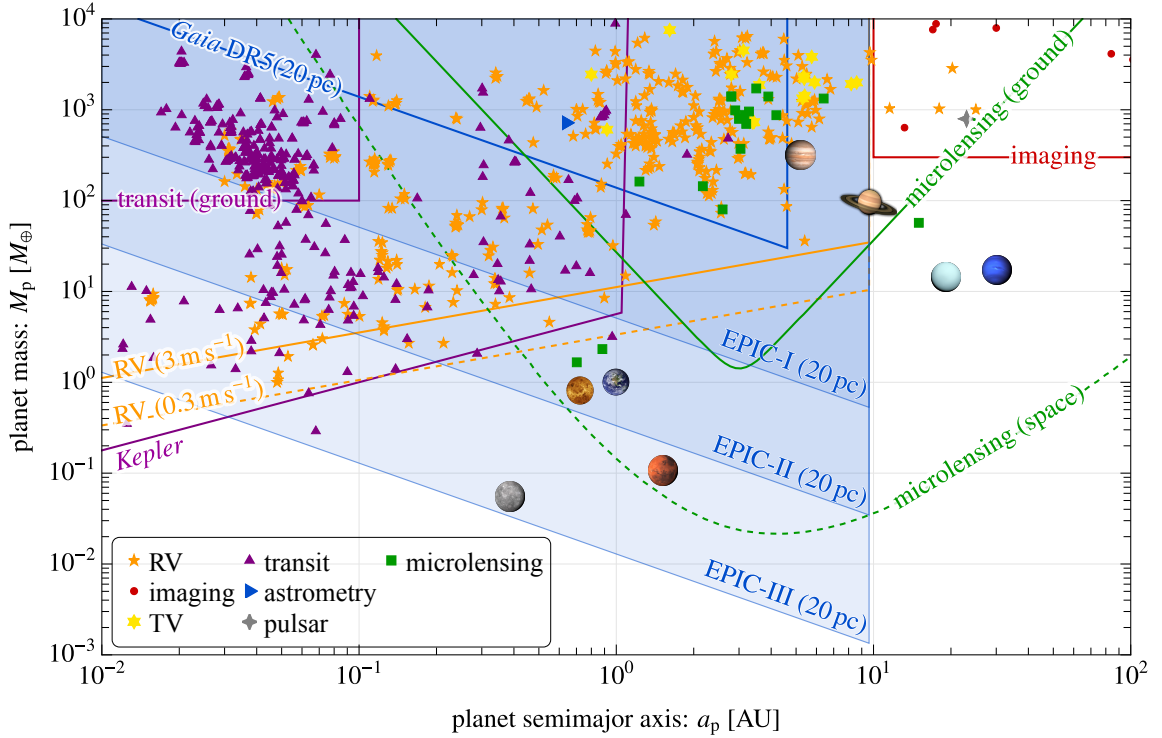


Figure 15: Sensitivity of exoplanet detection techniques as a function of semimajor axis a_p and mass M_p . The astrometric $3\text{-}\sigma$ detection sensitivity of EPIC Phases I-III is shown by the blue regions for a Sun-like star at $D = 20$ pc. The markers depict confirmed exoplanets in multiple-star systems (those where EPIC is definitely applicable), classified by discovery method from the NASA Exoplanet Archive [139, acquired May 2023]. The astrometric sensitivity of *Gaia* DR5 is outlined by the dashed blue line, that of radial velocity (RV) surveys by the orange lines, transit methods by the purple lines, direct imaging by the red line, and microlensing by the green lines (adapted from ref. [140]). The eight Solar System planets and planets discovered eclipse timing variations (TV) are also overlaid (image credit: NASA). Figure from companion paper [1].

probe of the gravitational potential and the underlying matter distribution, unlike techniques based on the MW’s rotation curve [147] (not local, since they are based on the enclosed mass within the orbit) or on velocity dispersions [148–152] (not direct, since they rely on assumptions of equilibrium and symmetry, which are furthermore violated [153–155]).

The line-of-sight component of the MW acceleration (relative to that of the Solar barycenter) can be measured by next-generation spectrographs through the resulting changes in radial velocity [156–158] and by pulsar timing arrays through changes in the pulsar’s spin period [159] or in the orbital period of pulsar binaries [159–161]. The latter orbital period drift is already constraining the vertical acceleration towards the Galactic disk at moderate signal-to-noise ratio, with further improvements expected over time. Ref. [15] has proposed using *Gaia* and future astrometric observatories (potentially in tandem) to measure the transverse angular acceleration of MW stars, forecasting that *Gaia* alone should have significant evidence for the MW’s transverse angular acceleration by the end of its mission, if large-angle systematics can be kept under control.

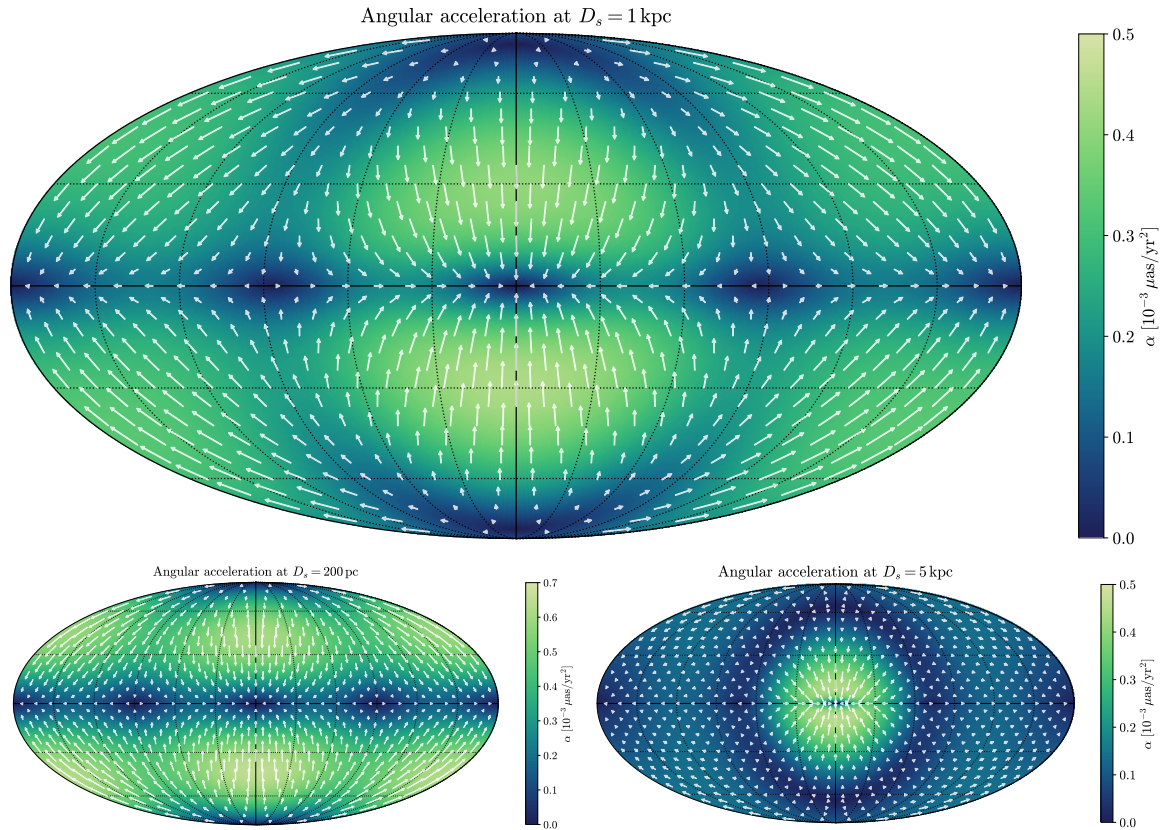


Figure 16: Apparent angular acceleration vector field in the Milky Way in galactic coordinates at three line-of-sight distances $D_s = 1$ kpc (top), $D_s = 200$ pc (bottom left), and $D_s = 5$ kpc (bottom right). The angular accelerations towards the Galactic disk are dominant (but no larger than $10^{-3} \mu\text{as yr}^{-2}$, as indicated by the color bars) for small distances, while for $D_s \gtrsim 1$ kpc the bulge and DM halo also give important contributions. The nodes at $(l, b) \approx \{(0^\circ, 0^\circ), (90^\circ, 0^\circ), (180^\circ, 0^\circ), (270^\circ, 0^\circ), (0^\circ, 90^\circ), (0^\circ, -90^\circ)\}$ for small D_s are dictated by symmetry.

In this section, we revisit the idea from ref. [15] and show that EPIC can significantly surpass the sensitivity of *Gaia* by a large factor, albeit on a much smaller number of stars due to its limitations on apparent brightness. For a *single* pair of stars, it may approach a (relative) angular acceleration sensitivity of $\sigma_{\delta\alpha} \sim 10^{-3} \mu\text{as yr}^{-2}$ over a 30-year observing campaign, close to the expected size of Galactic accelerations.

To estimate the size of the Galactic accelerations, we follow ref. [15] and use a simple model of the MW matter components, which is a combination of a bulge, disk, and spherical DM halo. We use the the Hernquist bulge model [162] with total mass $M_{\text{bulge}} = 5 \times 10^9 M_\odot$ and scale radius $r_{\text{bulge}} = 0.6$ kpc, a Miyamoto-Nagai disk model [163] with mass $M_{\text{disk}} = 6.8 \times 10^{10} M_\odot$, scale length $a_{\text{disk}} = 3$ kpc, and scale height $b_{\text{disk}} = 280$ pc, and the Navarro-Frenk-White (NFW) profile [164] for the DM halo with scale radius $r_s = 16$ kpc and local density (at $r_\odot = 8$ kpc from the Galactic Center) of $\rho_\odot = 0.3 \text{ GeV/cm}^3 = 0.008 M_\odot/\text{pc}^3$. Within this model, it is then straightforward to calculate the gravitational potential Φ and the resulting acceleration $\mathbf{a}(\mathbf{r}) = -\nabla\Phi$ at any position \mathbf{r} in the MW. The apparent angular

acceleration is then given by

$$\boldsymbol{\alpha}(l, b, D_s) = \frac{\delta a}{D_s} \left[\hat{\boldsymbol{\delta}}\mathbf{a} - \hat{\mathbf{D}}_s(\hat{\mathbf{D}}_s \cdot \hat{\boldsymbol{\delta}}\mathbf{a}) \right], \quad (4.6)$$

in terms of the acceleration relative to that of the solar barycenter $\boldsymbol{\delta}\mathbf{a} \equiv \mathbf{a}(\mathbf{r}) - \mathbf{a}(\mathbf{r}_\odot)$, the distance vector $\mathbf{D}_s \equiv \mathbf{r} - \mathbf{r}_\odot$ to the star, and their unit vectors $\hat{\boldsymbol{\delta}}\mathbf{a}$ and $\hat{\mathbf{D}}_s$, respectively. We plot the fiducial angular acceleration of eq. 4.6 as a function of galactic longitude l and latitude b in figure 16, for three distances $D_s = \{200 \text{ pc}, 1 \text{ kpc}, 5 \text{ kpc}\}$. Typical Galactic acceleration magnitudes are at the level of $0.3 \times 10^{-3} \mu\text{as yr}^{-2}$.

An EPIC telescope can track the relative angular separation $\boldsymbol{\theta}_{ba}$ between two sources a and b , and thus the relative angular acceleration between two sources $\boldsymbol{\alpha}_{ba} \equiv \boldsymbol{\alpha}_b - \boldsymbol{\alpha}_a$ according to eq. 4.6. In practice, both of the components of $\boldsymbol{\theta}_{ba}$ would be fit to the model:

$$\theta_{ba}^j(t) \simeq \varpi_0^j \cos\left(2\pi \frac{t}{\text{yr}} + \gamma^j\right) + \theta_0^j + \mu_0^j(t - t_0) + \alpha_0^j \frac{(t - t_0)^2}{2}. \quad (4.7)$$

where $j = 1, 2$ is a component superscript (e.g. (ra, dec)), and ϖ_0^j , θ_0^j , μ_0^j , and α_0^j are the fit parameters for the relative parallax, angular position, velocity, and acceleration, respectively. The phases γ^j are known based on the position of the source. Assuming measurements are taken at a fixed repetition frequency f_{rep} over a survey time \mathcal{T} (so a total number of measurement epochs $f_{\text{rep}}\mathcal{T}$), the covariance matrix on the estimated fit parameters for one component p from a least-squares analysis would then be:

$$\text{cov} \left[\hat{\theta}_i, \hat{\theta}_j \right] = \frac{\sigma_{\delta\theta}^2}{f_{\text{rep}}} \begin{pmatrix} \frac{2}{\mathcal{T}} & \frac{15}{\pi^2 \mathcal{T}^3} & 0 & \frac{-360}{\pi^2 \mathcal{T}^5} \\ \frac{15}{\pi^2 \mathcal{T}^3} & \frac{9}{4\mathcal{T}} & 0 & \frac{-30}{\mathcal{T}^3} \\ 0 & 0 & \frac{12}{\mathcal{T}^3} & 0 \\ \frac{-360}{\pi^2 \mathcal{T}^5} & \frac{-30}{\mathcal{T}^3} & 0 & \frac{720}{\mathcal{T}^5} \end{pmatrix}; \quad \hat{\theta}_i = \left\{ \hat{\varpi}_0^j, \hat{\theta}_0^j, \hat{\mu}_0^j, \hat{\alpha}_0^j \right\}, \quad (4.8)$$

where $\sigma_{\delta\theta}$ is the single-epoch light-centroiding precision of eq. 2.50 as before.

The Galactic acceleration is prohibitively small to be measured by EPIC Phase I, and difficult to detect on single star pairs even for EPIC Phase II, though perhaps positive evidence for the effect can be obtained on aggregate. EPIC Phase III, however, could map out the Galactic acceleration field on single star pairs. Its relative light-centroiding precision for two Sun-like stars at a distance of 200 pc would be $\sigma_{\delta\theta} \approx 0.11 \mu\text{as}$, and the resulting error on the relative acceleration would be $\sigma_{\delta\alpha} \simeq \sqrt{720/f_{\text{rep}}\mathcal{T}^5} \sigma_{\delta\theta} \approx 0.18 \times 10^{-3} \mu\text{as yr}^{-2}$ for $f_{\text{rep}} = 1/\text{month}$ and $\mathcal{T} = 30 \text{ yr}$, smaller or comparable to the expected accelerations of stars in the Milky Way shown in figure 16. Brighter stars would yield higher accuracy and sensitivity to accelerations at larger distances.

We leave a detailed projection on how a EPIC could be used to infer the structure of the Milky Way (e.g. as done in ref. [15]) to future work. Such an analysis would entail finding suitable bright source pairs, where the two constituents of the pair would have significantly different line-of-sight distances, otherwise their predicted relative accelerations would be too similar, with little signal remaining in their relative angular accelerations. An ideal configuration would consist of bright nearby stars close to distant sources, such as red/blue giants or quasars.

4.4 Stellar microlensing

Gravitational microlensing is the phenomenon whereby a compact foreground object, either luminous (e.g. a star) or dark (e.g. a black hole, neutron star, or compact dark matter object), temporarily passes nearly in front of a background source, bending its light and splitting its image into two (often unresolved) images [165]. Such an event produces transient signals in both photometric and astrometric observables [165–168]. Due to experimental realities, the photometric signal—a characteristic non-repeating magnification event in the light curve of a background source—has historically been the primary driver in the search for compact lenses [169–171], even excluding primordial black holes as the totality of dark matter over a wide mass range. Ground-based microlensing surveys such as Optical Gravitational Lensing Experiment (OGLE) [172], Microlensing Observations in Astrophysics (MOA) [173], and the Korea Microlensing Telescope Network (KMTNet) [174] continue to detect thousands of photometric microlensing events every year in dense stellar fields, and will soon be joined by a similar survey [146] with the *Nancy Grace Roman Space Telescope* [175]. Astrometric microlensing has been observationally challenging [176–178] but has recently become a useful tool, yielding positive stellar microlensing detections [179, 180], confirming the discovery of the first isolated black hole [3, 4, 181, 182], and spurring forecasts for astrometry-only analyses of luminous lenses [183] and “blind” searches for dark compact lenses [14, 184].

Since the optical depth for Galactic microlensing is tiny and building a vast catalog with EPIC is infeasible, blind searches for dark compact lenses with EPIC are not practical. However, EPIC’s excellent astrometric capabilities enable precise parameter estimation of two classes of microlensing events. Firstly, weak microlensing events between two luminous sources as predicted by e.g. *Gaia* may pinpoint the lens mass along the lines of ref. [183] but with higher precision. Secondly, for photometrically-flagged strong microlensing events of dark compact lenses, the relative separation of the two source images can be measured (as proposed in ref. [185]) by EPIC, again with great potential for parameter estimation. In this section, we will explore EPIC’s potential for these two use cases.

The characteristic angular scale of a microlensing event by a point-like lens of mass M_L at a line-of-sight distance D_L of a source at distance D_S is set by the (angular) Einstein radius:

$$\theta_E = \sqrt{\frac{4GM_L}{c^2 D_L} \frac{D_S - D_L}{D_S}} \approx 2.85 \text{ mas} \sqrt{\frac{M_L}{M_\odot} \frac{1 \text{ kpc}}{D_L} \frac{D_S - D_L}{D_S}}. \quad (4.9)$$

At an angular impact parameter β from the lens to the (unlensed) source location, the source image is split into two (denoted by + and – subscripts), with astrometric deflection angles $\Delta\theta_\pm$ and photometric magnifications μ_\pm :

$$\Delta\theta_\pm = \frac{\pm\sqrt{\beta^2 + 4\theta_E^2} - \beta}{2} \hat{\beta}; \quad (4.10)$$

$$\mu_\pm = \frac{\beta^2 + 2\theta_E^2}{2\beta\sqrt{\beta^2 + 4\theta_E^2}} \pm \frac{1}{2}; \quad (4.11)$$

$$\beta^j \equiv \left(\hat{\theta}_S - \hat{\theta}_L\right)_{\text{unlensed}}^j \equiv \varpi_0^j \cos\left(2\pi\frac{t}{\text{yr}} + \gamma^j\right) + \theta_0^j + \mu_0^j(t - t_0). \quad (4.12)$$

On the RHS of the last line, we have parametrized the unlensed trajectory by 5 parameters: the relative parallax ϖ_0 (whose direction and phases γ_j are known), and the relative separation

θ_0 and proper motion μ_0 (two components each, not to be confused with the magnifications μ_{\pm}) at some reference time t_0 (taken to be the midpoint of the observation period).

In this notation, the two aforementioned signatures for EPIC are as follows. Analogous to the *Gaia* forecasts of ref. [183], EPIC can measure the relative separation of a luminous lens and (the primary “+” image of) a source

$$\theta_{\text{SL}} \equiv \hat{\theta}_{\text{S}+} - \hat{\theta}_{\text{L}} = \beta + \Delta\theta_+ \quad (\text{weak lensing, luminous lens}). \quad (4.13)$$

Likewise, EPIC can also be employed to execute the proposal from ref. [185] to measure the relative separation θ_{+-} between the two images of the source in a microlensing event by a non-luminous lens:

$$\theta_{+-} \equiv \hat{\theta}_{\text{S}+} - \hat{\theta}_{\text{S}-} = \sqrt{\beta^2 + 4\theta_{\text{E}}^2} \hat{\beta} \quad (\text{strong lensing, dark lens}). \quad (4.14)$$

The observables in eqs. 4.13 and 4.14 can both be fit by 6 parameters: the 5 parameters in eq. 4.12, and the lens mass M_{L} , using the well-known fact that one can write $\theta_{\text{E}}^2 = 4GM_{\text{L}}\varpi_0/\text{AU}$ in terms of the lens mass M_{L} and the relative parallax ϖ_0 . In both cases, the lens mass can be extracted directly, unlike in photometry-only microlensing measurements with only the total magnification $\mu_+ + \mu_-$ as an observable.

To assess EPIC’s astrometric microlensing capabilities, we generate two mock data sets. The first is for the weak microlensing event 4410342766254199168-35742 between two luminous stars predicted from *Gaia* data in ref. [186]. We assume “truth values” for the system of $\{-46.1 \text{ mas}, 45.8 \text{ mas}, 108.04 \text{ mas/yr}, -118.78 \text{ mas/yr}, 11.4 \text{ mas}, 1.3 M_{\odot}\}$ for $\{\theta_0^{\alpha}, \theta_0^{\delta}, \mu_0^{\alpha*}, \mu_0^{\delta}, \varpi_0, M_{\text{L}}\}$, the two components each (right ascension α and declination δ , with $\mu_0^{\alpha*} \equiv \mu_0^{\alpha} \cos \delta$) of relative separation θ_0 and proper motion μ_0 , and for the relative parallax ϖ_0 and lens mass M_{L} . We set the parallax phases γ_j to zero and $3\pi/2$ for the right ascension and declination components, respectively. We generate a mock data set according to eq. 4.13 comprised of six relative angular separation measurements, spanning a period of a year around the closest approach. We assume an astrometric light-centroiding precision of $\sigma_{\delta\theta} = 11 \mu\text{as}$ per epoch, which is the expectation per observing night given the quoted apparent magnitude of the two stars in ref. [186] and Phase II instrumental parameters of an EPIC interferometer. We perform an MCMC parameter estimation of $\{\theta_0^{\alpha}, \theta_0^{\delta}, \mu_0^{\alpha*}, \mu_0^{\delta}, \varpi_0, M_{\text{L}}\}$, whose posteriors we show in figure 17.

The second mock data set is for the black-hole microlensing event MOA-2011-BLG-191/OGLE-2011-BLG-0462 from refs. [3, 4, 181, 182]. We create a (counterfactual) simulation of the dark lens’ mass estimation had EPIC taken data around the time that OGLE detected the photometric amplification. For our mock data generation, we assume a relative separation of $\{\theta_0^{\alpha}, \theta_0^{\delta}\} = \{-0.23, -0.17\}$ mas at the time of closest (unlensed) approach (taken to be the reference epoch t_0), commensurate with the reported closest approach of $\min \beta \approx 0.05 \theta_{\text{E}}$ and Einstein angle $\theta_{\text{E}} \approx 5.81 \text{ mas}$ from ref. [182]. We take the mean values of their inferred velocities as our “truth parameters”, namely $\{\mu_{\text{L}}^{\alpha*}, \mu_{\text{L}}^{\delta}\} = \{4.36, 3.06\} \text{ mas/yr}$ and $\{\mu_{\text{S}}^{\alpha*}, \mu_{\text{S}}^{\delta}\} = \{2.263, -3.597\} \text{ mas/yr}$, with the relative proper motion $\mu_0 \equiv \mu_{\text{S}} - \mu_{\text{L}}$. Likewise, we take the mass of the dark lens to be $M_{\text{L}} = 7.1 M_{\odot}$ and a relative parallax magnitude of $\varpi_0 = 0.6 \text{ mas}$. We also do not study the effects of the unequal brightness of the two images, nor their lensing-induced elongation (primarily along the axis perpendicular to $\hat{\theta}_{+-}$), which could slightly affect the form factor.

Given the faintness of this particular source star, whose I-band magnitude varies in the range $13 \lesssim m_{\text{I}} \lesssim 16$ during the microlensing event, Phase II of EPIC would yield a low

SNR, so Phase III parameters might be needed for high significance. On the other hand, the source is far enough that larger baselines can be employed: a Sun at the 1.5 kpc distance to the lens, would have an optimal baseline of 4 km baseline, yielding an angular resolution of $\sigma_{\theta_{\text{res}}} \approx 6 \mu\text{as}$ in the I band, and even better light centroiding. Assuming a conservative light-centroiding precision of $\sigma_{\delta\theta} \simeq \sigma_{\theta_{\text{res}}}$, we generate a mock data set which comprises six relative-angle measurements between the two images of the source, according to eq. 4.14, interspersed within two years around the closest approach. We perform an MCMC parameter estimation of $\{\theta_0^\alpha, \theta_0^\delta, \mu_0^{\alpha*}, \mu_0^\delta, \varpi_0, M_L\}$, whose posteriors we show in figure 18.

The capability of *Gaia* in determining stellar masses from star-star microlensing is projected to be at best a few percent: according to ref. [183], the mission can achieve stellar mass determination of about 5 to 10% for about seven events and below 15% for thirteen events total. As seen from the marginalized posterior for the lens mass in figure 17, even with the conservative assumptions of a Phase II interferometer and just six observing epochs, EPIC can greatly surpass *Gaia*'s capability per microlensing event by at least an order of magnitude, thereby achieving a 0.46% determination of the lens mass.

The microlensing event MOA-2011-BLG-191/OGLE-2011-BLG-0462 from an isolated black hole yielded a determination of the dark lens' mass to about 18% using *HST* astrometry [3, 4, 181, 182]. The observable in this case was the luminosity-weighted light centroid separation of *both* images of the source star, since *HST* cannot resolve them from each other. In contrast, an EPIC interferometer, much like the proposal of ref. [185] to use the VLT, can directly resolve the angular separation of the two images, thereby allowing for an order of magnitude better measurement of the dark lens' mass, down to a precision level of 1.7% with Phase II specifications, as seen from figure 18. Phase III could improve the significance and light centroiding by more than an order of magnitude, far surpassing the capabilities of optical interferometers, whose baselines can be at most a few hundred meters and light-centroiding precision of about $10 \mu\text{as}$ [185]. It would be interesting to pursue a more detailed analysis of dark lens microlensing events, including the modification of the stellar sizes due to elongation, which could give a form factor suppression akin to that of eq. 2.34 if resolved, but could also provide information about the lens structure.

4.5 Strongly lensed quasars

Intensity interferometry, including the extended-path variation detailed in this work, is only feasible on compact sources with a high surface brightness. The most obvious sources *at cosmological distances* are quasars, extremely luminous emission regions powered by the accretion of matter onto a supermassive black hole. (Other potential targets at large distances include dense stellar clusters and supernovae, but intensity interferometry applications for these sources are left to future work.) Their overall apparent brightness is not too small for advanced Phases of EPIC. The morphology of quasar emission regions is not well understood, and only an intensity interferometer may have the requisite effective angular resolution to directly resolve the nano-arcsecond structure of quasar central engines. Complementary indirect methods have also been proposed [187].

About 1 in 500 quasars are known to be strongly lensed into two or more images [188]. These images are often magnified by about an order of magnitude in apparent brightness, and are typically separated by about an arcsecond. (Smaller image separations are also possible but are not easily resolved, so some “single quasars” may actually consist of two or more duplicate images.) The first such system was Q0957 + 561 [189], while the most striking and best-studied system is Q2237 + 0305 [190, 191]. A few hundred multiply-imaged quasars are

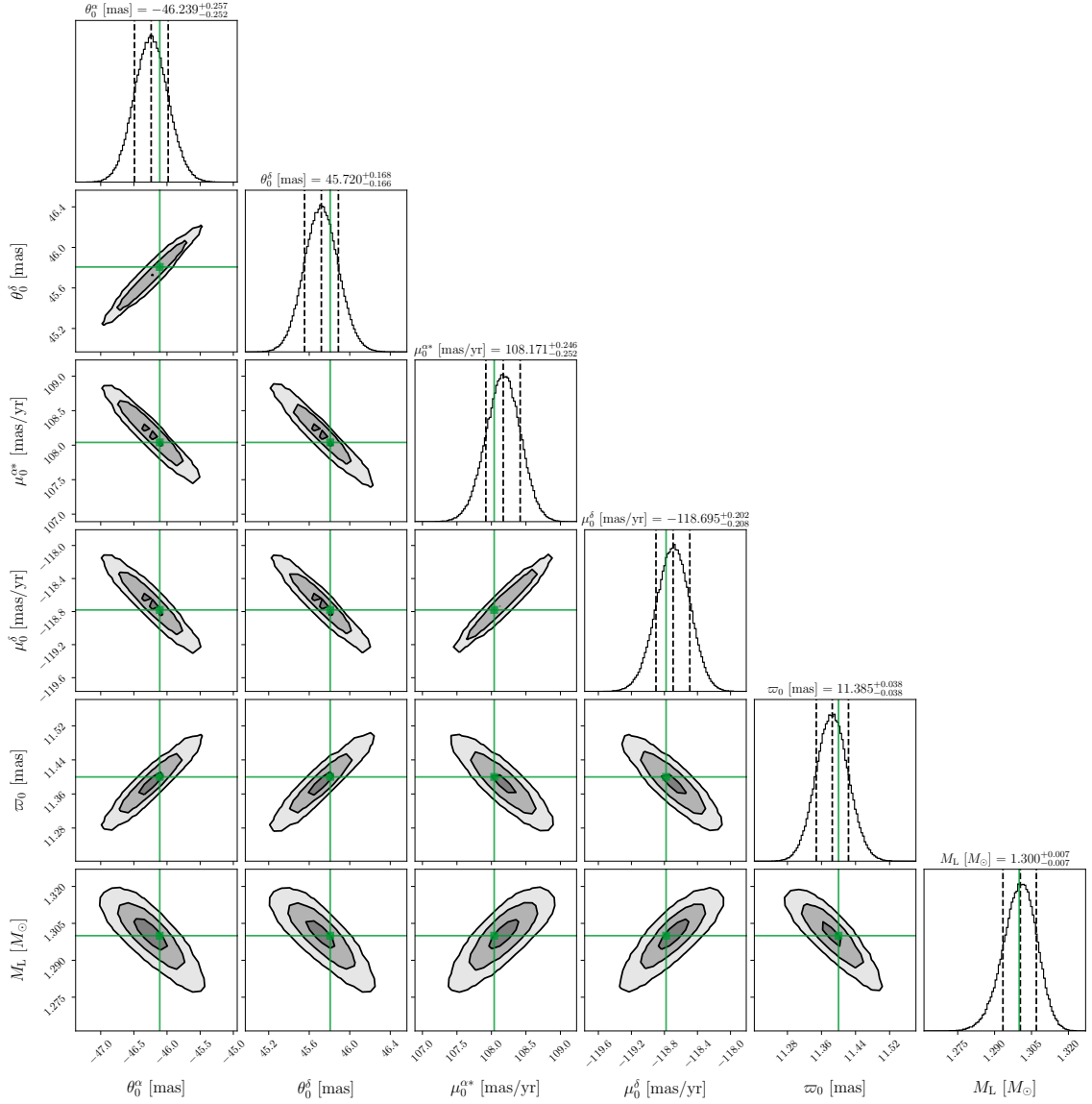


Figure 17: MCMC posteriors of the full relative astrometric solution $\{\theta_0^\alpha, \theta_0^\delta, \mu_0^{\alpha*}, \mu_0^\delta, \varpi_0, M_L\}$ from a mock data set of six relative separation measurements of the microlensing event 4410342766254199168-35742 predicted in ref. [186]. The measurements span a period of one year around the time of closest approach of the two stars, each having a precision $\sigma_\theta = 11 \mu\text{as}$. Remarkably, EPIC Phase II can determine the mass of the stellar lens at the 0.46% level, even with just enough measurements to break the parameter degeneracy.

known at present [192, 193], with an explosion of this sample (approaching 10^4) expected from upcoming surveys [194], most notably LSST but also the Dark Energy Survey, DESI, and Euclid.

EPIC is ideally suited to perform relative astrometry on any pair of strongly-lensed quasar images. The relative locations of these images are not so interesting per se, but with

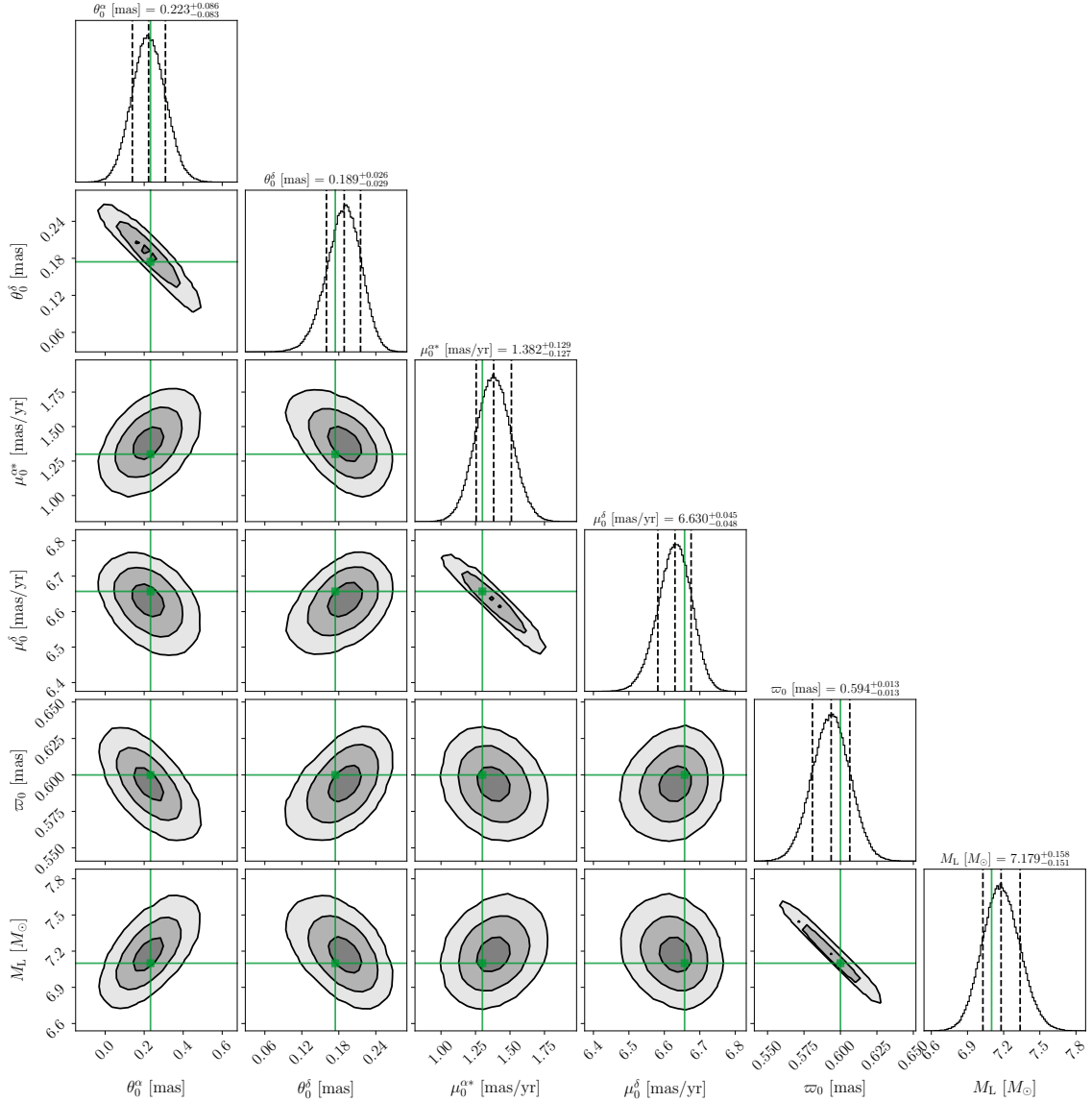


Figure 18: MCMC posteriors of the full relative astrometric solution $\{\theta_0^\alpha, \theta_0^\delta, \mu_0^{\alpha*}, \mu_0^\delta, \varpi_0, M_L\}$ from a mock data set of six relative separation measurements of the two images of MOA-2011-BLG-191/OGLE-2011-BLG-0462 [3, 4, 181, 182]. The measurements span a period of two years around the time of closest approach of the star to the dark lens, each having a precision $\sigma_\theta = 6 \mu\text{as}$ assuming Phase II instrumental parameters. The achieved determination of the mass of the dark lens—in this case an isolated black hole—is at the 1.7% level.

its exquisite light-centroiding precision, EPIC can track *changes* in their relative separation. Such changes can occur due to the (relative) peculiar velocities of the quasar-lens system, which lead to differential proper motion between the various quasar images because of the relative distortions caused by the lensing potential. The apparent image proper motions also sweep through the fine-grained structure of the gravitational potential, most notably the

micro-caustic network of stars in the lens galaxy. Near any micro-caustic crossing, one expects (correlated) photometric [191, 195–198] and astrometric [188, 199, 200] variability. A companion paper [128] to this work fleshes out an entirely new signature—stochastic astrometric weak lensing fluctuations from low-mass dark matter halos.

In this work, we will content ourselves with making rough projections on the relative astrometric light-centroiding precision between two images, and how this information can be used to measure the effective proper motion and macro-lensing Jacobians. These measurements would allow, for the first time, highly significant determinations of transverse proper motions of objects at cosmological distances and strong-lensing geometries for multiply-imaged quasars in their respective rest frames. The lensing map from an image-plane location $\boldsymbol{\theta}$ to a source-plane location $\boldsymbol{\beta}$ is given by the lensing map $\boldsymbol{\varphi}$,

$$\boldsymbol{\beta} = \boldsymbol{\varphi}(\boldsymbol{\theta}) = \boldsymbol{\theta} - \boldsymbol{\alpha}(\boldsymbol{\theta}), \quad (4.15)$$

with $\boldsymbol{\alpha}(\boldsymbol{\theta})$ the well-known (reduced) deflection angle, which can be written as:

$$\boldsymbol{\alpha}(\boldsymbol{\theta}) = 2 \int_0^{D_q} dD' \frac{D_q - D'}{D_q} \nabla_{\perp} \Phi(D'\boldsymbol{\theta}, D'). \quad (4.16)$$

In the above, D_q is the angular diameter distance to the quasar, and Φ is the 3D gravitational potential, which in almost all cases of relevance is dominated by the lens galaxy at some distance D_L . The macro-lensing Jacobian is the determinant of the lensing map, and is given by:

$$A_{ij} \equiv \frac{\partial \beta_i}{\partial \theta_j}. \quad (4.17)$$

Let B be the inverse of the 2×2 matrix A , i.e. $B_{ij} = (A^{-1})_{ij}$, which is a function of $\boldsymbol{\theta}$. The total image magnification is given by $\det B$. The inverse map $\boldsymbol{\varphi}^{-1} : \boldsymbol{\beta} \rightarrow \boldsymbol{\theta}$ is, in general, multi-valued (leading to multiple images). Let us denote the multiple quasar image locations as $\boldsymbol{\theta}^I = \boldsymbol{\varphi}^{-1}(\boldsymbol{\beta}_q)|_I$ with $I = A, B, \dots$ a discrete label for the images, and $\boldsymbol{\beta}_q$ the quasar's location on the source plane.

The effective apparent angular motion between the quasar and the lens galaxy (in the source plane) is

$$\boldsymbol{\mu} \equiv \frac{d\boldsymbol{\beta}}{dt} = \frac{\mathbf{v}_q}{1+z_q} \frac{1}{D_q} - \frac{\mathbf{v}_L}{1+z_L} \frac{1}{D_L} + \frac{\mathbf{v}_o}{1+z_L} \frac{D_q - D_L}{D_L D_q} \quad (4.18)$$

where \mathbf{v}_q , \mathbf{v}_L , and \mathbf{v}_o are the proper velocities of the quasar, lens galaxy, and observer, respectively [201]. With these definitions, the trajectory for each of the images is:

$$\boldsymbol{\theta}_i^I(t) = \boldsymbol{\theta}_i^I(t_0) + \sum_j B_{ij}^I \left[\boldsymbol{\mu}_j(t - t_0) + \boldsymbol{\varpi}_j \cos \left(2\pi \frac{t}{\text{yr}} + \beta_j \right) \right] \quad (4.19)$$

with $B_{ij}^I \equiv B_{ij}[\boldsymbol{\theta}^I(t_0)]$. For example, for Huchra's lens at $z_L = 0.0394$ which quadruply lenses the quasar Q2237+0305, we have

$$\boldsymbol{\mu} \simeq \frac{v_L}{(1+z_L)D_L} \approx 0.252 \mu\text{as/yr} \left(\frac{v_L}{200 \text{ km/s}} \right); \quad \boldsymbol{\varpi} \simeq \frac{\text{AU}}{(1+z_L)D_L} \approx 0.0060 \mu\text{as}. \quad (4.20)$$

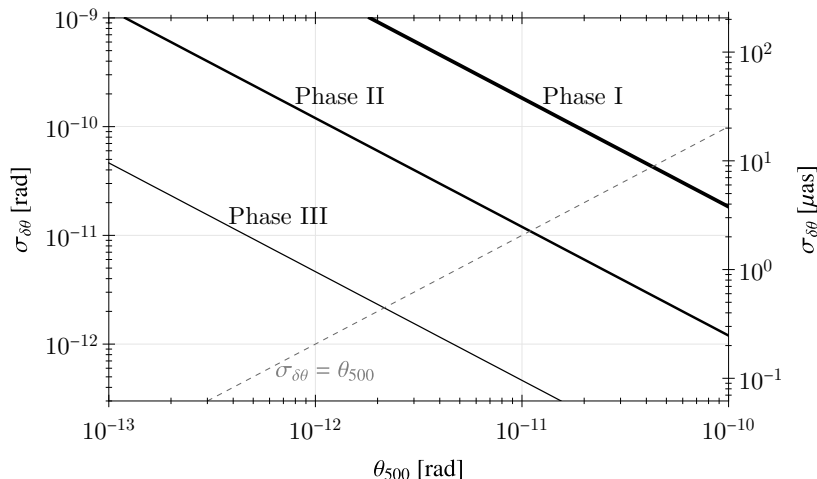


Figure 19: Light-centroiding precision $\sigma_{\delta\theta}$ from eq. 2.51 (at the optimal baseline distance d^{opt} of eq. 2.52) between two identical quasar images with apparent angular optical radius θ_{500} . For EPIC Phase III, we project that $\sigma_{\delta\theta,q}^{\text{opt}} \approx 4.64 \times 10^{-13} \text{ rad}$ ($10^{-11} \text{ rad}/\theta_{500}$) in our simple quasar emission model.

These astrometric deviations are then further magnified by the strong lens, parametrized by the (inverse) Jacobian B_{ij}^I , which can further amplify astrometric perturbations by up to a factor of 10 (or even higher [202]) along some direction(s), depending on the image and strong lens under consideration.

An error estimate analogous to the one in eq. 4.8 for this simpler model without acceleration gives uncertainties on the estimators of the parallax, relative separation, and proper motion (in each direction $j = 1, 2$) of:

$$\begin{pmatrix} \sigma_{\hat{\omega}_0^j} \\ \sigma_{\hat{\theta}_0^j} \\ \sigma_{\hat{\mu}_0^j} \end{pmatrix} = \frac{\sigma_{\delta\theta}}{\sqrt{f_{\text{rep}} \mathcal{T}}} \begin{pmatrix} \sqrt{2} \\ 1 \\ \frac{2\sqrt{3}}{\mathcal{T}} \end{pmatrix} \approx \begin{pmatrix} 0.168 \mu\text{as} \\ 0.119 \mu\text{as} \\ 0.0138 \mu\text{as/yr} \end{pmatrix} \left(\frac{\sigma_{\delta\theta}}{10^{-11} \text{ rad}} \right) \left(\frac{10/\text{yr}}{f_{\text{rep}}} \right)^{1/2} \quad (4.21)$$

with the latter estimate at $\mathcal{T} = 30 \text{ yr}$. The quoted uncertainties are for the apparent parallax and proper motion in the image plane; the magnification by the B_{ij}^I factors for each image in the pair will further reduce the uncertainties for the quantities in the source plane. We plot the expected light-centroiding precision $\sigma_{\delta\theta}$ from eq. 2.51 (at the optimal baseline distance d^{opt} of eq. 2.52) between two identical quasars in figure 19 for the three Phases of EPIC. Comparison of eqs. 4.20 and 4.21 shows that the relative motions between any image pair should be measurable at high fractional precision over a long time period with EPIC Phase II and III, while the parallax is extremely challenging to measure, even for this especially close lens.

In the simple model of eq. 4.19, we have ignored the effects of fine-grained structures in the lens galaxy, both from the stellar population and from dark matter substructures. Astrometric deflections from stellar substructure have been proposed as potentially observed signatures in ref. [188, 200] and from medium-scale dark matter subhalos in ref. [199]; these

are all interesting effects that can be explored with an intensity interferometer. A companion paper [128] will explore the astrometric noise caused by dark matter substructures at extremely small scales (substellar masses).

5 Conclusions

We have proposed the *Extended-Path Intensity Correlator* (EPIC) [1], an optical modification of intensity interferometers that introduces an adjustable, differential geometric extension in the light paths from widely-separated sources. EPIC expands the field of view of traditional intensity interferometry—by up to six orders of magnitude beyond the angular resolution—while preserving the light-centroiding precision. In detail, the EPIC setup consists of a large primary mirror and a collimating secondary mirror that guides the light into the path-extension system (figure 5). The latter has the form of a Mach-Zehnder interferometer of unequal path lengths, and serves a dual role: it introduces the geometric path extension and corrects for the relative tilt of the sources’ wavefronts. The wavefront tilt correction avoids the fringe suppression present when a constituent telescope resolves the source separation. The path extension allows for angular distances between sources at arcsecond separations to be determined with microarcsecond precision.

Our proposal arrives at a time when technological advances can be employed together to increase the signal-to-noise ratio and extend the intensity interferometry technique to a broader range of targets. We develop a multichannel observation scheme over a broad frequency range, combined with large telescopes, fast photodetectors, and synchronization over large baseline distances. We outline the current capabilities in spectroscopy and picosecond-level timing, and identify the specific advances needed from the recently-demonstrated kilopixel single-photon detector arrays for the EPIC proposal. Modern development of atomic clocks and infrastructure for large baseline radio interferometry make possible picosecond-level synchronization and millimeter-level baseline characterization over the hours-long observation times and kilometer-plus distances needed for intensity interferometry.

We find that EPIC will be able to target stars as faint as magnitude 15, as well as bright quasars, with telescope apertures no larger than 10 m in diameter. The maximum angular source separation for EPIC is limited by the atmosphere’s isoplanatic angle—a few arcseconds in the optical—within which atmospheric fluctuations are correlated.

This work improves on differential astrometry strategies with intensity interferometry in several ways. The feasibility of measuring the relative separation of sources with traditional interferometry was first demonstrated on the close spectroscopic binary α Vir at the original NSII [42], which determined all six Keplerian orbital parameters. Recently, ref. [60] has proposed to target widely separated sources (by more than the isoplanatic angle) with a *fixed* path extension using a single beam splitter and a GHz photon bandwidth per spectral channel. Such a setup imposes exacting (and potentially infeasible) requirements on the adaptive optics and spectroscopic systems. Using the *variable* path extension proposed here, we can track the separation of sources at or near the main path-extended fringe (center of figure 4b) and employ the differential wavefront tilt correction to avoid fringe suppression for sources separated by more than a few milliarcseconds. Our approach yields a per-epoch light-centroiding precision that scales as $t_{\text{obs}}^{-1/2}$ (eq. 2.51), compared to the fringe-scanning method of ref. [60] at extremely high fringe orders, which could lead to fringe confusion and scales as $t_{\text{obs}}^{-3/2}$.

In addition, while multi-band observation schemes have been proposed in recent years [50, 60, 61], this work is the first to study the optical tolerances induced by such a scheme. The few picosecond time-resolution assumed in this work allows for errors in optical paths as long as a millimeter. The desired spectral resolution and the small pixel sizes of ultra-fast photon counters are the limiting factors, and can tolerate primary-mirror imperfections as large as tens of wavelengths, in contrast to imaging telescopes and amplitude interferometers that require sub-wavelength polishing [115].

We also provide the first quantitative study of a fringe contrast suppression for very fast photodetectors and large pixels—unique to ultra-fast and multi-channel intensity interferometry and an entirely new effect unveiled in this work. This perhaps surprising effect originates for setups with photodetector arrays and spectroscopic splitting: atmospheric and instrumental aberrations require the angle subtended by each pixel to be larger than the diffraction limit of each telescope, resulting in uncorrelated fluctuations within a pixel. We identify several possible solutions to this problem, and focus on the conceptually simplest: splitting the beam exiting the EPIC optical delay system into several sub-beams, each with its own dispersion element and photodetector array.

Finally, we calculate effects from atmospheric aberrations and their limitation on the maximum source separation of order the isoplanatic angle for a ground-based intensity interferometer; correcting for atmospheric turbulence over angular separations significantly larger than the isoplanatic patch is beyond the capabilities of present adaptive optics systems [115]. In the future, should a lunar observatory be established, an EPIC observatory would be an clear candidate that would benefit from the absence of an atmosphere; study of a large opening angle design without atmospheric limitations is left to future work.

We present several scientific applications that would experience major leaps forward by leveraging the differential astrometric capabilities of EPIC. The target sources of interest in the Milky Way are binary systems, accidental double stars, and strong microlensing events. EPIC could detect exoplanets astrometrically through the wobble they impart on their host stars with a reach orders of magnitude better than *Gaia*'s projected DR5 [1]. An EPIC interferometer targeting a binary system could determine all Keplerian angles to a sub-degree level and, combined with radial velocity measurements, determine the masses of the constituent stars and the line-of-sight distance to the per-mil level or better. This level of precision would open up possibilities of measurements of stellar mass loss and cosmic distance ladder calibration. Observations of accidental double stars can be used to detect astrometric microlensing and determine stellar masses to the sub-percent level and, with later Phases of the setup, map the potential of the Milky Way by directly measuring the induced stellar accelerations at the nas/yr^2 level, significantly surpassing *Gaia* sensitivity [15]. Finally, EPIC could target *extragalactic* sources such as quasars (and possibly supernovae). We study the specific case of measuring the astrometric evolution of the images in a multiply-imaged quasar to characterize the strong-lensing system and determine peculiar velocities at cosmological distances.

Directions for future work are numerous. At the level of design, identifying a simpler solution to the aforementioned spectroscopic suppression is important to reducing both complexity and cost, potentially allowing the construction of several baselines and many telescopes per observation site. Potential sources of observational systematic uncertainties, such as contamination from ambient light or other sources in a crowded field, should be characterized in more detail. On the experimental side, it is crucial to demonstrate kilo-pixel arrays of single-photon detection devices tailored to the requirements of EPIC, including broadband sensitivity to a wide range of wavelengths. Naturally, a laboratory demonstration of the

EPIC’s path-extension system would be the first step to large-scale implementation.

Further study of the full scientific potential of the applications is also of interest. While we use real example systems to illustrate the power of our technique, we have not performed an exhaustive survey of potential sources. For instance, thousands of microlensing events are predicted to occur in the next few decades based on the *Gaia* catalog alone [186], hundreds of which could be targeted by EPIC. *Gaia* data can also be used to construct a larger double-star catalog to map out the Milky Way’s potential via the relative transverse angular accelerations it imparts on source pairs. Finding sufficiently bright and distant binary systems of Cepheids and other giant stars would aid in refining the first rung of the cosmic distance ladder.

We have also foretold the possibility to probe sub-solar-mass dark matter substructure using astrometry on the multiple images of strongly lensed quasars, which will be studied in detail in a future paper [128]. In addition, we expect EPIC may test general relativity in the vicinity of Sagittarius A* [203–205], with potentially sufficient sensitivity to measure the spin of the central black hole and surrounding mass distribution [206]. Finally, it would be interesting to generalize our analysis of multi-channel intensity interferometry (with and without path extension) to other extended, high surface brightness sources, such as the various types of novae and the cores of globular clusters and galaxies, and investigate corresponding applications.

Extended-Path Intensity Correlation will enable new sets of astronomical measurements at unprecedented precision. It has the potential to transform our knowledge about stellar systems and the Milky Way, and may ultimately provide a new window into the dark universe and physics Beyond the Standard Model.

Acknowledgments

We thank Gordon Baym, Megan Bedell, Karl Berggren, Michael Blanton, Matteo Cantiello, Cyril Creque-Sarbinowski, Liang Dai, Neal Dalal, Julianne Dalcanton, Peter Graham, David Hogg, Miguel Morales, Oren Slone, and David Spergel for valuable conversations and input, and Calvin Chen, Jacob Crawford, Cyril Creque-Sarbinowski, David Dunsky, Marius Kongsore, and Jessie Yang for comments on the manuscript. KVT thanks Jason Aufdenberg, Matthew Brown, James Buckley, Dainis Dravins, David Kieda, Michael Lisa, Nolan Matthews, Andrei Nomerotski, Ue-Li Pen, Naomi Vogel, Shiang-Yu Wang, and Luca Zampieri for fruitful conversations, and Sebastian Karl for pointing out ref. [63], during the 2023 Workshop on Stellar Intensity Interferometry at The Ohio State University. KVT is supported by the National Science Foundation under Grant PHY-2210551. NW is supported by NSF under award PHY-2210498, by the BSF under grant 2018140, and by the Simons Foundation. MB is supported by the DOE Office of Science under Award Number DE-SC0022348, University of Washington Royal Research Fund and through the Department of Physics and College of Arts and Science at the University of Washington.

The Center for Computational Astrophysics at the Flatiron Institute is supported by the Simons Foundation. Research at Perimeter Institute is supported in part by the Government of Canada through the Department of Innovation, Science and Economic Development and by the Province of Ontario through the Ministry of Colleges and Universities.

Part of this work was performed at the Aspen Center for Physics, which is supported by National Science Foundation grant PHY-1607611 and PHY-2210452. The participation of MB at the Aspen Center for Physics was supported by the Simons Foundation. MB, MG, and KVT thank the Institute for Nuclear Theory at the University of Washington for its kind

hospitality and stimulating research environment. The INT is supported in part by the U.S. Department of Energy grant No. DE-FG02-00ER41132.

This work has made use of data from the European Space Agency (ESA) mission *Gaia* (<https://www.cosmos.esa.int/gaia>), processed by the *Gaia* Data Processing and Analysis Consortium (DPAC, <https://www.cosmos.esa.int/web/gaia/dpac/consortium>). Funding for the DPAC has been provided by national institutions, in particular the institutions participating in the *Gaia* Multilateral Agreement. This research has made use of the NASA Exoplanet Archive, which is operated by the California Institute of Technology, under contract with the National Aeronautics and Space Administration under the Exoplanet Exploration Program.

A Notation

In tables 2–7, we relist all variables used in this work in the first column, along with their definitions in the second column.

Variable	Definition
E_p	Total electric field at telescope p
$E_{i\alpha}$	Electric field amplitude of i and of energy k_α
I, \tilde{I}_j	Intensity, fractional intensity of emitter j
$k = 2\pi/\lambda, \bar{k}$	Wavenumber (in terms of wavelength), mean wavenumber
$\hat{\theta}_j$	Unit vector to j
$\theta_{ij} = \hat{\theta}_i - \hat{\theta}_j$	Relative angular distance of i and j .
r_{ip}	Distance of i from telescope p
$\phi_{i\alpha}^{\text{em}}$	Intrinsic phase of emitter i and energy k_α
$\tilde{\phi}_{i\alpha}^{(p)}$	Aberration phase at telescope p
$dI/(dkd\Omega)$	Intensity (power per area) per unit wavenumber and unit solid angle

Table 2: Electric field variables.

Variable	Definition
\mathbf{d}	Baseline vector
\mathbf{b}	Aperture vector
A_i	Area of aperture of telescope i
D	Diameter of primary mirror
f, f', f_c	Focal lengths of primary, secondary, and camera
n_p^{arr}	Number of telescopes at array site p
α_{nlm}	Optical aberration amplitude
ℓ_p	Geometric path extension at telescope p
γ	Angle of first beam-splitter
γ', δ'	Angles of wavefront correction mirror
ϵ	Transmission coefficient of beam splitter
N	Number of illuminated lines on diffraction grating
d_g	Periodicity of grating
s	Slit size of grating
θ_F	Angle from camera to the pixel plane
\mathcal{R}	Spectroscopic resolution
σ_k	Range of wavenumbers on incident on pixel
τ	Timing offset
$\sigma_t/\sqrt{2}$	Timing precision per photodetector
t_{obs}	Observation time per epoch
t_{jitter}	Time jitter of photodetector (FWHM)
t_{reset}	Photodetector reset time
DCR	Dark count rate of photodetector
N_p	Total number of photons incident at p after time t_{obs}
η_p	Photodetection efficiency of p
$C(\mathbf{d}, \tau)$	Intensity correlation
\hat{X}	Estimator of X
$\langle X \rangle$	Expectation value of X (averaged over mode phases)
$\bar{X}(t)$	Time average of $X(t)$ over observation time
$\sigma_{\hat{C}}$	Standard deviation of \hat{C}
$\sigma_{\theta_{\text{res}}}$	Angular resolution of the interferometer
$\sigma_{\Delta\theta}$	Angular dynamic range of the interferometer
$\sigma_{\hat{\theta}}$	Global astrometric precision

Table 3: Instrumental variables.

Variable	Definition
$n[\mathbf{r}]$	Atmospheric index at 3D position \mathbf{r}
$D_n(r)$	Structure function, r -dependent
h	Altitude in the atmosphere
$C_n(h)$	Structure function, dependence on altitude h
l_0	Inner turbulence scale
L_0	Outer turbulence scale
$B_n(r)$	Correlation function of atmospheric index of refraction
$\theta_0(\bar{k}, \gamma)$	Isoplanatic patch angle at an angle γ away from zenith
$\sigma_{\phi}^{\text{atm}}$	Standard deviation of differential phase fluctuation due to the atmosphere
θ_{seeing}	Seeing angle
r_0	Fried parameter

Table 4: Atmospheric fluctuation variables from section 2.5, appendix B.2, and appendix C.3.

Variable	Definition
R_s	Stellar radius
D_s	Distance to star/binary
θ_s	Angular radius of star
M_j	Mass of star j
T_j	Temperature of j
\mathcal{F}_j	Finite-size form factor of j
$T_{500} = 2\pi\hbar c/500 \text{ nm}$	Black body temperature corresponding to 500 nm
R_{500}	Physical radius in quasar's local frame with temperature T_{500}
z_q	Quasar redshift
R_{isco}	Innermost stable circular orbit radius of quasar
$T_{q,0}$	Quasar reference temperature

Table 5: Single source parameters.

Variable	Definition
f_{rep}	Observational repetition frequency
G	Gravitational constant
M	Total binary mass
a	Semi-major axis
e	Eccentricity
i	Inclination
Ω	Longitude of ascending node
ω	Argument of periapsis
ν	True anomaly
t_0	Reference epoch
E	Eccentric anomaly
\mathcal{M}	Mean anomaly
P	Period of binary
z_i	Radial velocity of star i
K_i	Radial velocity semi-amplitude of star i

Table 6: Binary system parameters from sections 4.1 and 4.2.

Variable	Definition
μ_+, μ_-	Magnification factor of + and - images
$\boldsymbol{\mu}$	Angular velocity
$\boldsymbol{\alpha}$	Angular acceleration
ϖ	Parallax
θ_E	Einstein angle
Φ	Gravitational potential
$\boldsymbol{\beta}$	Source-plane location
$\boldsymbol{\varphi}$	Lensing map
A_{ij}, B_{ij}	Macro-lensing Jacobian and its inverse

Table 7: Microlensing parameters from sections 4.3 and 4.5.

B Derivations

B.1 Intensity correlation noise

In what follows, we derive expressions for the expectation values of various moments of the intensity estimator $\hat{I}_p(t_p)$ from eq. 2.43. Firstly, its time average

$$\overline{\hat{I}_p(t_p)} \equiv \frac{1}{t_{\text{obs}}} \int_{t_p - t_{\text{obs}}/2}^{t_p + t_{\text{obs}}/2} dt' \hat{I}_p(t') \quad (\text{B.1})$$

is expected to equal the true intensity $\langle I_p \rangle$, since it is an unbiased estimator:

$$\langle \overline{\hat{I}_p(t_p)} \rangle = \frac{\hbar c \bar{k}}{\eta_p A_p} \int_{t_p - t_{\text{obs}}/2}^{t_p + t_{\text{obs}}/2} \frac{dt'}{t_{\text{obs}}} \sum_{i=1}^{N_p} \int \frac{dt_i}{t_{\text{obs}}} \frac{e^{-\frac{(t' - t_i)^2}{\sigma_t^2}}}{\sqrt{\pi} \sigma_t} = \frac{\hbar c \bar{k}}{\eta_p A_p} \frac{N_p}{t_{\text{obs}}} \equiv \langle I_p \rangle. \quad (\text{B.2})$$

Again, because $\hat{I}_p(t_p)$ from eq. 2.43 is an unbiased estimator of the local intensity field, it also faithfully reflects the intensity *correlations* at detectors $p = 1$ and $p = 2$:

$$\langle \overline{\hat{I}_1(t_1) \hat{I}_2(t_2)} \rangle = \langle \overline{\hat{I}_1(t_1)} \rangle \langle \overline{\hat{I}_2(t_2)} \rangle \left[1 + \underbrace{C(\mathbf{d}, \ell, t_2 - t_1)}_{\text{correlations} \ll 1} \right] \quad (\text{B.3})$$

$$\simeq \frac{\hbar^2 c^2 \bar{k}^2}{\eta_1 \eta_2 A_1 A_2} \frac{N_1 N_2}{t_{\text{obs}}^2} = \langle I_1 \rangle \langle I_2 \rangle. \quad (\text{B.4})$$

In the second line, we have approximated the excess intensity correlations to be small ($C \ll 1$), which is usually a good approximation. Equation B.4 implies that \hat{C} from eq. 2.44 is also an unbiased estimator of C .

The statistical error on the time-averaged intensities is negligibly small, because:

$$\begin{aligned} \left\langle \left[\overline{\hat{I}_p(t_p)} \right]^2 \right\rangle &\simeq \left(\frac{\hbar c \bar{k}}{\eta_p A_p} \right)^2 \left(\prod_{i=1}^{N_p} \int \frac{dt_i}{t_{\text{obs}}} \right) \int \frac{dt'}{t_{\text{obs}}} \left(\sum_{i=1}^{N_p} \frac{e^{-\frac{(t' - t_i)^2}{\sigma_t^2}}}{\sqrt{\pi} \sigma_t} \right) \int \frac{dt''}{t_{\text{obs}}} \left(\sum_{i=1}^{N_p} \frac{e^{-\frac{(t'' - t_i)^2}{\sigma_t^2}}}{\sqrt{\pi} \sigma_t} \right) \\ &\simeq \left(\frac{\hbar c \bar{k}}{\eta_p A_p} \right)^2 \left(\frac{N_p}{t_{\text{obs}}} \right)^2 = \langle I_p \rangle^2. \end{aligned} \quad (\text{B.5})$$

In other words, the fractional variance of $\overline{\hat{I}_p(t_p)}$ is of order $\mathcal{O}(1/N_p)$, exceedingly small for very bright sources with $N_p \gg 1$ needed to measure C with high SNR. The (fractional) statistical error on the intensity correlations is significantly larger, since it receives contributions only

from near-simultaneous photon arrivals. We find:

$$\begin{aligned}
\left\langle \left[\overline{\hat{I}_1(t)\hat{I}_2(t+\tau)} \right]^2 \right\rangle &= \frac{(\hbar c \bar{k})^4}{(\eta_1 \eta_2 A_1 A_2)^2} \left(\prod_{i=1}^{N_1} \int \frac{dt_i^{(1)}}{t_{\text{obs}}} \right) \left(\prod_{m=1}^{N_2} \int \frac{dt_m^{(2)}}{t_{\text{obs}}} \right) \int \frac{dt'}{t_{\text{obs}}} \int \frac{dt''}{t_{\text{obs}}} \\
&\times \left[\sum_{i=1}^{N_1} \frac{e^{-\frac{(t'-t_i^{(1)})^2}{\sigma_t^2}}}{\sqrt{\pi}\sigma_t} \right] \left[\sum_{m=1}^{N_2} \frac{e^{-\frac{(t'-t_m^{(2)})^2}{\sigma_t^2}}}{\sqrt{\pi}\sigma_t} \right] \left[\sum_{j=1}^{N_1} \frac{e^{-\frac{(t''-t_j^{(1)})^2}{\sigma_t^2}}}{\sqrt{\pi}\sigma_t} \right] \left[\sum_{n=1}^{N_2} \frac{e^{-\frac{(t''-t_n^{(2)})^2}{\sigma_t^2}}}{\sqrt{\pi}\sigma_t} \right] \\
&= \frac{(\hbar c \bar{k})^4}{(\eta_1 \eta_2 A_1 A_2)^2} \frac{1}{t_{\text{obs}}^2} \left(\prod_{i=1}^{N_1} \int \frac{dt_i^{(1)}}{t_{\text{obs}}} \right) \left(\prod_{m=1}^{N_2} \int \frac{dt_m^{(2)}}{t_{\text{obs}}} \right) \sum_{i,j} \frac{e^{-\frac{1}{2\sigma_t^2} \left[(t_i^{(1)}-t_m^{(2)})^2 + (t_j^{(1)}-t_n^{(2)})^2 \right]}}{2\pi\sigma_t^2} \quad (\text{B.6}) \\
&\simeq \frac{(\hbar c \bar{k})^4}{(\eta_1 \eta_2 A_1 A_2)^2} \frac{1}{t_{\text{obs}}^2} \left\{ \left[\sum_{i,m} \int \frac{dt_i^{(1)}}{t_{\text{obs}}} \int \frac{dt_m^{(2)}}{t_{\text{obs}}} \frac{e^{-\frac{1}{2\sigma_t^2} (t_i^{(1)}-t_m^{(2)})^2}}{\sqrt{2\pi}\sigma_t} \right]^2 \right. \\
&\quad \left. + \sum_{i,m} \int \frac{dt_i^{(1)}}{t_{\text{obs}}} \int \frac{dt_m^{(2)}}{t_{\text{obs}}} \frac{e^{-\frac{1}{2\sigma_t^2} (t_i^{(1)}-t_m^{(2)})^2}}{2\pi\sigma_t^2} \right\} \\
&= \frac{(\hbar c \bar{k})^4}{(\eta_1 \eta_2 A_1 A_2)^2} \left[\left(\frac{N_1 N_2}{t_{\text{obs}}^2} \right)^2 + \frac{N_1 N_2}{t_{\text{obs}}^3 \sqrt{4\pi}\sigma_t} \right]
\end{aligned}$$

The latter term in the last equality is responsible for the statistical variance on \hat{C} in the low-SNR limit for each spectral channel. Putting everything together, we find:

$$\sigma_{\hat{C}}^2 \equiv \langle \hat{C}^2 \rangle - \langle \hat{C} \rangle^2 \simeq \frac{\left\langle \left[\overline{\hat{I}_1(t)\hat{I}_2(t+\tau)} \right]^2 \right\rangle - \left[\langle \overline{\hat{I}_1(t)\hat{I}_2(t+\tau)} \rangle \right]^2}{\langle I_1 \rangle^2 \langle I_2 \rangle^2} = \frac{t_{\text{obs}}}{\sqrt{4\pi}\sigma_t} \frac{1}{N_1 N_2}. \quad (\text{B.7})$$

This corresponds to eq. 2.48 from the main text.

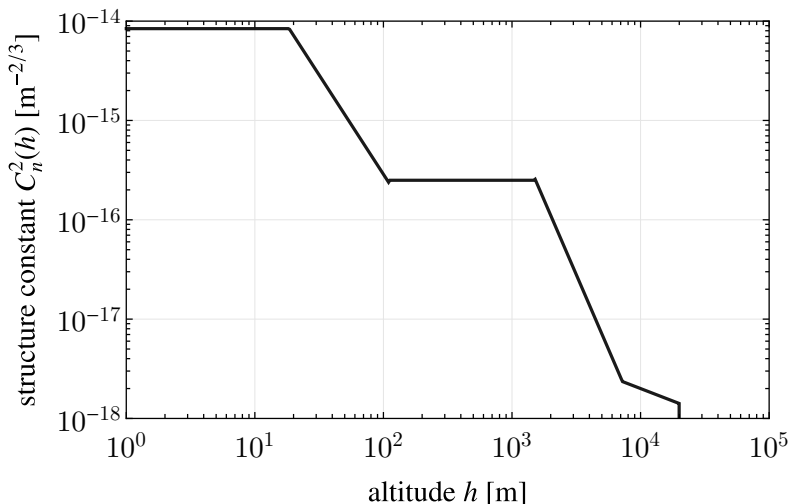


Figure 20: Structure constant C_n^2 for atmospheric refraction from eq. 2.58 as a function of altitude h in the SLC night model.

B.2 Atmospheric aberration

We derive the mean square doubly-differential refraction phase from atmospheric aberrations (eq. 2.60 in the main text). We find:

$$\begin{aligned}
(\sigma_\phi^{\text{atm}})^2 &\equiv \left\langle \left[\Delta\tilde{\phi}^{(1,2)}(\bar{k}, \hat{\theta}_a, \hat{\theta}_b) \right]^2 \right\rangle_{\text{atm}} \\
&= \bar{k}^2 \iint ds ds' \left\langle \left(n[\mathbf{x}_{a1}(s)] + n[\mathbf{x}_{b2}(s)] - n[\mathbf{x}_{a2}(s)] - n[\mathbf{x}_{b1}(s)] \right) \right. \\
&\quad \left. \times \left(n[\mathbf{x}_{a1}(s')] + n[\mathbf{x}_{b2}(s')] - n[\mathbf{x}_{a2}(s')] - n[\mathbf{x}_{b1}(s')] \right) \right\rangle_{\text{atm}} \\
&= \bar{k}^2 \iint_0^{L_{\text{atm}} \sec \gamma} ds ds' \frac{-C_n^2(s \cos \gamma)}{2} \left\{ \right. \\
&\quad + |\mathbf{x}_{a1}(s) - \mathbf{x}_{a1}(s')|^{2/3} + |\mathbf{x}_{b1}(s) - \mathbf{x}_{b1}(s')|^{2/3} + |\mathbf{x}_{a2}(s) - \mathbf{x}_{a2}(s')|^{2/3} + |\mathbf{x}_{b2}(s) - \mathbf{x}_{b2}(s')|^{2/3} \\
&\quad - |\mathbf{x}_{a1}(s) - \mathbf{x}_{b1}(s')|^{2/3} - |\mathbf{x}_{b1}(s) - \mathbf{x}_{a1}(s')|^{2/3} - |\mathbf{x}_{a2}(s) - \mathbf{x}_{b2}(s')|^{2/3} - |\mathbf{x}_{b2}(s) - \mathbf{x}_{a2}(s')|^{2/3} \\
&\quad - |\mathbf{x}_{a1}(s) - \mathbf{x}_{a2}(s')|^{2/3} - |\mathbf{x}_{b1}(s) - \mathbf{x}_{b2}(s')|^{2/3} - |\mathbf{x}_{a2}(s) - \mathbf{x}_{a1}(s')|^{2/3} - |\mathbf{x}_{b2}(s) - \mathbf{x}_{b1}(s')|^{2/3} \\
&\quad \left. + |\mathbf{x}_{a1}(s) - \mathbf{x}_{b2}(s')|^{2/3} + |\mathbf{x}_{b1}(s) - \mathbf{x}_{a2}(s')|^{2/3} + |\mathbf{x}_{a2}(s) - \mathbf{x}_{b1}(s')|^{2/3} + |\mathbf{x}_{b2}(s) - \mathbf{x}_{a1}(s')|^{2/3} \right\}. \tag{B.8}
\end{aligned}$$

To get to the second equality, we plugged in eq. 2.57. To get to the last equality, we used eqs. 2.58 and 2.59. We integrate to the “height” L_{atm} of the atmosphere, though technically $C_n^2(h)$ drops to zero smoothly. In the last four lines, we have expanded the 16 correlation functions into suggestive groups. The last two lines are not correct if $d \gg L_0$, and we will ignore them in what follows; in that regime, the sum of the last two lines (which involve cross-correlations between paths to *different* detectors) is very strongly suppressed. Each of the four terms in the first line are equal to $[(s - s')^2]^{1/3}$, while those in the second line are of

the form $[(\hat{\boldsymbol{\theta}}_a s - \hat{\boldsymbol{\theta}}_b s')^2]^{1/3}$. Putting this all together gives:

$$\begin{aligned}
(\sigma_\phi^{\text{atm}})^2 &\simeq 2\bar{k}^2 \int_0^{L_{\text{atm}} \sec \gamma} \int_0^{L_{\text{atm}} \sec \gamma} ds ds' C_n^2(s \cos \gamma) \left\{ (s^2 - 2ss' \cos \theta_{ba} + s'^2)^{1/3} - (s - s')^{1/3} \right\} \\
&\simeq 2\bar{k}^2 \int_0^{L_{\text{atm}} \sec \gamma} ds C_n^2(s \cos \gamma) \underbrace{\int_{-s}^{+s} dx \left\{ [x^2 + s(s+x)\theta_{ba}^2]^{1/3} - [x^2]^{1/3} \right\}}_{\sqrt{\pi} \frac{\Gamma(-5/6)}{\Gamma(-1/3)} \theta_{ba}^{5/3} - 2\theta_{ba}^2 + \mathcal{O}(\theta_{ba}^{11/3})}. \quad (\text{B.9})
\end{aligned}$$

To get to the last line, we used the small-angle approximation, and used the fact that most of the integral has support at $|x| = |s - s'| \lesssim s$ to separate the integrals. This result, combined with the definition of the isoplanatic patch angle in eq. 2.61, gives eq. 2.60. For reference, we show the dependence of the structure constant $C_n^2(h)$ on altitude h in figure 20.

C Wave Optics

In this appendix, we carry out an analysis using scalar wave optics for the propagation of starlight within each telescope. Emphasis is given on analytic results to understand the requirements for an EPIC intensity interferometer. We include finite telescope apertures and finite pixel sizes in our analysis, as well as atmospheric and instrumental aberrations. Some simplifications and idealizations are necessarily made, and we leave a detailed numerical study to future work.

The structure of this appendix follows the depiction of our setup in figure 5: section C.1 treats the primary and secondary mirrors, section C.2 the optical elements of the geometric path-delay system, section C.3 the effect of aberrations on image formation, and finally section C.4 presents the details of the calculation of section 3.4 concerning the seeing angle suppression for large telescopes and fast photodetectors resulting from the spectroscopic instrument.

C.1 Primary and secondary mirrors

The focus of this section is the derivation of the spatial profile of the electric field, after collimation from the secondary mirror (as depicted in figure 5a), in the presence of mirror distortions. Our main result here is the functional dependence of the electric field profile on the focal ratio of the two mirrors, which magnifies both stellar separations and wavefront aberrations induced by the primary mirror.

Let two point-like stars, a and b , emit monochromatic spherical waves of wavenumber k . Right before incidence on the parabolic mirror of a telescope, the electric field is given by

$$\begin{aligned}
E_k(\mathbf{x}, t) &= A e^{i\omega t} e^{-ik|\mathbf{r}_a + \mathbf{x}| + i\phi_a^{\text{em}} + i\tilde{\phi}_a^{\text{atm}}(\mathbf{x}, t)} + B e^{i\omega t} e^{-ik|\mathbf{r}_b + \mathbf{x}| + i\phi_b^{\text{em}} + i\tilde{\phi}_b^{\text{atm}}(\mathbf{x}, t)} \\
&\simeq e^{i\omega t} \left(A e^{-ik(r_a + \mathbf{x} \cdot \hat{\boldsymbol{\theta}}_a) + i\phi_a^{\text{em}} + i\tilde{\phi}_a^{\text{atm}}(\mathbf{x}, t)} + B e^{-ik(r_b + \mathbf{x} \cdot \hat{\boldsymbol{\theta}}_b) + i\phi_b^{\text{em}} + i\tilde{\phi}_b^{\text{atm}}(\mathbf{x}, t)} \right), \quad (\text{C.1})
\end{aligned}$$

where A and B are the amplitudes of the electric field of each star on the telescope, \mathbf{r}_i is the physical location of star i on the sky, \mathbf{x} a 2D vector on a plane parallel to the telescope's aperture (denoted \mathbf{b} in section 2), centered at the vertex of the parabolic mirror, and $\hat{\boldsymbol{\theta}}_i \equiv \mathbf{r}_i / r_i$ the unit vector pointing to the position of star i . Because \mathbf{x} is a 2D vector, we can trade $\hat{\boldsymbol{\theta}}_a$ for its component parallel to \mathbf{x} , which we denote $\boldsymbol{\theta}_a$ without the hat. Clearly the telescope is pointed such that $|\boldsymbol{\theta}_a| \ll 1$. The phase ϕ_i^{em} is the random phase of the emitter i and $\tilde{\phi}_i^{\text{atm}}(\mathbf{x}, t)$

is the space- and time-dependent phase the wave from emitter i inherits from passing through turbulent layers of the atmosphere. In the second line we neglected wavefront curvature effects $\sim k|\mathbf{x}|^2/r \ll 1$. In what follows we will also drop the explicit time-dependence $e^{i\omega t}$.

We take the primary mirror to have diameter D and centered at $\mathbf{x} = 0$, with a surface given by

$$z_{\text{primary}}(\mathbf{x}) = \frac{|\mathbf{x}|^2}{4f} + \frac{1}{2}\tilde{z}^{\text{inst}}(\mathbf{x}), \quad |\mathbf{x}| \in [0, D], \quad (\text{C.2})$$

where the first term corresponds to an ideal spherical paraboloid of focal length f and \tilde{z}^{inst} describes its deformations, which induce *instrumental* (as opposed to atmospheric) aberrations on the wavefront. We will assume that their effect is achromatic.

Using the Kirchhoff-Helmholtz diffraction integral [111], the electric field from star a at a distance $z \gg (D/2)^2/(4f)$ from the primary mirror will be given by

$$E_{a,k}(\mathbf{x}', z) = A \frac{-ik}{2\pi z} \exp \left[-ikr_a + i\phi_a^{\text{em}} + ik \left(z + \frac{x'^2}{2z} \right) \right] \times \int d^2x \exp \left\{ ik \left[-\frac{x^2}{2} \left(\frac{1}{f} - \frac{1}{z} \right) - \mathbf{x} \cdot \left(\frac{\mathbf{x}'}{z} + \boldsymbol{\theta}_a \right) + \tilde{z}^{\text{inst}}(\mathbf{x}) \right] + i\tilde{\phi}_a^{\text{atm}}(\mathbf{x}, t) \right\}, \quad (\text{C.3})$$

where \mathbf{x}' is the 2D vector on a surface perpendicular to propagation. The spatial profile, as described by the second line, is intuitive: the first term describes smearing due to defocusing, which vanishes at the focal plane $z = f$, while the second term would give the usual diffraction limited electric field profile centered at $-\boldsymbol{\theta}_a$ on the focal plane, in the absence of aberrations.

Analogous considerations apply for the secondary parabolic mirror that collimates the beam. We find at a distance z from the vertex of the secondary mirror

$$E_{a,k}^{\text{coll}}(\mathbf{x}', z) = A \exp \left[-ikr_a + i\phi_a^{\text{em}} + ik(z + f - f') \right] \frac{f}{f'} \frac{kF^{-1}(z)}{\pi} \int d^2x \exp \left\{ ik \left[F^{-1}(z) \left(\mathbf{x} - \frac{f}{f'}\mathbf{x}' \right)^2 + \mathbf{x} \cdot \boldsymbol{\theta}_a + \tilde{z}^{\text{inst}}(\mathbf{x}) \right] + i\tilde{\phi}_a^{\text{atm}}(\mathbf{x}, t) \right\}, \quad (\text{C.4})$$

where $F^{-1}(z) \equiv \frac{f'}{2f} \frac{1}{z \frac{f}{f'} + f - f'}$ and \mathbf{x}' is, again, the 2D vector on a surface perpendicular to propagation. In deriving this result we have assumed for simplicity that the secondary mirror is an ideal paraboloid, large enough to collect all the light from the primary and not induce any further diffraction effects. In what follows, we suppress the atmospheric phase for brevity, as it can formally be treated in the same way as instrumental aberrations.

We wish to gain some analytic understanding of the electric field profile that exits the two-mirror system, in the presence of potentially large (compared to the wavelength) aberrations, i.e. in the limit $k\tilde{z}^{\text{inst}} \gg 1$. This can be done with the stationary phase approximation.

We define the exponent to be $g(\mathbf{x}) \equiv \left[F^{-1}(z) \left(\mathbf{x} - \frac{f}{f'}\mathbf{x}' \right)^2 + \mathbf{x} \cdot \boldsymbol{\theta}_a + \tilde{z}^{\text{inst}}(\mathbf{x}) \right]$. In the ideal mirror case $\tilde{z}^{\text{inst}}(\mathbf{x}) = 0$ and the equations $\partial_x g = 0$ and $\partial_y g = 0$ have the simple solutions (critical points) $x = x'f/f'$ and $y = y'f/f'$. Since $|\mathbf{x}| \in [0, D/2]$, it follows that $|\mathbf{x}'| \in [0, Df'/(2f)]$, so the collimated beam exists over a smaller spatial extent, given by the geometric optics width of the beam at the plane of the secondary mirror.

We may then approximate

$$\int d^2x \exp[ikg(\mathbf{x})] \simeq \begin{cases} \pi F(z) \exp(ikf\mathbf{x}' \cdot \boldsymbol{\theta}_a/f')/k & \text{for } |\mathbf{x}'| \in \left[0, \frac{f}{f'} \frac{D}{2}\right], \\ 0 & \text{elsewhere} \end{cases}, \quad (\text{C.5})$$

so that the collimated beam has modulus $|E(\mathbf{x}', z)| = Af/f'$ and its extent is $|\mathbf{x}'| \in [0, Df'/(2f)]$. The key takeaway is that, on the \mathbf{x}' plane, the angle $\boldsymbol{\theta}_a$ appears magnified by the magnification f/f' , as expected from geometric optics. Due to the prefactor f/f' of eq. C.4, the energy of the beam is conserved.

In the presence of mirror imperfections \tilde{z}^{inst} , critical points cannot always be found analytically, but we may work in the limit where they induce small corrections to the shape of the collimated beam. As an example, in this limit the critical points in the x direction are

$$x \simeq \frac{f}{f'}x' - \frac{F(z)}{2} \left[\theta_a^{(x)} + \left. \frac{\partial \tilde{z}^{\text{inst}}}{\partial x} \right|_{x=\frac{f}{f'}x'} \right], \quad (\text{C.6})$$

where we took $\partial_x \tilde{z}^{\text{inst}}$ to be a perturbation on the zeroth order solution $x \simeq x^{(0)} = x'f/f'$ and $\theta_a^{(x)}$ is the x -coordinate of $\boldsymbol{\theta}_a$. One can work out optical tolerances for the primary mirror due to this approximation, but they turn out to be less tight compared to those of section C.3 that concern pixel sizes. Thus, we do not discuss them here.

Having established the above, we can approximate the collimated beam for both stars as

$$\begin{aligned} E_{k,\text{coll}}(\mathbf{x}', z) \simeq & \frac{f}{f'} \exp[ik(2(f-f')-z)] \exp \left\{ ik \left[\frac{F(d)}{4} (\nabla \tilde{z}^{\text{inst}})^2 \Big|_{\mathbf{x}=\frac{f}{f'}\mathbf{x}'} + \tilde{z}^{\text{inst}} \left(\frac{f}{f'}\mathbf{x}' \right) \right] \right\} \\ & \left[A \exp \left[-ikr_a + i\phi_a^{\text{em}} + i\tilde{\phi}_a^{\text{atm}} \left(\frac{f}{f'}\mathbf{x}', t \right) \right] \exp \left\{ ik \left[\frac{f}{f'}\mathbf{x}' \cdot \boldsymbol{\theta}_a - \frac{F(d)\boldsymbol{\theta}_a^2}{4} \right] \right\} \right. \\ & \left. + B \exp \left[-ikr_b + i\phi_b^{\text{em}} + i\tilde{\phi}_b^{\text{atm}} \left(\frac{f}{f'}\mathbf{x}', t \right) \right] \exp \left\{ ik \left[\frac{f}{f'}\mathbf{x}' \cdot \boldsymbol{\theta}_b - \frac{F(d)\boldsymbol{\theta}_b^2}{4} \right] \right\} \right], \end{aligned} \quad (\text{C.7})$$

where $|\mathbf{x}'| \in [0, Df'/(2f)]$, z is the coordinate distance with the primary mirror's vertex being at $z=0$, and $d=f-f'-z$ is the (positive) distance from the secondary mirror. In deriving this expression we have dropped the dependence of \tilde{z}^{inst} on $\boldsymbol{\theta}_a, \boldsymbol{\theta}_b$, as it is small. To simplify notation hereafter we will denote the full wavefront aberration imprinted by the primary-secondary mirror system as $\tilde{z}^{\text{inst}}(f\mathbf{x}'/f')$, instead of the full exponent in the first line above, and drop the $\propto \boldsymbol{\theta}^2$ terms.

The most important feature of our result, eq. C.7, is the appearance of the magnification factor f/f' multiplying the physical positions of the stars and the arguments of the aberration functions, both instrumental and atmospheric. This is not a surprising result: just as relative stellar separations $\boldsymbol{\theta}_a - \boldsymbol{\theta}_b$ are magnified by f/f' , so does the seeing angle due to the rescaled argument of $\tilde{\phi}^{\text{atm}}$, and the mirror-induced wavefront aberrations due to \tilde{z}^{inst} .

C.2 The EPIC optical system

The EPIC optical delay module has the form of a Mach-Zehnder interferometer of unequal path lengths, achieved by positioning the first beamsplitter at an angle $\gamma \neq 45^\circ$, as shown

in figure 5b and described in section 2. This system’s role is twofold: it both induces the geometric path delay that expands the field of view, and corrects for the wavefront tilt between the images of the two stars. The latter suppresses fringe contrast if uncorrected, an effect known since the advent of intensity interferometry [34] and relevant when each telescope *itself* resolves the angular separation being measured.

In section C.2 we study the induced phases by the multiple reflections within an idealized beamsplitter and technical requirements when operating it with broadband light. In section C.2 we generalize eqs. 2.17 and 2.26 for the geometric path delay and wavefront correction for a general 2D relative stellar separation and derive expressions for the required two-dimensional wavefront correction angle. We conclude by commenting on tolerances relevant to the EPIC module.

Fourier decomposition

The analysis in this section will be carried out with plane waves for clarity. This retains all generality because any wave can be decomposed into plane waves via a Fourier transform, and the effect of all optical elements is linear so that no two wavelengths mix. As such, any electric field $E(\mathbf{r})$, where $\mathbf{r} = (x, y, z)$, can be decomposed as

$$E(\mathbf{r}) \equiv \int d^3p \tilde{E}(\mathbf{p}) e^{-i\mathbf{p}\cdot\mathbf{r}}, \quad \tilde{E}(\mathbf{p}) = \int \frac{d^3x}{(2\pi)^3} E(\mathbf{r}) e^{+i\mathbf{p}\cdot\mathbf{r}}. \quad (\text{C.8})$$

Each Fourier component has a fixed direction and so it is easier to calculate how it transforms after propagation through the EPIC optical system of figure 5b. Formally, the direction will be modified such that

$$\tilde{E}(\mathbf{p}) e^{-i\mathbf{p}\cdot\mathbf{r}} \rightarrow \tilde{E}(\mathbf{p}) e^{-i\mathbf{M}(\mathbf{r})\cdot\mathbf{p}}, \quad (\text{C.9})$$

for some function $\mathbf{M}(\mathbf{r}) \equiv (M_1(x, y, z), M_2(x, y, z), M_3(x, y, z))$ that depends on the optical instruments the wave encounters. We can resum these plane waves into E' at some point after beam-recombination at the exit of the EPIC module so that

$$E'(x, y, z) = E(M_1, M_2, M_3), \quad (\text{C.10})$$

which therefore corresponds to translations and distortions of the shape of the incoming collimated beam.

Beamsplitters

Here we study an idealized beamsplitter, consisting of a single slab of material with index of refraction n_2 . Though this study is necessarily incomplete, we wish to highlight some non-trivial requirements for these optical elements when operated with broadband light. Our main result is that, when accounting for multiple reflections, there are irreducible phases that may extinguish the intensity of certain wavelengths. We defer more complete modeling to future work.

Let a ray propagate in a medium of index of refraction n_1 (air) and be incident on a semi-transparent plate of index of refraction n_2 , at an angle γ . If the angle of refraction is θ , such that $n_1 \sin \gamma = n_2 \sin \theta$ by Snell’s law, the reflection and transmission coefficients at each surface of the plate for the parallel⁵ component of the electric field are [111]

$$n_1 \rightarrow n_2: \quad t = \frac{2n_1 \cos \gamma}{n_2 \cos \gamma + n_1 \cos \theta}, \quad r = \frac{n_2 \cos \gamma - n_1 \cos \theta}{n_2 \cos \gamma + n_1 \cos \theta} \quad (\text{C.11})$$

⁵We will neglect polarization effects throughout the discussion here and derive expressions only for the parallel component.

$$n_2 \rightarrow n_1: \quad t' = \frac{2n_2 \cos \theta}{n_1 \cos \theta + n_2 \cos \gamma} = \frac{n_2 \cos \theta}{n_1 \cos \gamma} t, \quad r' = \frac{n_1 \cos \theta - n_2 \cos \gamma}{n_1 \cos \theta + n_2 \cos \gamma} = -r, \quad (\text{C.12})$$

where $r^2 + tt' = 1$, but $r^2 + t^2 \neq 1$. Naively, the transmitted beam suffers a tt' suppression, compared to the reflected which suffers only an r suppression. Consistency with energy conservation for elements with similar r and t requires taking into account multiple reflections within the beamsplitter [111]. If $E^{(i)}$ is the amplitude of the incident field, then the reflected and transmitted amplitudes are, respectively

$$E^{(r)} = \sqrt{\mathbb{R}} \frac{1 - e^{i\delta}}{1 - \mathbb{R}e^{i\delta}} E^{(i)}, \quad E^{(t)} = \frac{\mathbb{T}e^{i\Phi}}{1 - \mathbb{R}e^{i\delta}} E^{(i)}, \quad (\text{C.13})$$

where $\mathbb{R} \equiv r^2$ and $\mathbb{T} \equiv tt'$, so that $\mathbb{R} + \mathbb{T} = 1$, and the phases accumulated are $\delta = 2k\ell_b n_2 \cos \theta$, where ℓ_b is the width of the beamsplitter, and $\Phi = k\ell_b(n_2 \cos \theta - n_1 \cos \gamma)$.

The reflected and transmitted intensities are

$$\left| \frac{I^{(r)}}{I^{(i)}} \right| = \frac{F \sin^2 \frac{\delta}{2}}{1 + F \sin^2 \frac{\delta}{2}} \equiv |\tilde{\mathbb{R}}|, \quad \left| \frac{I^{(t)}}{I^{(i)}} \right| = \frac{1}{1 + F \sin^2 \frac{\delta}{2}} \equiv |\tilde{\mathbb{T}}|, \quad (\text{C.14})$$

where $F \equiv \frac{4\mathbb{R}}{(1-\mathbb{R})^2}$, and $|\tilde{\mathbb{R}}| + |\tilde{\mathbb{T}}| = 1$ recovers energy conservation. In the main text we denoted $|\tilde{\mathbb{T}}| \equiv \epsilon^2$ for notational simplicity. The intensity of the recombined beam will scale as $|\tilde{\mathbb{R}}|^2 |\tilde{\mathbb{T}}|^2 = \left[|\tilde{\mathbb{R}}| (1 - |\tilde{\mathbb{R}}|) \right]^2$, which is maximized for $|\tilde{\mathbb{R}}| = 1/2$ as shown in the main text.

However, the intensity of the reflected and transmitted beams depends on the wavelength through the phase δ , so that $|\tilde{\mathbb{R}}| = 1/2$ can strictly be achieved for only one wavelength. In order to maximize the intensity in as broad a range of wavelengths as possible, we require both $|\tilde{\mathbb{R}}|^2 |\tilde{\mathbb{T}}|^2 = 1/4$ at a particular wavelength, and that the second derivative $\frac{d^2}{d\delta^2} |\tilde{\mathbb{R}}|^2 |\tilde{\mathbb{T}}|^2$ vanishes, so that the change around the preferred δ is as ‘‘slow’’ as possible. This can be achieved formally for $F = 1$, since the second derivative scales as $\propto (1 - F)$. As seen in the left panel of figure 21, for $F = 1$ the final intensity is equal to 1/4 for a factor of 2 in wavelength, but decreases significantly outside this range. If we choose $\delta = \pi$ to correspond to the central wavelength we are recording, e.g. $\delta(450\text{nm}) = \pi$, then we can cover the region 300 – 600nm with intensity loss $\lesssim 1.7\%$.

Three comments are in order in light of the the above results. First, and most importantly, the beamsplitter will be large compared to the wavelength, so that $\ell_b \gg \lambda$. Figure 21 (left) is periodic in δ with period 2π , so we can choose in general $\delta(450\text{nm}) = (2m + 1)\pi$, $m \in \mathbb{N}$, and then the width of the plate needs to be

$$\ell_b = \frac{2m + 1}{n_2 \sqrt{1 - \frac{n_1^2}{n_2^2} \sin^2 \gamma}} \frac{\lambda}{4}, \quad m \in \mathbb{N}, \quad (\text{C.15})$$

where we have neglected the wavelength dependence of the index of refraction. If one chooses $m > 1$ for λ , the above considerations no longer apply as wavelengths λ' which are $\mathcal{O}(1)$ different from λ (as needed for a broadband setup) will acquire a $\mathcal{O}(1)$ different phase $\delta(\lambda')$, which is not within π of $\delta(\lambda)$: for instance $\lambda/2$ acquires a phase $m\pi/2$ which can be very much different from $m\pi - \pi/2$ for large m . The broadband response of wide beamsplitters will have to be determined experimentally and might entail some $\mathcal{O}(1)$ loss of light. In the limit $\ell_b \gg \lambda$, approximately 83% of the spectrum will exit the beamsplitter with more than half its incident intensity and the total intensity lost will be at most 35%. Alternatively, by

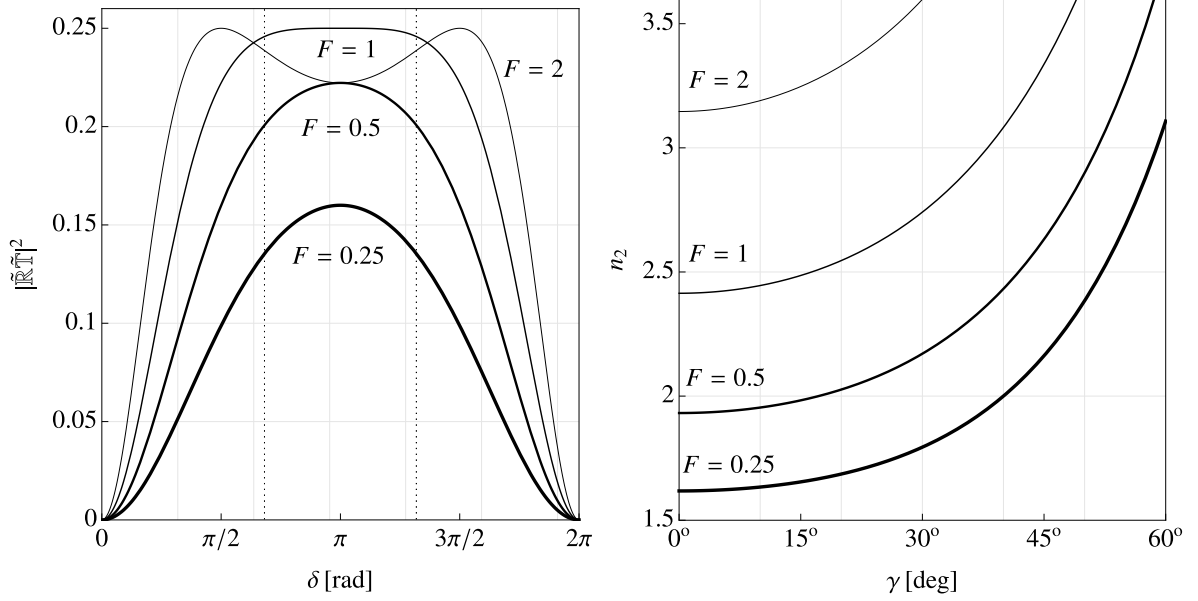


Figure 21: *Left:* Intensity of the main EPIC fringe normalized to total incident intensity, when accounting for multiple reflections within each beamsplitter, as a function of the phase $\delta = 2k\ell_b n_2 \cos \theta$ accumulated after one crossing of the beamsplitter. The product of the reflection and transmission coefficients plotted on the vertical axis is another definition of the quantity $\epsilon^2(1 - \epsilon^2)$ used in e.g. eq. 2.19. The lines, in order of diminishing thickness, correspond to increasing values of the ratio $F \equiv 4\mathbb{R}/(1 - \mathbb{R})^2$, as defined below eq. C.14. The vertical dotted lines correspond to the angles $\pi \pm 1$, within which there is a coverage of a factor of 2 in wavelength. An $F = 1$ beamsplitter has optimal response to broadband light, as proven in the text. *Right:* Required index of refraction n_2 as a function of the incidence angle γ , for different values of F . The index of refraction of air is $n_1 = 1$ and of the beamsplitter n_2 . The thickness grading is the same as in the left figure.

energy conservation, we can retain the full intensity if we made use of both readouts of the second beamsplitter.

Second, the choice of F imposes a specific combination of the incidence angle and the index of refraction, since F is a proxy for the reflection coefficient. In particular, $r^2 = 1 - \frac{2}{F}(\sqrt{1+F} - 1)$, and so the required incidence angle as a function of the indices of refraction and F is given by

$$\cos \gamma = \left[\frac{1 - \frac{n_1^2}{n_2^2}}{\frac{n_2^2}{n_1^2} \left(\frac{1-r}{1+r} \right)^2 - \frac{n_1^2}{n_2^2}} \right]^{1/2}. \quad (\text{C.16})$$

On the right panel of figure 21 we are plotting the required index of refraction of the plate n_2 as a function of the incidence angle γ , for different values of F and assuming $n_1 = 1$ for air. From this figure it is clear that, at least for this toy model, there might be a need for materials with large indices of refraction.

Third, the above discussion concerned intensities, but it is also necessary to know the λ -dependent phase shift of the electric fields due to each beamsplitter, as it may induce smearing

of the intensity fringe we are observing. We find

$$\begin{aligned}
E^{(r)} &= \left(\frac{F \sin^2 \frac{\delta}{2}}{1 + F \sin^2 \frac{\delta}{2}} \right)^{1/2} e^{i\Phi_r} E^{(i)}, \quad \tan \Phi_r \equiv -\frac{(1 - \mathbb{R}) \sin \delta}{(1 + \mathbb{R})(1 - \cos \delta)} \\
E^{(t)} &= \frac{e^{i(\Phi_{t,1} + \Phi_{t,2})}}{(1 + F \sin^2 \frac{\delta}{2})^{1/2}} E^{(i)}, \quad \tan \Phi_{t,1} \equiv \frac{\mathbb{R} \sin \delta}{1 - \mathbb{R} \cos \delta} \quad \text{and} \quad \Phi_{t,2} = \frac{\delta}{2} - k\ell_b n_1 \cos \gamma.
\end{aligned}
\tag{C.17}$$

Assuming that the beamsplitters are identical, the electric field that exits the EPIC module will have accumulated a phase $\Phi_{\text{total}} = \Phi_r + \Phi_{t,1} + \Phi_{t,2}$. For $m > 1$ this phase oscillates rapidly for a finite range of λ and may reduce fringe contrast. The strictest tolerance concerns the size of the beamsplitter, which needs to be such that $\sigma_k \ell_b \lesssim 1$, so that fringe contrast is not lost within each pixel, and must be known with sub-wavelength precision, so that the relative phase delay *between* pixels can be accounted for. The former sets $\ell_b \sim \text{mm}$ and the latter can be determined experimentally.

To summarize, in this section we have studied the broadband response of a beamsplitter made entirely of a single index of refraction. We have identified an irreducible phase contribution that may reduce the intensity of the beam exiting the EPIC module by a third at most, but can be recovered if both readouts of the EPIC module are used. Given our simplistic modeling, we anticipate that experimental work will be needed to optimize these optical elements.

Geometric delay and wavefront correction

In this section, we derive the general expression for the geometric path delay in the case of a relative 2D wavefront angle. We derive the expressions for the required angles of the EPIC system's mirrors, and discuss their tolerances.

In order to achieve the wavefront correction described in section 2, we can tune the upper mirror of the path-extension system at an angle $\gamma' \neq \gamma$, as shown in figure 5b. Because the upper mirror might need to correct for a 2D angle, we must include a small angle δ' with the axis that in figure 5b is perpendicular to the page. We define as ℓ_{\perp} the distance between the first beamsplitter and the mirror of the upper part of the EPIC delay system when $\gamma' = \gamma$ and $\delta' = 0$. This is an unambiguous length convenient for this calculation. It can be shown that $w_p = \ell_{\perp} \sin 2\gamma / \cos \gamma$, where w_p is the length shown on figure 5b.

In the limit $|\gamma - \gamma'| \equiv |\varepsilon| \ll 1$ ⁶ and $\delta' \ll 1$ we find for the $\mathbf{M}(\mathbf{r})$ function of eq. C.9

$$\begin{aligned}
M_1 &\simeq x + y\delta' \sin 2\gamma + 2z(\gamma - \gamma') - 2\ell_{\perp} [(\gamma - \gamma') \cos \gamma + \sin \gamma] \\
M_2 &\simeq -x\delta' \sin 2\gamma + y - z\delta'(1 + \cos 2\gamma) + 2\ell_{\perp} \delta' \cos \gamma \\
M_3 &\simeq -2(\gamma - \gamma')x + y\delta'(1 + \cos 2\gamma) + z - 2\ell_{\perp} [\cos \gamma - (\gamma - \gamma') \sin \gamma].
\end{aligned}
\tag{C.18}$$

These expressions have a simple geometric meaning: for a plane wave only in the z -direction and for $\gamma = \gamma'$ and $\delta' = 0$, the center of the beam is shifted by $2\ell_{\perp} \sin \gamma$ in the x -direction, and gains a phase because of the geometric path between points with the same z -coordinate, $2\ell_{\perp} \cos \gamma$.

⁶Not to be confused with the transmission coefficient ϵ^2 we defined in section 2.

Neglecting instrumental and atmospheric aberrations, the recombined collimated beam exiting the second beamsplitter is then

$$\begin{aligned}
E_k^{\text{recomb}}(\mathbf{x}, z) \simeq & \tilde{\mathbb{R}}\tilde{\mathbb{T}} \frac{f}{f'} \exp [ik(2(f - f') - z)] \\
& \left[A e^{-ikr_a + i\phi_a^{\text{em}}} e^{ikx(2\varepsilon + \frac{f}{f'}\theta_{a,x})} e^{iky(-2\delta' \cos^2 \gamma + \frac{f}{f'}\theta_{a,y})} e^{2ik\ell_{\perp}(\cos \gamma - \varepsilon \sin \gamma - \frac{f}{f'}\theta_{a,x} \sin \gamma)} \right. \\
& + B e^{-ikr_b + i\phi_b^{\text{em}}} e^{ikx(2\varepsilon + \frac{f}{f'}\theta_{b,x})} e^{iky(-2\delta' \cos^2 \gamma + \frac{f}{f'}\theta_{b,y})} e^{2ik\ell_{\perp}(\cos \gamma - \varepsilon \sin \gamma - \frac{f}{f'}\theta_{b,x} \sin \gamma)} \left. \right] \\
& + e^{2ik\ell_{\perp}(\sin \gamma + \varepsilon \cos \gamma)} \left[A e^{-ikr_a + i\phi_a^{\text{em}}} e^{ik\frac{f}{f'}\mathbf{x}\cdot\boldsymbol{\theta}_a} e^{-2ik\ell_{\perp}\frac{f}{f'}\theta_{a,x} \sin \gamma} \right. \\
& \quad \left. + B e^{-ikr_b + i\phi_b^{\text{em}}} e^{ik\frac{f}{f'}\mathbf{x}\cdot\boldsymbol{\theta}_b} e^{-2ik\ell_{\perp}\frac{f}{f'}\theta_{b,x} \sin \gamma} \right],
\end{aligned} \tag{C.19}$$

where we have expanded the exponents to first order in ε and δ' . The overall coefficient $\tilde{\mathbb{R}}\tilde{\mathbb{T}}$ has to do with the beamsplitters and expressions for a simple model can be found in section C.2. We assume that these are identical for both beamsplitters.

The principal EPIC fringe arises from the terms in the third and fourth line of eq. C.19. The relative phase between these two terms is

$$\Delta\phi = ik \left[x \left(2\varepsilon + \frac{f}{f'}\theta_{ba,x} \right) + y \left(-2\delta' \cos^2 \gamma + \frac{f}{f'}\theta_{ba,y} \right) \right] + ik\ell_p \tag{C.20}$$

where we defined $\boldsymbol{\theta}_{ba} = (\theta_{ba,x}, \theta_{ba,y}) \equiv \boldsymbol{\theta}_b - \boldsymbol{\theta}_a$ and ℓ_p is the geometric delay, the tuning of which allows for the expansion of the field of view (see section 2.2). It is given by

$$\ell_p = \frac{\ell_{\perp} \cos(\gamma - \gamma')}{\cos \gamma'} \left[\cos 2\gamma + \cos 2(\gamma - \gamma') - \sin 2\gamma - \sin 2(\gamma - \gamma') \right] - 2\ell_{\perp} \frac{f}{f'} \theta_{ba,x} \sin \gamma, \tag{C.21}$$

where the last term $\propto \theta_{ba,x}$ is in fact $\propto \varepsilon$, so this expression reduces to eq. 2.17 for $\gamma = \gamma'$. The wavefront correction for large apertures and large stellar separations amounts to canceling the x - and y - dependence of $\Delta\phi$ by choosing

$$\varepsilon \equiv \gamma - \gamma' = -\frac{f}{2f'}\theta_{ba,x} \quad \text{and} \quad \delta' = \frac{f}{2f' \cos^2 \gamma} \theta_{ba,y}. \tag{C.22}$$

Wavefront correction and telescope pointing tolerances

The residual angle φ from the aforementioned tuning has to be within the diffraction limit of the telescope, so that $\varphi \lesssim (kD/2)^{-1} \simeq 8 \text{ mas}$ at $\lambda = 500 \text{ nm}$ and for a 4 m diameter primary. The angle has to be both known and tuned to within this precision. The former is satisfied by the first step of the source localization protocol outlined in 3.1, while the latter sets an instrumental tolerance which should be achievable.

Furthermore, we have found a term proportional to (a component of) the magnified relative angle of the two stars in eq. C.21. We remind the reader that ℓ_p must be tuned close to $\mathbf{d} \cdot \boldsymbol{\theta}$, where \mathbf{d} is the baseline vector and $\boldsymbol{\theta}$ the relative stellar separation, to within a wavelength, as discussed in sections 2.2 and in particular 3.1 and 3.2. Even though the magnification factor f/f' can be large, ℓ_{\perp} will only be on the order of tens of cm. As a result, this factor does not induce any stricter tolerances than what we have discussed so far.

Finally, we factored out an overall \mathbf{x} dependent factor $\exp(ikf\mathbf{x} \cdot \boldsymbol{\theta}_a/f')$. This factor includes possible telescope pointing errors and, although similar in form to the relative wavefront tilt, it does *not* lead to fringe suppression. Pointing of the telescope affects the light paths of both stars in the same way, so, in fact, it is largely irrelevant: all it does is shift the overall position of the image on the photodetector array, without any suppression of correlation. The only tolerance on pointing is that any error remains within the angle subtended by each pixel. Seeing fluctuations demand that this angle be at least 1 arcsec, as we will see in section C.4, and stable pointing with such a precision is achievable even with commercial star-guiding systems for amateur astronomy.

C.3 Optical aberrations

In this section, we derive tolerance conditions for our optical systems. We first sketch a proof of the well-known fact that a periodic grating produces an identical image of the source at every wavelength, so it is sufficient to neglect the dispersion of the grating and, rather, study the effects of aberrations on a single image of a point-like source. We derive tolerances on primary aberrations analytically and show that the requirements for intensity interferometry in general, and for EPIC in particular, can be orders of magnitude looser than those of traditional imagers and amplitude interferometers. Towards the end, we revisit atmospheric aberrations, which we studied in sections 2.5 and B.2, this time focusing on the size of the finite seeing disk on the pixel array. We defer a complete numerical study to future work.

Multiple image formation by a diffraction grating

The presence of the diffraction grating complicates the analytic understanding of the 2D image formation at the focal plane in the presence of optical aberrations. Fortunately, we can leverage the well-known fact of spectroscopy that a grating produces a copy of the image at every wavelength and the angular separation of these images on the focal plane is the same as that of the aberration-free images of point-like sources.

We may consider, for simplicity, a 1D grating of periodicity d_g and linear size along the “spectroscopic direction” $w = Nd_g$, where N is the number of illuminated slits of width $s < d$, and a wave $E_k \propto \exp\{ik[z + \tilde{z}(x)]\}$ at normal incidence with wavefront aberrations \tilde{z} . Here, z is the direction of propagation and x is the transverse coordinate, namely the one on the plane of the grating. The outgoing light is focused on the photodetector array using a camera of focal length f_c . The amplitude of the wave E_k at the position $\theta_F = x_F/f_c$ on the focal plane is

$$\begin{aligned} E_k(\theta_F) &\propto \sum_{n=-N/2+1}^{N/2} \int_{(2n-1)\frac{d_g}{2}-\frac{s}{2}}^{(2n-1)\frac{d_g}{2}+\frac{s}{2}} d\xi e^{-ik\xi\theta_F} e^{ik\tilde{z}(\xi)} \\ &= \sum_n e^{ik\theta_F(2n-1)d_g/2} \int_{-\frac{s}{2}}^{\frac{s}{2}} d\xi' e^{-ik[\xi'\theta_F - \tilde{z}(\xi' + (2n-1)d_g/2)]}. \end{aligned} \quad (\text{C.23})$$

Because $d > s$ we can ignore the ξ' dependence in the argument of \tilde{z} to get

$$E_k(\theta_F) \propto s \frac{\sin(k\theta_F \frac{s}{2})}{k\theta_F \frac{s}{2}} \sum_n e^{ik\theta_F(2n-1)d_g/2} e^{ik\tilde{z}((2n-1)d_g/2)}. \quad (\text{C.24})$$

Neglecting the single-slit prefactor, which is effectively constant for $\theta_F \ll 1/(ks)$, the remainder is periodic in θ_F with period $T = 4\pi/(kd_g)$. Its modulus has half that period, i.e

$|E(\theta_F + mT/2)| = |E(\theta_F)|$. Thus the profile centered around any diffraction order $m \in \mathbb{Z}$ is the same.

Within a period, we can take the limit $d_g \rightarrow 0$. Then we can approximate $(2n-1)d_g/2 \simeq x$, such that $x \in [-Nd_g/2, Nd_g/2] = [-w/2, w/2]$, for $N \gg 1$. We specialize to the first diffraction peak $m = 1$, to find

$$E_k(\theta_F) \propto \int_{-w}^w dx e^{-ikx\left(\theta_F - \frac{2\pi}{kd_g}\right)} e^{ik\tilde{z}(x)}. \quad (\text{C.25})$$

This is the image of the source in the focal plane as seen through an aperture of width w which imprints aberrations \tilde{z} . The salient feature of this expression is that the angle where each wavelength is focused at, $2\pi/(kd_g)$, depends on the wavelength as one expects from a dispersion grating, but the functional form of the wave profile is the same around that point. Prefactors can be determined from energy conservation.

The argument presented here disentangles the effects of aberrations from the dispersion of the grating and allows us to consider only the aberrated intensity distribution of a monochromatic wave in what follows.

Tolerances on primary aberrations

Intensity interferometry is not sensitive to the precise functional form of the intensity distribution of an image. Instead, the only requirement is that all the light is collected by the photodetector. In the simplest setup, we allocate one pixel per σ_k wavenumbers, so, according to the proof of the previous subsection, we require the spread of a single image to be within this one pixel. We provide a general analytic framework for deriving the spread of the distorted image and calculate tolerances on Seidel aberrations. Our discussion follows ref. [111] and is technical. We refer the reader interested in how (primary) tolerances for EPIC compare to those of regular diffraction-limited telescopes to figure 22 and especially table 8.

Let $\mathbf{x} = (x, y)$ be the 2D cartesian vector on the plane of the photodetector, which lies at $z = z_p$ from a lens of width $w = Nd_g$ and focal length f_c centered at $(\mathbf{x}, z) = (\mathbf{0}, 0)$.⁷ The width of the lens is related to the aperture of the primary by the magnification factor $w \equiv Df'/f$, as we have proven in section C.1, e.g. see eq. C.7. We define the corresponding polar coordinates (r, ϕ) for the focal plane and (ρ, θ) for the lens. The wave at the plane of the photodetector will be, according to eq. C.7:

$$E_k(r, \phi) \propto \int_0^{\frac{w}{2}} d\rho \int_0^{2\pi} d\theta \rho \exp \left[ik \left(\frac{\rho^2}{2} \left(\frac{1}{z_p} - \frac{1}{f_c} \right) - \frac{r}{z_p} \rho \cos(\theta - \phi) + \tilde{z} \left(\frac{f}{f'} \rho, \theta \right) \right) \right]. \quad (\text{C.26})$$

The terms proportional to ρ and ρ^2 in the exponent are known as *distortion* and *curvature of field*, respectively [111]. Both shift the 3D position of the Gaussian focus⁸ and the new position of maximum intensity is referred to as the *diffraction focus*. Crucially, if only such terms exist, they do not change the intensity profile *around* the diffraction focus compared to the profile around the Gaussian focus for an aberration-free system. Therefore, we do not need to set tolerances on these.

⁷The lens here is a proxy for the grating. In the case of a grating there is the additional distance from the grating to the camera mirror/lens.

⁸We remind the reader that this corresponds to the position of maximum intensity for a point-like source, i.e. the center of the Airy pattern. Distortion displaces this point horizontally, within the focal plane where the Airy pattern is, and curvature of field vertically compared to said plane.

It is well known that for a polynomial aberration of the form $\tilde{z} \propto \rho^n$, one can add aberrations of a lower order to maximize the intensity at the Gaussian focus [111]. Because different aberrations shift the diffraction focus by different amounts, it is convenient to expand the aberration function in polynomials that have maximum intensity at the same point and, in particular, at the Gaussian focus. We can directly compare the spread of the image with the aberration-free Airy pattern. This expansion is standard and is done in terms of Zernike polynomials, so that

$$\tilde{\phi}^{\text{inst}}\left(\frac{f}{f'}\rho, \theta\right) = \sum_{l,n,m} \epsilon_{nm} \alpha_{lnm} \bar{\lambda} R_n^m\left(\frac{\rho}{w/2}\right) \cos m\theta, \quad (\text{C.27})$$

where $n \geq m$, $n - m$ is even, $\epsilon_{nm} = 1/\sqrt{2}$ if $m = 0$, $n \neq 0$ and 1 otherwise, and α_{nlm} are dimensionless constants. Because EPIC uses a broadband setup, it is useful to extract a reference length scale $\bar{\lambda}$, which we choose to be 500nm. The polynomials R_n^m can be found in standard references [111]. Terms with $2l + m + n = 4$ correspond to Seidel or primary aberrations.

If the aberration is small and the induced phase $k\tilde{z} \lesssim 1$, tolerances are derived in standard references [111]. If this phase is large, which can be the case for intensity interferometry, we can use the stationary phase approximation to evaluate the integrals of eq. C.26, by identifying the critical points of the exponent. In fact, the precise functional form is not needed, but rather only the area in which most of the intensity lies in. Critical points will exist only for a finite range of ρ and one can prove analytically that the wave profile decays much faster outside this range. Our criterion is that *the pixel must be at least as large as the area in which critical points exist*. We have verified this numerically, as can be seen in figure 22. The intensity lost using this criterion is $\mathcal{O}(1\%)$, but looser requirements, such as the collection of half the intensity, will give parametrically the same tolerances.

As an illustrative example, we will now calculate the tolerance on the primary (Seidel) spherical aberration for the primary mirror.⁹ Essentially identical calculations can be carried out for primary coma and astigmatism. We collect our results in table 8.

For cylindrically symmetric Zernike polynomials $m = 0$, the integral is independent of ϕ and depends only on the ratio $|\theta_F| \equiv r/f_c$, so that

$$E_k(|\theta_F|, \phi) = -\frac{ik e^{ikf_c}}{f_c} \int_0^{w/2} d\rho \rho J_0(k|\theta_F|\rho) \exp\left[ik\tilde{\phi}^{\text{inst}}\left(\frac{f}{f'}\rho\right)\right]. \quad (\text{C.28})$$

Since the spreading due to aberrations is going to be larger than the diffraction limited spread $|\theta_F| \sim \lambda/w$,¹⁰ we can use the asymptotic expansion of the Bessel function and then approximate the integral using the stationary phase approximation.

The $(n, m) = (4, 0)$ Zernike polynomial $R_4^0(x) = 6x^4 - 6x^2 + 1$ corresponds to the primary spherical aberration $\tilde{z}(\rho) = \alpha_4' \bar{\lambda} (\rho/(w/2))^4$. Critical points exist only for $|\theta_F| \leq 2(6/\sqrt{2})\alpha_{4,0}\bar{\lambda}/(w/2) \equiv \theta_{4,0}$. This we must match with the angle subtended by a pixel of diameter Δx_p at Gaussian focus a distance f_c from the camera lens. Rescaling α_4 to correspond

⁹Technically, Seidel aberrations correspond to simple monomials, in contrast to the Zernike polynomials. Because the Maréchal criterion for a well-corrected system refers to the diffraction focus (that the rms wavefront error should be less than $\lambda/14$), it is simpler to first derive tolerances of the Zernike polynomial of the same order n as the corresponding Seidel aberration, and then match the coefficients [111].

¹⁰The physical angle of a diffraction limited image is λ/w , where $w = f'D/f$. This is not in conflict with the fact that the diffraction limit of the telescope is λ/D since any *relative* angle on the sky will be magnified by f/f' .

Type of aberration	Form of $\tilde{z}(\rho, \theta)$	Tolerance	Wavefront error (rms)	Maréchal criterion
Spherical aberration	$\alpha'_4 \bar{\lambda} \left(\frac{\rho}{D/2}\right)^4$	$\alpha'_4 \lesssim 50$	$\sim 3.8\bar{\lambda}$	$\alpha'_4 \bar{\lambda} \lesssim 0.94\lambda$
Coma	$\alpha'_{3,1} \bar{\lambda} \left(\frac{\rho}{D/2}\right)^3 \cos \theta$	$\alpha'_{3,1} \lesssim 43$	$\sim 5\bar{\lambda}$	$\alpha'_{3,1} \bar{\lambda} \lesssim 0.60\lambda$
Astigmatism	$\alpha'_{2,2} \bar{\lambda} \left(\frac{\rho}{D/2}\right)^2 \cos^2 \theta$	$\alpha'_{2,2} \lesssim 100$	$\sim 20\bar{\lambda}$	$\alpha'_{2,2} \bar{\lambda} \lesssim 0.35\lambda$
Curvature of field	$\alpha_2 \bar{\lambda} \left(\frac{\rho}{D/2}\right)^2$	-	-	-
Distortion	$\alpha_{1,1} \bar{\lambda} \left(\frac{\rho}{D/2}\right) \cos \theta$	-	-	-

Table 8: Tolerances on Seidel aberrations assuming that all the intensity of a single spectral channel is recorded by a *single* pixel. In the third column the tolerance is set by imposing that all the intensity (see text for a precise definition) falls within a pixel of linear size of $20\mu\text{m}$, for a telescope with $f/f' = 10$, a $D = 10\text{m}$ primary and a $f_c = 100\text{mm}$ camera focal length, at the reference wavelength of $\bar{\lambda} = 500\text{nm}$. The fourth column relates the tolerance to the rms wavefront error or, equivalently, to twice the rms surface error of the primary mirror. In the last column we give the corresponding Maréchal criterion for a diffraction limited system from [111] for comparison. Larger pixels, allocation of more pixels per spectral channel and smaller magnifications can further alleviate these requirements.

to the Seidel coefficient α'_4 , we find

$$\alpha'_4 \lesssim 50 \left(\frac{\Delta x_p}{20\mu\text{m}}\right) \left(\frac{100\text{mm}}{f_c}\right) \left(\frac{D}{10\text{m}}\right) \left(\frac{500\text{nm}}{\bar{\lambda}}\right) \left(\frac{10}{f/f'}\right). \quad (\text{C.29})$$

This should be contrasted to the Maréchal criterion (the rms wavefront error of a sphere centered at the diffraction focus should be smaller than $\lambda/14$ for a diffraction limited system) which for a primary spherical aberration yields $\alpha'_4 \bar{\lambda} \lesssim 0.94\lambda$. For this choice of parameters, the rms wavefront error is $3.75\bar{\lambda}$, which corresponds to twice the tolerable surface rms error for the primary mirror¹¹. As such, even in the presence of small pixels, intensity interferometry can tolerate aberrations an order of magnitude larger than diffraction limited designs. Because the surface rms error is about a micron, rather than significantly sub-wavelength, many of the expensive and time-consuming mirror polishing processes could be skipped [115]. Larger pixels, allocation of multiple pixels to a single aberrated image and smaller magnifications can all further loosen this tolerance.

Atmospheric aberrations

The atmosphere is another source of image aberrations that broadens the area into which the light is focused on the photodetector. We have established in sections 2.5 and B.2 that sources within the isoplanatic angle suffer the same stochastic image variations from the atmosphere, so that the contrast of the main EPIC fringe is not diminished. Here we are concerned with the size of the distorted image over long timescales, which is known as the *seeing* disk. As

¹¹The rms wavefront error $\Delta\tilde{z}$ of the aberration function \tilde{z} is defined as

$$(\Delta\tilde{z})^2 \equiv \frac{1}{\pi} \int_0^1 \int_0^{2\pi} (\tilde{z} - \langle\tilde{z}\rangle)^2 \rho \, d\rho d\theta, \quad \text{where} \quad \langle\tilde{z}\rangle \equiv \frac{1}{\pi} \int_0^1 \int_0^{2\pi} \tilde{z} \rho \, d\rho d\theta. \quad (\text{C.30})$$

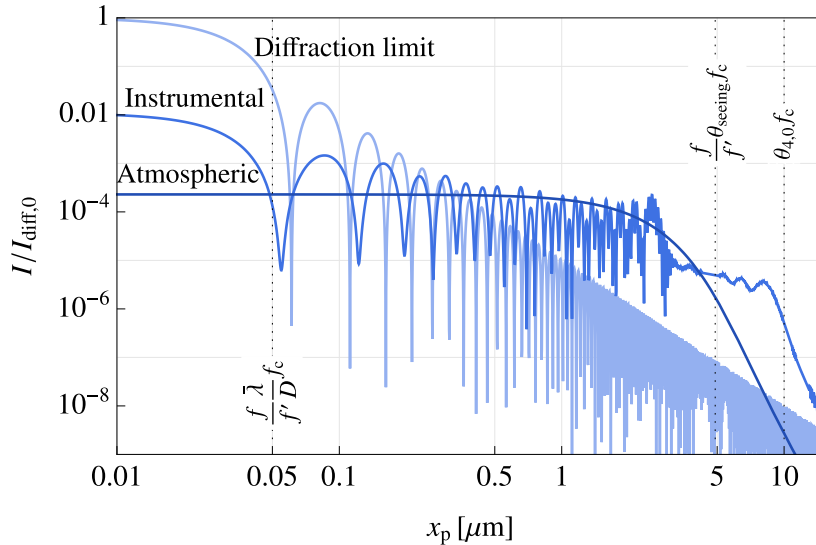


Figure 22: Intensity plotted as a function of the physical pixel coordinate, where we have normalized the intensities to the peak of the diffraction limited image. All curves correspond to the same total intensity. We have chosen a $D = 10$ m primary, $f/f' = 10$, $f_c = 100$ mm at $\lambda = 500$ nm. The lightest blue line corresponds to the diffraction limited image of a point source (Airy pattern), whose characteristic (magnified) diffraction limit $(f/f')(\lambda/D)f_c$ we have indicated with the leftmost vertical dotted line. The line labelled “Instrumental” corresponds to the produced image in a system with primary spherical aberration $\alpha'_4 = 50$. We have indicated the boundary of the region within which most of the intensity resides as $\theta_{4,0}f_c$, which agrees with the analytic estimate described in the main text, see e.g. C.29. The line titled “Atmospheric” is the time-averaged image of a point source after accounting for atmospheric fluctuations, as described by eq. C.31. We have chosen a Fried parameter $r_0 = 10$ cm, which corresponds to a 1 arcsec seeing disk at 500 nm, which we have indicated with the middlemost dotted line. The Maréchal criterion for a diffraction limited system imposes that the maximum intensity of the distorted image (normalized to the diffraction limited peak) be ≥ 0.8 , which shows how much more distortion EPIC can tolerate.

with the instrumental aberrations discussed above, the seeing disk should fit within each pixel.

Following the modeling of atmospheric fluctuations based on Kolmogorov turbulence, the intensity on the focal plane over long timescales is given by [207]

$$I(\boldsymbol{\theta}_F) \propto \int d^2x e^{-ik\boldsymbol{\theta}_F \cdot \mathbf{x}} e^{-3.44 \left(\frac{f}{f'} \frac{|\mathbf{x}|}{r_0} \right)^{5/3}}, \quad (\text{C.31})$$

where r_0 is the Fried parameter. The FWHM of the seeing disk is found to be $\theta_{\text{seeing}} \sim 0.98\lambda/r_0$, which is given by eq. 2.63. Here the seeing angle is magnified at the plane of the photodetector by f/f' . The Fried parameter $r_0 \sim 10 - 20$ cm, which corresponds to a (unmagnified) seeing disk of $\sim 0.5 - 1$ arcsec for blue light. We plot the radial profile in figure 22, to compare it with the spread due to instrumental aberrations. In particular, the size of the magnified seeing disk is the same as that of an image with primary spherical aberration for $\alpha'_4 \sim 25$.

C.4 Dispersive element

In this section we fill in the details of the calculation presented in section 3.4, concerning the reduction of fringe contrast for large telescopes, large pixels and fast photodetectors. We stress that the presence of aberrations, instrumental or atmospheric, do not modify this effect. We thus study a diffraction limited system here for clarity.

The analysis here is one-dimensional and the optical configuration consists of a grating of size Nd_g , a camera lens of focal length f_c at a distance z_1 from the grating, and a photodetector array at the focal plane of the lens. A plane monochromatic wave incident on the grating has a profile at the focal plane given by

$$E_k(\theta_F, t) \propto A_k e^{ik(f_c+z_1-ct)} \exp \left[ik \frac{x_F^2}{f_c + z_1} \right] \frac{\sin(k\theta_F \frac{Nd}{2})}{\sin(k\theta_F \frac{d}{2})} \frac{\sin(k\frac{s}{2}\theta_F)}{k\frac{s}{2}\theta_F} e^{-ikct}, \quad (\text{C.32})$$

where $\theta_F \equiv x_F/f_c$ is the ratio of the physical distance on the pixel plane over the camera focal length, d_g is the periodicity of the grating and s is the width of each slit. The factor $f_c + z_1$ is common for every wavelength and can be absorbed into a shift of the clock, so will be neglected below. Similarly, the quadratic in x_F term is a path difference for rays with different wavelengths due to being focused at different points. We will neglect this for now but will comment on it towards the end. These phase factors were neglected in section 3.4 for brevity.

We are concerned with the spatial distribution of different wavelengths within a pixel, which comes about from the term of the form $\sin(Ny)/\sin(y)$. We specialize to the pixel in whose center the focused wavenumber is $k = \bar{k}$. All other wavelengths within the pixel will have wavenumbers $k \equiv \bar{k} + \sigma \in [\bar{k} - \frac{\sigma_k}{2}, \bar{k} + \frac{\sigma_k}{2}]$, where $\sigma_k \sim \bar{k}/\mathcal{R} \ll \bar{k}$, \mathcal{R} being the required resolution. The first diffraction peak of the wavelength $\lambda = 2\pi/k$ occurs at $\theta_k = \frac{\lambda}{d_g}$. We can shift θ_F such that $\theta_F = \theta'_F - \frac{\bar{\lambda}}{d}$, bringing the pixel's center at $\theta'_F = 0$, where $\bar{\lambda}$ is focused at. Then $k\theta_F \frac{Nd_g}{2} = k\theta'_F \frac{Nd_g}{2} + \pi N \frac{k}{\bar{k}}$ and similarly for the denominator. Now within the pixel of interest $\theta'_F \in \left(-\frac{\bar{\lambda}}{2d_g\mathcal{R}}, \frac{\bar{\lambda}}{2d_g\mathcal{R}}\right)$, so that $k\theta'_F d_g \ll 1$ and we can approximate the denominator as $\sin\left(k\theta_F \frac{d_g}{2}\right) = -\sin\left(k\theta'_F \frac{d_g}{2} - \pi\right) = -\sin\left[k\theta'_F \frac{d_g}{2} + \pi\left(\frac{k}{\bar{k}} - 1\right)\right] \simeq -\left[k\theta'_F \frac{d_g}{2} + \pi\left(\frac{k}{\bar{k}} - 1\right)\right]$. Similarly the numerator is $-\sin\left[k\theta'_F \frac{Nd_g}{2} + \pi N\left(\frac{k}{\bar{k}} - 1\right)\right]$. As proven in the beginning of section C.3, the resulting profile is the image of the point source at the wavelength k , as if we had an aperture of size Nd_g without the grating. Dropping the prime on θ'_F from here on, we recover eq. 3.7:

$$E_k(\theta_F, t) \propto A_k \frac{\sin\left[k\theta_F \frac{Nd_g}{2} + \pi N\left(\frac{k}{\bar{k}} - 1\right)\right]}{k\theta_F \frac{Nd_g}{2} + \pi N\left(\frac{k}{\bar{k}} - 1\right)} e^{-ikct}. \quad (\text{3.7})$$

A straightforward calculation gives the numerator and denominator of the excess fractional

intensity correlation

$$\begin{aligned}
\mathcal{N} &\propto \left\langle \int dk \int dk' |A_k|^2 |A_{k'}|^2 e^{-i(k-k')ct} \right. \\
&\quad \times \int d\theta_F^{(1)} N \frac{\sin \left[k\theta_F^{(1)} \frac{Nd_g}{2} + \pi N \left(\frac{k}{k} - 1 \right) \right]}{k\theta_F^{(1)} \frac{Nd_g}{2} + \pi N \left(\frac{k}{k} - 1 \right)} N \frac{\sin \left[k'\theta_F^{(1)} \frac{Nd_g}{2} + \pi N \left(\frac{k'}{k} - 1 \right) \right]}{k'\theta_F^{(1)} \frac{Nd_g}{2} + \pi N \left(\frac{k'}{k} - 1 \right)} \\
&\quad \times \left. \int d\theta_F^{(2)} N \frac{\sin \left[k\theta_F^{(2)} \frac{Nd_g}{2} + \pi N \left(\frac{k}{k} - 1 \right) \right]}{k\theta_F^{(2)} \frac{Nd_g}{2} + \pi N \left(\frac{k}{k} - 1 \right)} N \frac{\sin \left[k'\theta_F^{(2)} \frac{Nd_g}{2} + \pi N \left(\frac{k'}{k} - 1 \right) \right]}{k'\theta_F^{(2)} \frac{Nd_g}{2} + \pi N \left(\frac{k'}{k} - 1 \right)} \right\rangle_{\sigma_t} \quad (\text{C.33}) \\
\mathcal{D} &\propto \left| \int d\theta_F \int dk \left| A_k \frac{\sin \left[k\theta_F \frac{Nd_g}{2} + \pi N \left(\frac{k}{k} - 1 \right) \right]}{k\theta_F \frac{Nd_g}{2} + \pi N \left(\frac{k}{k} - 1 \right)} \right|^2 \right|^2,
\end{aligned}$$

where $\mathcal{N} \equiv \langle I_1 I_2 \rangle - \langle I_1 \rangle \langle I_2 \rangle$ and $\mathcal{D} \equiv \langle I_1 \rangle \langle I_2 \rangle$, as in eqs. 3.8 and 3.9, and $\langle \dots \rangle_{\sigma_t}$ denotes averaging over time with a normalized gaussian kernel of standard deviation σ_t . We emphasize that the terms involving the focal plane of each telescope, $\theta_F^{(i)}$, $i = 1, 2$ contain *different* wavenumber k and k' in the numerator. Consequently, if these are focused too far apart spatially, then this term averages out and fringe contrast can be lost.

There is no obstacle in evaluating these formulae numerically, but we can understand the source of the suppression better in the limit where the pixel is much larger than the width of these sinc functions (Airy patterns). Then we can take the integrations over $\theta_F^{(i)}$ to infinity in these expressions, which is a good approximation if there are several distinct ‘‘Airy patterns’’ within each pixel. We have also verified this fact numerically.

One can show that

$$\begin{aligned}
&\int_{-\infty}^{+\infty} d\theta_F^{(i)} N \frac{\sin \left[k\theta_F^{(i)} \frac{Nd_g}{2} + \pi N \left(\frac{k}{k} - 1 \right) \right]}{k\theta_F^{(i)} \frac{Nd_g}{2} + \pi N \left(\frac{k}{k} - 1 \right)} N \frac{\sin \left[k'\theta_F^{(i)} \frac{Nd_g}{2} + \pi N \left(\frac{k'}{k} - 1 \right) \right]}{k'\theta_F^{(i)} \frac{Nd_g}{2} + \pi N \left(\frac{k'}{k} - 1 \right)} \\
&\quad \simeq \frac{2\pi N \sin \left(N\pi \frac{k-k'}{k} \right)}{\bar{k} d_g N\pi \frac{k-k'}{k}}. \quad (\text{C.34})
\end{aligned}$$

This should be contrasted to the term $\langle I_1 \rangle \langle I_2 \rangle$, which involves integrals of the same wavelengths at each telescope, in which case $\langle I_1 \rangle = \langle I_2 \rangle \propto 2\pi N / \bar{k} d_g$. Neglecting this prefactor, we have

$$\mathcal{N} \propto \left\langle \int dk \int dk' |A_k|^2 |A_{k'}|^2 e^{-i(k-k')ct} \left[\frac{\sin \left(N\pi \frac{k-k'}{k} \right)}{N\pi \frac{k-k'}{k}} \right]^2 \right\rangle_{\sigma_t}. \quad (\text{C.35})$$

This shows where the ‘‘sinc-squared filter’’ we encountered in eq. 3.10 stems from. It restricts the integral only to those wavenumbers that are $\sim (N\pi)^{-1}$ close. Because $N \gg \mathcal{R}$ in order to accommodate optical aberrations but, most importantly, seeing fluctuations, this term, if uncorrected, will reduce the fringe contrast.

The starlight spectrum has a natural width σ_n and a peak at k_0 . By writing $|A_k|^2 = \frac{1}{\sqrt{2\pi}\sigma_n} \exp \left[-\frac{(k-k_0)^2}{2\sigma_n^2} \right]$, where $\sigma_n \sim k_0 \gg \sigma_k$, we can approximate within the integral $|A_k|^2 \simeq$

$|A_{\bar{k}}|^2$, which is a constant and can be dropped in ratios. We find:

$$\frac{N}{\mathcal{D}} \simeq \left\langle \int_{\bar{k}-\frac{\sigma_k}{2}}^{\bar{k}+\frac{\sigma_k}{2}} dk \int_{\bar{k}-\frac{\sigma_k}{2}}^{\bar{k}+\frac{\sigma_k}{2}} dk' e^{-i(k-k')ct} \left[\frac{\sin\left(N\pi\frac{k-k'}{k}\right)}{N\pi\frac{k-k'}{k}} \right]_{\sigma_t}^2 \right\rangle. \quad (\text{C.36})$$

In the limit of no dispersion (such as in the case where we used a filter of bandwidth $\sim \bar{k}/\mathcal{R}$ instead), this becomes

$$\left\langle \int_{\bar{k}-\frac{\sigma_k}{2}}^{\bar{k}+\frac{\sigma_k}{2}} dk \int_{\bar{k}-\frac{\sigma_k}{2}}^{\bar{k}+\frac{\sigma_k}{2}} dk' e^{-i(k-k')ct} \right\rangle_{\sigma_t} = \frac{1}{c^2\sigma_t^2} \left[-2 + 2e^{-c^2\sigma_k^2\sigma_t^2/2} + \sqrt{2\pi}c\sigma_k\sigma_t \operatorname{erf}\left(\frac{c\sigma_k\sigma_t}{\sqrt{2}}\right) \right], \quad (\text{C.37})$$

which, in the limit $c\sigma_t \ll \sigma_k^{-1}$, along with the prefactor $\propto \sigma_n^{-2}$ of the $|A_k|^2$ terms, gives $\propto \left(\frac{\sigma_k}{\sigma_n}\right)^2 \frac{1}{c\sigma_k\sigma_t}$. The first quadratic term is a suppression coming from taking only part of the total spectrum within the pixel, and the second term is the usual suppression due to a finite time-resolution. This is the standard result used throughout section 2.

The integral in the presence of dispersion cannot be calculated analytically, but we can bring it in a form that is more transparent. We define the function $h(\sigma) = e^{-i\sigma ct} \left[\frac{\sin(\sigma/\sigma_d)}{\sigma/\sigma_d} \right]^2$, where we defined $\sigma_d \equiv \bar{k}/\pi N$ as the ‘‘diffraction limited’’ width. By changing variables to $\sigma \equiv k + k'$ and $\sigma' \equiv k - k'$, the double integral can be made one-dimensional

$$\begin{aligned} \left\langle \int_{\bar{k}-\frac{\sigma_k}{2}}^{\bar{k}+\frac{\sigma_k}{2}} dk \int_{\bar{k}-\frac{\sigma_k}{2}}^{\bar{k}+\frac{\sigma_k}{2}} dk' e^{-i(k-k')ct} \left[\frac{\sin\left(N\pi\frac{k-k'}{k}\right)}{N\pi\frac{k-k'}{k}} \right]_{\sigma_t}^2 \right\rangle &= \left\langle \int_0^{\sigma_k} d\sigma (\sigma_k - \sigma) [h(\sigma) + h(-\sigma)] \right\rangle_{\sigma_t} \\ &= 2 \int_0^{\sigma_k} d\sigma (\sigma_k - \sigma) e^{-\frac{c^2\sigma^2\sigma_t^2}{2}} \left[\frac{\sin(\sigma/\sigma_d)}{\sigma/\sigma_d} \right]^2, \end{aligned} \quad (\text{C.38})$$

which concludes the proof of eq. 3.10. This function is plotted in figure 12 for relevant parameters of the different proposed phases of EPIC interferometers. We refer the reader to section 3.4 for the implications of these results and for potential ways to alleviate the resulting suppression.

We have carried out the same calculation in the presence of a prism instead of a grating. The result remains the same as that of eq. C.33, with the only difference that the quantity N in the θ_F -independent term (the resolving power if the system was diffraction limited) is replaced by $N_{\text{prism}} \equiv b dn/d\lambda$, where b is the length of the base of the prism and $dn/d\lambda$ the derivative of the index of refraction with respect to the wavelength. The requirement of including the seeing angle within each pixel is the same as in eq. 3.11, but with $N \rightarrow N_{\text{prism}}$.

References

- [1] Ken Van Tilburg, Masha Baryakhtar, Marios Galanis, and Neal Weiner. Astrometry with Extended-Path Intensity Correlation. *arXiv e-prints*, page arXiv:2307.03221, July 2023.
- [2] Kailash C. Sahu et al. An Isolated Stellar-mass Black Hole Detected through Astrometric Microlensing. *Astrophys. J.*, 933(1):83, 2022.
- [3] Casey Y. Lam et al. An Isolated Mass-gap Black Hole or Neutron Star Detected with Astrometric Microlensing. *ApJ*, 933(1):L23, July 2022.

- [4] Przemek Mróz, Andrzej Udalski, and Andrew Gould. Systematic Errors as a Source of Mass Discrepancy in Black Hole Microlensing Event OGLE-2011-BLG-0462. *ApJ*, 937(2):L24, October 2022.
- [5] Gaia Collaboration. Gaia Data Release 3: Stellar multiplicity, a teaser for the hidden treasure. *arXiv e-prints*, page arXiv:2206.05595, June 2022.
- [6] Ana Bonaca, David W. Hogg, Adrian M. Price-Whelan, and Charlie Conroy. The Spur and the Gap in GD-1: Dynamical evidence for a dark substructure in the Milky Way halo. *The Astrophysical Journal*, 11 2019.
- [7] Lina Necib, Bryan Ostdiek, Mariangela Lisanti, Timothy Cohen, Marat Freytsis, and Shea Garrison-Kimmel. Chasing Accreted Structures within Gaia DR2 using Deep Learning. *Astrophys. J.*, 903(1):25, 2020.
- [8] Amina Helmi. Streams, Substructures, and the Early History of the Milky Way. *ARA&A*, 58:205–256, August 2020.
- [9] Amina Helmi. Streams, Substructures, and the Early History of the Milky Way. *Ann. Rev. Astron. Astrophys.*, 58(1):205–256, 2020.
- [10] John David Anderson, Michael SW Keeseey, Eunice L Lau, EM Standish Jr, and XX Newhall. Tests of general relativity using astrometric and radio metric observations of the planets. *Acta Astronautica*, 5(1-2):43–61, 1978.
- [11] E Fomalont, S Kopeikin, G Lanyi, and J Benson. Progress in measurements of the gravitational bending of radio waves using the vlba. *The Astrophysical Journal*, 699(2):1395, 2009.
- [12] Maria Teresa Crosta and F Mignard. Microarcsecond light bending by jupiter. *Classical and Quantum Gravity*, 23(15):4853, 2006.
- [13] GRAVITY Collaboration, R. Abuter, A. Amorim, M. Bauböck, J. P. Berger, H. Bonnet, W. Brandner, Y. Clénet, V. Coudé Du Foresto, P. T. de Zeeuw, C. Deen, J. Dexter, G. Duvert, A. Eckart, F. Eisenhauer, N. M. Förster Schreiber, P. Garcia, F. Gao, E. Gendron, R. Genzel, S. Gillessen, P. Guajardo, M. Habibi, X. Haubois, Th. Henning, S. Hippler, M. Horrobin, A. Huber, A. Jiménez-Rosales, L. Jocou, P. Kervella, S. Lacour, V. Lapeyrère, B. Lazareff, J. B. Le Bouquin, P. Léna, M. Lippa, T. Ott, J. Panduro, T. Paumard, K. Perraut, G. Perrin, O. Pfuhl, P. M. Plewa, S. Rabien, G. Rodríguez-Coira, G. Rousset, A. Sternberg, O. Straub, C. Straubmeier, E. Sturm, L. J. Tacconi, F. Vincent, S. von Fellenberg, I. Waisberg, F. Widmann, E. Wieprecht, E. Wieszorrek, J. Woillez, and S. Yazici. Detection of orbital motions near the last stable circular orbit of the massive black hole SgrA*. *A&A*, 618:L10, October 2018.
- [14] Ken Van Tilburg, Anna-Maria Taki, and Neal Weiner. Halometry from astrometry. *Journal of Cosmology and Astroparticle Physics*, 2018(07):041, 2018.
- [15] Malte Buschmann, Benjamin R Safdi, and Katelin Schutz. Galactic potential and dark matter density from angular stellar accelerations. *Physical review letters*, 127(24):241104, 2021.
- [16] Cristina Mondino, Anna-Maria Taki, Ken Van Tilburg, and Neal Weiner. First Results on Dark Matter Substructure from Astrometric Weak Lensing. *Phys. Rev. Lett.*, 125(11):111101, 2020.
- [17] Ted Pyne, Carl R Gwinn, Mark Birkinshaw, T Marshall Eubanks, and Demetrios N Matsakis. Gravitational radiation and very long baseline interferometry. *arXiv preprint astro-ph/9507030*, 1995.
- [18] Laura G Book and Eanna E Flanagan. Astrometric effects of a stochastic gravitational wave background. *Physical Review D*, 83(2):024024, 2011.

- [19] Sergei A Klioner. Gaia-like astrometry and gravitational waves. *Classical and Quantum Gravity*, 35(4):045005, 2018.
- [20] Christopher J Moore, Deyan P Mihaylov, Anthony Lasenby, and Gerard Gilmore. Astrometric search method for individually resolvable gravitational wave sources with gaia. *Physical Review Letters*, 119(26):261102, 2017.
- [21] E. Høg, C. Fabricius, V. V. Makarov, S. Urban, T. Corbin, G. Wycoff, U. Bastian, P. Schwekendiek, and A. Wicenec. The Tycho-2 catalogue of the 2.5 million brightest stars. *A&A*, 355:L27–L30, March 2000.
- [22] Timo Prusti, JHJ De Bruijne, Anthony GA Brown, Antonella Vallenari, C Babusiaux, CAL Bailer-Jones, U Bastian, M Biermann, Dafydd Wyn Evans, L Eyer, et al. The gaia mission. *Astronomy & astrophysics*, 595:A1, 2016.
- [23] A. Bradley, L. Abramowicz-Reed, D. Story, G. Benedict, and W. Jefferys. The Flight Hardware and Ground System for Hubble Space Telescope Astrometry. *PASP*, 103:317, March 1991.
- [24] Jonathan P. Gardner, John C. Mather, Mark Clampin, Rene Doyon, Matthew A. Greenhouse, Heidi B. Hammel, John B. Hutchings, Peter Jakobsen, Simon J. Lilly, Knox S. Long, Jonathan I. Lunine, Mark J. McCaughrean, Matt Mountain, John Nella, George H. Rieke, Marcia J. Rieke, Hans-Walter Rix, Eric P. Smith, George Sonneborn, Massimo Stiavelli, H. S. Stockman, Rogier A. Windhorst, and Gillian S. Wright. The James Webb Space Telescope. *Space Sci. Rev.*, 123(4):485–606, April 2006.
- [25] Roberto Abuter, Matteo Accardo, A Amorim, N Anugu, Gerardo Avila, N Azouaoui, Myriam Benisty, Jean-Philippe Berger, Nicolas Blind, Henri Bonnet, et al. First light for gravity: Phase referencing optical interferometry for the very large telescope interferometer. *Astronomy & Astrophysics*, 602:A94, 2017.
- [26] T. A. ten Brummelaar, H. A. McAlister, S. T. Ridgway, Jr. Bagnuolo, W. G., N. H. Turner, L. Sturmann, J. Sturmann, D. H. Berger, C. E. Ogden, R. Cadman, W. I. Hartkopf, C. H. Hopper, and M. A. Shure. First Results from the CHARA Array. II. A Description of the Instrument. *ApJ*, 628(1):453–465, July 2005.
- [27] Kazunori Akiyama et al. First M87 Event Horizon Telescope Results. I. The Shadow of the Supermassive Black Hole. *Astrophys. J. Lett.*, 875:L1, 2019.
- [28] Kazunori Akiyama et al. First M87 Event Horizon Telescope Results. II. Array and Instrumentation. *Astrophys. J. Lett.*, 875(1):L2, 2019.
- [29] M. Mark Colavita and Peter L. Wizinowich. Keck Interferometer update. In Wesley A. Traub, editor, *Interferometry for Optical Astronomy II*, volume 4838 of *Society of Photo-Optical Instrumentation Engineers (SPIE) Conference Series*, pages 79–88, February 2003.
- [30] R. Hanbury Brown and R. G. Twiss. A New type of interferometer for use in radio astronomy. *Philosophical Magazine*, 45(366):663–682, March 1954.
- [31] R. Hanbury Brown and R. Q. Twiss. Correlation between Photons in two Coherent Beams of Light. *Nature*, 177(4497):27–29, January 1956.
- [32] R. Hanbury Brown. A Test of a New Type of Stellar Interferometer on Sirius. *Nature*, 178(4541):1046–1048, November 1956.
- [33] R Hanbury Brown and Richard Quinton Twiss. Interferometry of the intensity fluctuations in light-i. basic theory: the correlation between photons in coherent beams of radiation. *Proceedings of the Royal Society of London. Series A. Mathematical and Physical Sciences*, 242(1230):300–324, 1957.
- [34] R Hanbury Brown and RQ Twiss. Interferometry of the intensity fluctuations in light. ii. an

experimental test of the theory for partially coherent light. *Proceedings of the Royal Society of London. Series A. Mathematical and Physical Sciences*, 243(1234):291–319, 1958.

- [35] R Hanbury Brown and RQ Twiss. Interferometry of the intensity fluctuations in light iii. applications to astronomy. *Proceedings of the Royal Society of London. Series A. Mathematical and Physical Sciences*, 248(1253):199–221, 1958.
- [36] R. Hanbury Brown and R. Q. Twiss. Interferometry of the Intensity Fluctuations in Light. IV. A Test of an Intensity Interferometer on Sirius A. *Proceedings of the Royal Society of London Series A*, 248(1253):222–237, November 1958.
- [37] R. Hanbury Brown, J. Davis, and L. R. Allen. The stellar interferometer at Narrabri Observatory I. A. description of the instrument and the observational procedure. *MNRAS*, 137:375, January 1967.
- [38] R. Hanbury Brown, J. Davis, L. R. Allen, and J. M. Rome. The stellar interferometer at Narrabri Observatory-II. The angular diameters of 15 stars. *MNRAS*, 137:393, January 1967.
- [39] R. Hanbury Brown. *The intensity interferometer; its application to astronomy*. London, Taylor & Francis; New York, Halsted Press, 1974.
- [40] R. Hanbury Brown, J. Davis, and L. R. Allen. The Angular Diameters of 32 Stars. *MNRAS*, 167:121–136, April 1974.
- [41] A. D. Code, J. Davis, R. C. Bless, and R. H. Brown. Empirical effective temperatures and bolometric corrections for early-type stars. *ApJ*, 203:417–434, January 1976.
- [42] D. Herbison-Evans, R. Hanbury Brown, J. Davis, and L. R. Allen. A study of alpha Virginis with an intensity interferometer. *MNRAS*, 151:161, 1971.
- [43] TC Weekes, H Badran, SD Biller, I Bond, S Bradbury, J Buckley, D Carter-Lewis, M Catanese, S Criswell, W Cui, et al. Veritas: the very energetic radiation imaging telescope array system. *Astroparticle Physics*, 17(2):221–243, 2002.
- [44] James Anthony Hinton, Hess Collaboration, et al. The status of the hess project. *New Astronomy Reviews*, 48(5-6):331–337, 2004.
- [45] C Baixeras, D Bastieri, C Bigongiari, O Blanch, G Blanchot, R Bock, T Bretz, A Chilingarian, JA Coarasa, E Colombo, et al. Commissioning and first tests of the magic telescope. *Nuclear Instruments and Methods in Physics Research Section A: Accelerators, Spectrometers, Detectors and Associated Equipment*, 518(1-2):188–192, 2004.
- [46] H Anderhub, Michael Backes, A Biland, Vittorio Boccone, Isabel Braun, Thomas Bretz, J Buß, Franck Cadoux, V Commichau, L Djambazov, et al. Design and operation of fact—the first g-apd cherenkov telescope. *Journal of Instrumentation*, 8(06):P06008, 2013.
- [47] CTA Consortium J. Knapp@ leeds. ac. uk <http://www.cta-observatory.org>, M Actis, G Agnetta, F Aharonian, A Akhperjanian, J Aleksić, E Aliu, D Allan, I Allekotte, F Antico, et al. Design concepts for the cherenkov telescope array cta: an advanced facility for ground-based high-energy gamma-ray astronomy. *Experimental Astronomy*, 32:193–316, 2011.
- [48] Paul D Nuñez, Richard Holmes, David Kieda, Janvida Rou, and Stephan LeBohec. Imaging submilliarcsecond stellar features with intensity interferometry using air cherenkov telescope arrays. *Monthly Notices of the Royal Astronomical Society*, 424(2):1006–1011, 2012.
- [49] D. Kieda, Monica Acosta, Anastasia Barbano, Colin Carlile, Michael Daniel, Dainis Dravins, Jamie Holder, Nolan Matthews, Teresa Montaruli, Roland Walter, and Luca Zampieri. Science opportunities enabled by the era of Visible Band Stellar Imaging with sub-100 μ arc-sec angular resolution. *arXiv e-prints*, page arXiv:1908.03164, August 2019.
- [50] Sascha Trippe, Jae-Young Kim, Bangwon Lee, Changsu Choi, Junghwan Oh, Taeseok Lee, Sung-Chul Yoon, Myungshin Im, and Yong-Sun Park. Optical Multi-Channel Intensity

Interferometry - Or: How to Resolve O-Stars in the Magellanic Clouds. *Journal of Korean Astronomical Society*, 47(6):235–253, December 2014.

- [51] Paul D Nunez and A Domiciano de Souza. Capabilities of future intensity interferometers for observing fast-rotating stars: imaging with two-and three-telescope correlations. *Monthly Notices of the Royal Astronomical Society*, 453(2):1999–2005, 2015.
- [52] Dainis Dravins. Intensity interferometry: optical imaging with kilometer baselines. In *Optical and Infrared Interferometry and Imaging V*, volume 9907, pages 128–139. SPIE, 2016.
- [53] N Matthews and S LeBohec. Astrophysical measurements with the veritas stellar intensity interferometer. *arXiv preprint arXiv:1908.03587*, 2019.
- [54] AU Abeysekera, W Benbow, A Brill, JH Buckley, JL Christiansen, AJ Chromey, MK Daniel, J Davis, A Falcone, Q Feng, et al. Demonstration of stellar intensity interferometry with the four veritas telescopes. *Nature Astronomy*, 4(12):1164–1169, 2020.
- [55] David Kieda, Jonathan Davis, Tugdual LeBohec, Mike Lisa, and Nolan K Matthews. The veritas-stellar intensity interferometry (vsii) survey of stellar diameters. *arXiv preprint arXiv:2108.09774*, 2021.
- [56] Luca Zampieri, Giampiero Naletto, Aleksandr Burtovoi, Michele Fiori, and Cesare Barbieri. Stellar intensity interferometry of vega in photon counting mode. *Monthly Notices of the Royal Astronomical Society*, 506(2):1585–1594, 2021.
- [57] Dainis Dravins, Stephan LeBohec, Hannes Jensen, and Paul D. Nuñez. Stellar intensity interferometry: Prospects for sub-milliarcsecond optical imaging. *New A Rev.*, 56(5):143–167, November 2012.
- [58] Elliott P Horch, Samuel A Weiss, Paul M Klaucke, Richard A Pellegrino, and Justin D Rupert. Observations with the southern connecticut stellar interferometer. i. instrument description and first results. *The Astronomical Journal*, 163(2):92, 2022.
- [59] W. Guerin, J. P. Rivet, M. Fouché, G. Labeyrie, D. Vernet, F. Vakili, and R. Kaiser. Spatial intensity interferometry on three bright stars. *MNRAS*, 480(1):245–250, October 2018.
- [60] Paul Stankus, Andrei Nomerotski, Anže Slosar, and Stephen Vintskevich. Two-photon amplitude interferometry for precision astrometry. 10 2020.
- [61] Zhi Chen, Andrei Nomerotski, Anže Slosar, Paul Stankus, and Stephen Vintskevich. Astrometry in two-photon interferometry using an Earth rotation fringe scan. *Phys. Rev. D*, 107(2):023015, 2023.
- [62] Massimo Tinto and Sanjeev V Dhurandhar. Time-delay interferometry. *Living Reviews in Relativity*, 17:1–54, 2014.
- [63] James D Franson. Bell inequality for position and time. *Physical review letters*, 62(19):2205, 1989.
- [64] Gordon Baym. The physics of hanbury brown–twiss intensity interferometry: from stars to nuclear collisions. 1998.
- [65] Leonard Mandel and Emil Wolf. *Optical coherence and quantum optics*. Cambridge university press, 1995.
- [66] Antoine Labeyrie, Stephen G Lipson, and Peter Nisenson. *An introduction to optical stellar interferometry*. Cambridge University Press, 2006.
- [67] Sebastian Karl, Andreas Zmija, Stefan Richter, Naomi Vogel, Dmitry Malyshev, Adrian Zink, Thilo Michel, Gisela Anton, Joachim von Zanthier, and Stefan Funk. Comparing different approaches for stellar intensity interferometry. *Monthly Notices of the Royal Astronomical Society*, 512(2):1722–1729, 2022.

- [68] Manuel Bojer, Zixin Huang, Sebastian Karl, Stefan Richter, Pieter Kok, and Joachim von Zanthier. A quantitative comparison of amplitude versus intensity interferometry for astronomy. *New Journal of Physics*, 24(4):043026, 2022.
- [69] GRAVITY Collaboration, R. Abuter, M. Accardo, A. Amorim, N. Anugu, G. Ávila, N. Azouaoui, M. Benisty, J. P. Berger, N. Blind, H. Bonnet, P. Bourget, W. Brandner, R. Brast, A. Buron, L. Burtscher, F. Cassaing, F. Chapron, É. Choquet, Y. Clénet, C. Collin, V. Coudé Du Foresto, W. de Wit, P. T. de Zeeuw, C. Deen, F. Delplancke-Ströbele, R. Dembet, F. Derie, J. Dexter, G. Duvert, M. Ebert, A. Eckart, F. Eisenhauer, M. Esselborn, P. Fédou, G. Finger, P. Garcia, C. E. Garcia Dabo, R. Garcia Lopez, E. Gendron, R. Genzel, S. Gillessen, F. Gonte, P. Gordo, M. Grould, U. Grözinger, S. Guieu, P. Haguenaue, O. Hans, X. Haubois, M. Haug, F. Haussmann, Th. Henning, S. Hippler, M. Horrobin, A. Huber, Z. Hubert, N. Hubin, C. A. Hummel, G. Jakob, A. Janssen, L. Jochum, L. Jocou, A. Kaufer, S. Kellner, S. Kendrew, L. Kern, P. Kervella, M. Kiekebusch, R. Klein, Y. Kok, J. Kolb, M. Kulas, S. Lacour, V. Lapeyrère, B. Lazareff, J. B. Le Bouquin, P. Lèna, R. Lenzen, S. Lévêque, M. Lippa, Y. Magnard, L. Mehrgan, M. Mellein, A. Mérand, J. Moreno-Ventas, T. Moulin, E. Müller, F. Müller, U. Neumann, S. Oberti, T. Ott, L. Pallanca, J. Panduro, L. Pasquini, T. Paumard, I. Percheron, K. Perraut, G. Perrin, A. Pflüger, O. Pfuhl, T. Phan Duc, P. M. Plewa, D. Popovic, S. Rabien, A. Ramírez, J. Ramos, C. Rau, M. Riquelme, R. R. Rohloff, G. Rousset, J. Sanchez-Bermudez, S. Scheithauer, M. Schöller, N. Schuhler, J. Spyromilio, C. Straubmeier, E. Sturm, M. Suarez, K. R. W. Tristram, N. Ventura, F. Vincent, I. Waisberg, I. Wank, J. Weber, E. Wieprecht, M. Wiest, E. Wiezorrek, M. Wittkowski, J. Woillez, B. Wolff, S. Yazici, D. Ziegler, and G. Zins. First light for GRAVITY: Phase referencing optical interferometry for the Very Large Telescope Interferometer. *A&A*, 602:A94, June 2017.
- [70] N. I. Shakura and R. A. Sunyaev. Black holes in binary systems. Observational appearance. *A&A*, 24:337–355, January 1973.
- [71] Nolan Matthews, Jean-Pierre Rivet, Mathilde Hugbart, Guillaume Labeyrie, Robin Kaiser, Olivier Lai, Farrokh Vakili, David Vernet, Julien Chabé, Clément Courde, Nicolas Schuhler, Pierre Bourget, and William Guerin. Intensity interferometry at Calern and beyond: progress report. In Antoine Mérand, Stephanie Sallum, and Joel Sanchez-Bermudez, editors, *Optical and Infrared Interferometry and Imaging VIII*, volume 12183 of *Society of Photo-Optical Instrumentation Engineers (SPIE) Conference Series*, page 121830G, August 2022.
- [72] VB Mendes and Erricos C Pavlis. High-accuracy zenith delay prediction at optical wavelengths. *Geophysical research letters*, 31(14), 2004.
- [73] GC Hulley and Erricos C Pavlis. A ray-tracing technique for improving satellite laser ranging atmospheric delay corrections, including the effects of horizontal refractivity gradients. *Journal of Geophysical Research: Solid Earth*, 112(B6), 2007.
- [74] Benjamin K Stuhl. Atmospheric refraction corrections in ground-to-satellite optical time transfer. *Optics Express*, 29(9):13706–13714, 2021.
- [75] A Kolmogorov. Classic papers on statistical theory, friedlander s., topper l, 1961.
- [76] The effects of the turbulent atmosphere on wave propagation. *Jerusalem: Israel Program for Scientific Translations*, 1971, 1971.
- [77] F. Roddier. The effects of atmospheric turbulence in optical astronomy. *Progress in Optics*, 19:281–376, January 1981.
- [78] Changhui Rao, Wenhan Jiang, and Ning Ling. Spatial and temporal characterization of phase fluctuations in non-Kolmogorov atmospheric turbulence. *Journal of Modern Optics*, 47(6):1111–1126, June 2000.
- [79] MG Miller and PL Zieske. Turbulence environment characterization. Technical report, AVCO EVERETT RESEARCH LAB INC EVERETT MA, 1979.

- [80] David L Fried. Anisoplanatism in adaptive optics. *JOSA*, 72(1):52–61, 1982.
- [81] Frederick G Smith. Atmospheric propagation of radiation. *The infrared and electro-optical systems handbook-IR/EO systems handbook*, 1993.
- [82] W Gao, Seung-Woo Kim, H Bosse, H Haitjema, YL Chen, XD Lu, W Knapp, A Weckenmann, WT Estler, and H Kunzmann. Measurement technologies for precision positioning. *CIRP annals*, 64(2):773–796, 2015.
- [83] Yuki Shimizu, Liang-Chia Chen, Dae Wook Kim, Xiuguo Chen, Xinghui Li, and Hiraku Matsukuma. An insight into optical metrology in manufacturing. *Measurement Science and Technology*, 32(4):042003, April 2021.
- [84] Vanessa P. Bailey, Philip M. Hinz, Alfio T. Puglisi, Simone Esposito, Vidhya Vaitheeswaran, Andrew J. Skemer, Denis Defrère, Amali Vaz, and Jarron M. Leisenring. Large binocular telescope interferometer adaptive optics: on-sky performance and lessons learned. In Enrico Marchetti, Laird M. Close, and Jean-Pierre Vran, editors, *Adaptive Optics Systems IV*, volume 9148 of *Society of Photo-Optical Instrumentation Engineers (SPIE) Conference Series*, page 914803, July 2014.
- [85] P. Wizinowich, J. Chin, C. Correia, J. Lu, T. Brown, K. Casey, S. Cetre, J.-R. Delorme, L. Gers, L. Hunter, S. Lilley, S. Ragland, A. Surendran, E. Wetherell, A. Ghez, T. Do, T. Jones, M. Liu, D. Mawet, C. Max, M. Morris, T. Treu, and S. Wright. Keck all sky precision adaptive optics. In Laura Schreiber, Dirk Schmidt, and Elise Vernet, editors, *Adaptive Optics Systems VII*, volume 11448, page 114480E. International Society for Optics and Photonics, SPIE, 2020.
- [86] MA Holdaway and Tamara T Helfer. Interferometric array design. In *Synthesis Imaging in Radio Astronomy II*, volume 180, page 537, 1999.
- [87] Eric Keto. The shapes of cross-correlation interferometers. *The Astrophysical Journal*, 475(2):843, 1997.
- [88] Marcel JE Golay. Point arrays having compact, nonredundant autocorrelations. *JOSA*, 61(2):272–273, 1971.
- [89] L Kogan. Optimization of an array configuration minimizing side lobes. *MMA Memo*, 171, 1997.
- [90] F Boone. Interferometric array design: Distributions of fourier samples for imaging. *Astronomy & Astrophysics*, 386(3):1160–1171, 2002.
- [91] Lennart Lindegren, SA Klioner, J Hernández, A Bombrun, M Ramos-Lerate, Hea Steidelmüller, U Bastian, M Biermann, A de Torres, E Gerlach, et al. Gaia early data release 3-the astrometric solution. *Astronomy & Astrophysics*, 649:A2, 2021.
- [92] Stephan Steinhauer, Samuel Gyger, and Val Zwiller. Progress on large-scale superconducting nanowire single-photon detectors. *Applied Physics Letters*, 118(10):100501, 2021.
- [93] Robert H. Hadfield. Superfast photon counting. *Nature Photonics*, 14(4):201–202, 2020.
- [94] Boris Korzh, Qing-Yuan Zhao, Jason P Allmaras, Simone Frasca, Travis M Autry, Eric A Bersin, Andrew D Beyer, Ryan M Briggs, Bruce Bumble, Marco Colangelo, et al. Demonstration of sub-3 ps temporal resolution with a superconducting nanowire single-photon detector. *Nature Photonics*, 14(4):250–255, 2020.
- [95] E. E. Wollman, V. B. Verma, A. D. Beyer, R. M. Briggs, B. Korzh, J. P. Allmaras, F. Marsili, A. E. Lita, R. P. Mirin, S. W. Nam, and M. D. Shaw. Uv superconducting nanowire single-photon detectors with high efficiency, low noise, and 4 k operating temperature. *Opt. Express*, 25(22):26792–26801, Oct 2017.
- [96] Lixing You, Xiaoyan Yang, Yuhao He, Wenxing Zhang, Dengkuan Liu, Weijun Zhang, Lu Zhang, Ling Zhang, Xiaoyu Liu, Sijing Chen, Zhen Wang, and Xiaoming Xie. Jitter

- analysis of a superconducting nanowire single photon detector. *AIP Advances*, 3(7):072135, 2013.
- [97] Andrew S. Mueller, Boris Korzh, Marcus Runyan, Emma E. Wollman, Andrew D. Beyer, Jason P. Allmaras, Angel E. Velasco, Ioana Craiciu, Bruce Bumble, Ryan M. Briggs, Lautaro Narvaez, Cristián Peña, Maria Spiropulu, and Matthew D. Shaw. Free-space coupled superconducting nanowire single-photon detector with low dark counts. *Optica*, 8(12):1586–1587, Dec 2021.
- [98] Dileep V. Reddy, Robert R. Nerem, Sae Woo Nam, Richard P. Mirin, and Varun B. Verma. Superconducting nanowire single-photon detectors with 98% system detection efficiency at 1550 nm. *Optica*, 7(12):1649–1653, Dec 2020.
- [99] Emma E. Wollman, Varun B. Verma, Adriana E. Lita, William H. Farr, Matthew D. Shaw, Richard P. Mirin, and Sae Woo Nam. Kilopixel array of superconducting nanowire single-photon detectors. *Opt. Express*, 27(24):35279–35289, Nov 2019.
- [100] Jason P. Allmaras, Emma E. Wollman, Andrew D. Beyer, Ryan M. Briggs, Boris A. Korzh, Bruce Bumble, and Matthew D. Shaw. Demonstration of a thermally coupled row-column snspd imaging array. *Nano Letters*, 20(3):2163–2168, 2020. PMID: 32091221.
- [101] Qing-Yuan Zhao, Di Zhu, Niccolò Calandri, Andrew E. Dane, Adam N. McCaughan, Francesco Bellei, Hao-Zhu Wang, Daniel F. Santavicca, and Karl K. Berggren. Single-photon imager based on a superconducting nanowire delay line. *Nature Photonics*, 11(4):247–251, 2017.
- [102] Emma E. Wollman, Varun B. Verma, Alexander B. Walter, Jeff Chiles, Boris Korzh, Jason P. Allmaras, Yao Zhai, Adriana E. Lita, Adam N. McCaughan, Ekkehart Schmidt, Simone Frasca, Richard P. Mirin, Sae-Woo Nam, and Matthew D. Shaw. Recent advances in superconducting nanowire single-photon detector technology for exoplanet transit spectroscopy in the mid-infrared. *Journal of Astronomical Telescopes, Instruments, and Systems*, 7(1):011004, 2021.
- [103] Cara Battersby, Lee Armus, Edwin Bergin, Tiffany Kataria, Margaret Meixner, Alexandra Pope, Kevin B. Stevenson, Asantha Cooray, David Leisawitz, Douglas Scott, James Bauer, C. Matt Bradford, Kimberly Ennico, Jonathan J. Fortney, Lisa Kaltenegger, Gary J. Melnick, Stefanie N. Milam, Desika Narayanan, Deborah Padgett, Klaus Pontoppidan, Thomas Roellig, Karin Sandstrom, Kate Y. L. Su, Joaquin Vieira, Edward Wright, Jonas Zmuidzinas, Johannes Staguhn, Kartik Sheth, Dominic Benford, Eric E. Mamajek, Susan G. Neff, Sean Carey, Denis Burgarella, Elvire De Beck, Maryvonne Gerin, Frank P. Helmich, S. Harvey Moseley, Itsuki Sakon, and Martina C. Wiedner. The origins space telescope. *Nature Astronomy*, 2(8):596–599, 2018.
- [104] Simone Tisa, Fabrizio Guerrieri, and Franco Zappa. Variable-load quenching circuit for single-photon avalanche diodes. *Opt. Express*, 16(3):2232–2244, Feb 2008.
- [105] Mirko Sanzaro, Paolo Gattari, Federica Villa, Alberto Tosi, Giuseppe Croce, and Franco Zappa. Single-photon avalanche diodes in a 0.16 μm bcd technology with sharp timing response and red-enhanced sensitivity. *IEEE Journal of Selected Topics in Quantum Electronics*, 24(2):1–9, 2018.
- [106] Wolfgang Becker, Francesco Gramuglia, Ming-Lo Wu, Edoardo Charbon, and Claudio Bruschini. 8.7 ps fwhm irf width from ultrafast spad. <https://www.becker-hickl.com/literature/application-notes/8-7-ps-fwhm-irf-width-from-ultrafast-spada/>, 2022. [Online; accessed 06-Apr-2023].
- [107] Brian F. Aull, Erik K. Duerr, Jonathan P. Frechette, K. Alexander McIntosh, Daniel R. Schuette, and Richard D. Younger. Large-format geiger-mode avalanche photodiode arrays and readout circuits. *IEEE Journal of Selected Topics in Quantum Electronics*, 24(2):1–10, 2018.

- [108] Meera Punjija, Kevin Ryu, Brian Aull, K. Alexander McIntosh, Kevan Donlon, Mike Brattain, Hermanus Pretorius, Denis Nothern, Noah Pestana, Thomas Karolyshyn, Jorgo Mihallari, Zachary Kranefeld, Erik Duerr, Anup B. Katake, and Alejandro Miguel San Martin. A direct-detection LIDAR detector for the Europa lander concept. In Mark A. Itzler, Joshua C. Bienfang, and K. Alex McIntosh, editors, *Advanced Photon Counting Techniques XVI*, volume 12089, page 1208903. International Society for Optics and Photonics, SPIE, 2022.
- [109] Meera Punjija, Kevin Ryu, Matt Gregory, Alex McIntosh, Erik Duerr, and Anup Katake. Radiation-Hardened Sensors for the Final Descent Phase of Europa Lander. In *Advanced Technology for National Security Workshop (ATNS) 2021, Pasadena, California, April 6-8, 2021*. Pasadena, CA: Jet Propulsion Laboratory, National Aeronautics and Space Administration, 2021.
- [110] Kevin K. Ryu, Brian F. Aull, Michael Collins, Noah Pestana, Joseph Ciampi, Rabindra Das, Kevan Donlon, Hermanus Pretorius, Meera Punjija, Alex McIntosh, and Erik K Duerr. Geiger-mode avalanche photodiode arrays fabricated on SOI engineered-substrates. In Mark A. Itzler, Joshua C. Bienfang, and K. Alex McIntosh, editors, *Advanced Photon Counting Techniques XVI*, volume 12089, page 120890C. International Society for Optics and Photonics, SPIE, 2022.
- [111] Max Born, Emil Wolf, A. B. Bhatia, P. C. Clemmow, D. Gabor, A. R. Stokes, A. M. Taylor, P. A. Wayman, and W. L. Wilcock. *Principles of Optics: Electromagnetic Theory of Propagation, Interference and Diffraction of Light*. Cambridge University Press, 7 edition, 1999.
- [112] Pierre-Marie Gori, Farrokh Vakili, Jean-Pierre Rivet, William Guerin, Mathilde Hugbart, Andrea Chiavassa, Adrien Vakili, Robin Kaiser, and Guillaume Labeyrie. I3T: Intensity Interferometry Imaging Telescope. *MNRAS*, 505(2):2328–2335, August 2021.
- [113] N. Jovanovic, C. Schwab, N. Cvetojevic, O. Guyon, and F. Martinache. Enhancing Stellar Spectroscopy with Extreme Adaptive Optics and Photonics. *PASP*, 128(970):121001, December 2016.
- [114] Rüdiger Paschotta. *Encyclopedia of laser physics and technology*. John Wiley & Sons, 2008.
- [115] Pierre Bely. *The design and construction of large optical telescopes*. Springer, 2003.
- [116] Ed B. Fomalont. Astrometry and Geodesy. In G. B. Taylor, C. L. Carilli, and R. A. Perley, editors, *Synthesis Imaging in Radio Astronomy II*, volume 180 of *Astronomical Society of the Pacific Conference Series*, page 463, January 1999.
- [117] A Richard Thompson, James M Moran, and George W Swenson. *Interferometry and synthesis in radio astronomy*. Springer Nature, 2017.
- [118] Hayo Hase, Dirk Behrend, Chopo Ma, Bill Petrachenko, Harald Schuh, and Alan Whitney. The emerging vgos network of the ivs. In *IVS 2012 General Meeting Proceedings, NASA/CP-2012-217504*, pages 8–12, 2012.
- [119] Dirk Behrend, Bill Petrachenko, Chet Ruszczyk, and Pedro Elósegui. Roll-out status of the vgos network. In *poster, 24rd European VLBI group for geodesy and astrometry working meeting*, 2019.
- [120] A Niell, J Barrett, A Burns, R Cappallo, B Corey, M Derome, C Eckert, P Elosegui, R McWhirter, M Poirier, et al. Demonstration of a broadband very long baseline interferometer system: a new instrument for high-precision space geodesy. *Radio Science*, 53(10):1269–1291, 2018.
- [121] María J Rioja and Richard Dodson. Precise radio astrometry and new developments for the next generation of instruments. *The Astronomy and Astrophysics Review*, 28:1–79, 2020.
- [122] Microchip Technology Inc. Mhm-2020 active hydrogen maser.
<https://ww1.microchip.com/downloads/aemDocuments/documents/FTD/>

- [ProductDocuments/Brochures/MHM-2020-Active-Hydrogen-Maser-00003090.pdf](#), 2023. [Online; accessed 29-Jan-2023].
- [123] Quartzlock. Ch1-76a passive hydrogen maser. https://www.quartzlock.com/userfiles/downloads/datasheets/Passive_Hydrogen_Maser_CH1-76A.pdf, 2023. [Online; accessed 29-Jan-2023].
- [124] Microchip Technology Inc. 8040c rubidium frequency standard. <https://ww1.microchip.com/downloads/aemDocuments/documents/FTD/ProductDocuments/Brochures/00003047.pdf>, 2023. [Online; accessed 29-Jan-2023].
- [125] Astronic Corporation. 3352a series rubidium frequency standard. https://www.astronics.com/docs/default-source/Documents-ats/current-datasheets/rubidiums/3352a_0.pdf?sfvrsn=2, 2023. [Online; accessed 29-Jan-2023].
- [126] Microchip Technology Inc. 5071a primary frequency standard. <https://ww1.microchip.com/downloads/aemDocuments/documents/FTD/ProductDocuments/Brochures/5071A-Sell-Sheet-00002980.pdf>, 2023. [Online; accessed 29-Jan-2023].
- [127] Anthony G. A. Brown. Microarcsecond Astrometry: Science Highlights from Gaia. *ARA&A*, 59:59–115, September 2021.
- [128] Ken Van Tilburg and David E Kaplan. Discovering subsolar dark matter halos with astrometric weak lensing of multiply-imaged quasars. In preparation, 2023.
- [129] Rex A Saffer, James Liebert, and Edward W Olszewski. Discovery of a close detached binary da white dwarf system. *The Astrophysical Journal*, 334:947–957, 1988.
- [130] P Bergeron, F Wesemael, James Liebert, and G Fontaine. Determination of the atmospheric parameters of the binary da white dwarf 1870-2 (eg 11). *The Astrophysical Journal*, 345:L91–L94, 1989.
- [131] R Napiwotzki, CA Karl, T Lisker, S Catalán, H Drechsel, U Heber, D Homeier, D Koester, B Leibundgut, TR Marsh, et al. The eso supernovae type ia progenitor survey (spy)-the radial velocities of 643 da white dwarfs. *Astronomy & Astrophysics*, 638:A131, 2020.
- [132] PFL Maxted, TR Marsh, and CKJ Moran. Radial velocity measurements of white dwarfs. *Monthly Notices of the Royal Astronomical Society*, 319(1):305–317, 2000.
- [133] Jerry B Holberg, Terry D Oswalt, Edward M Sion, and George P McCook. The 25 parsec local white dwarf population. *Monthly Notices of the Royal Astronomical Society*, 462(3):2295–2318, 2016.
- [134] P Bergeron, P Dufour, G Fontaine, S Coutu, S Blouin, C Genest-Beaulieu, A Bédard, and B Rolland. On the measurement of fundamental parameters of white dwarfs in the gaia era. *The Astrophysical Journal*, 876(1):67, 2019.
- [135] Vedant Chandra, Hsiang-Chih Hwang, Nadia L Zakamska, and Sihao Cheng. A gravitational redshift measurement of the white dwarf mass–radius relation. *The Astrophysical Journal*, 899(2):146, 2020.
- [136] JA Panei, LG Althaus, and OG Benvenuto. Mass-radius relations for white dwarf stars of different internal compositions. *Astron. Astrophys*, 353:970–977, 2000.
- [137] F Pepe, Stefano Cristiani, R Rebolo, NC Santos, H Dekker, A Cabral, Paolo Di Marcantonio, P Figueira, G Lo Curto, C Lovis, et al. Espresso at vlt-on-sky performance and first results. *Astronomy & Astrophysics*, 645:A96, 2021.
- [138] Michael Perryman, Joel Hartman, Gáspár Á Bakos, and Lennart Lindegren. Astrometric exoplanet detection with gaia. *The Astrophysical Journal*, 797(1):14, 2014.

- [139] RL Akeson, X Chen, D Ciardi, M Crane, J Good, M Harbut, E Jackson, SR Kane, AC Laity, S Leifer, et al. The nasa exoplanet archive: data and tools for exoplanet research. *Publications of the Astronomical Society of the Pacific*, 125(930):989, 2013.
- [140] Wei Zhu and Subo Dong. Exoplanet statistics and theoretical implications. *Annual Review of Astronomy and Astrophysics*, 59:291–336, 2021.
- [141] D. L. Pollacco, I. Skillen, A. Collier Cameron, D. J. Christian, C. Hellier, J. Irwin, T. A. Lister, R. A. Street, R. G. West, D. R. Anderson, W. I. Clarkson, H. Deeg, B. Enoch, A. Evans, A. Fitzsimmons, C. A. Haswell, S. Hodgkin, K. Horne, S. R. Kane, F. P. Keenan, P. F. L. Maxted, A. J. Norton, J. Osborne, N. R. Parley, R. S. I. Ryans, B. Smalley, P. J. Wheatley, and D. M. Wilson. The WASP Project and the SuperWASP Cameras. *PASP*, 118(848):1407–1418, October 2006.
- [142] G. Bakos, R. W. Noyes, G. Kovács, K. Z. Stanek, D. D. Sasselov, and I. Domsa. Wide-Field Millimagnitude Photometry with the HAT: A Tool for Extrasolar Planet Detection. *PASP*, 116(817):266–277, March 2004.
- [143] William J Borucki, David Koch, Gibor Basri, Natalie Batalha, Timothy Brown, Douglas Caldwell, John Caldwell, Jørgen Christensen-Dalsgaard, William D Cochran, Edna DeVore, et al. Kepler planet-detection mission: introduction and first results. *Science*, 327(5968):977–980, 2010.
- [144] Debra A. Fischer, Guillem Anglada-Escude, Pamela Arriagada, Roman V. Baluev, Jacob L. Bean, Francois Bouchy, Lars A. Buchhave, Thorsten Carroll, Abhijit Chakraborty, Justin R. Crepp, Rebekah I. Dawson, Scott A. Diddams, Xavier Dumusque, Jason D. Eastman, Michael Endl, Pedro Figueira, Eric B. Ford, Daniel Foreman-Mackey, Paul Fournier, Gabor Fűrész, B. Scott Gaudi, Philip C. Gregory, Frank Grundahl, Artie P. Hatzes, Guillaume Hébrard, Enrique Herrero, David W. Hogg, Andrew W. Howard, John A. Johnson, Paul Jorden, Colby A. Jurgenson, David W. Latham, Greg Laughlin, Thomas J. Loredo, Christophe Lovis, Suvrath Mahadevan, Tyler M. McCracken, Francesco Pepe, Mario Perez, David F. Phillips, Peter P. Plavchan, Lisa Prato, Andreas Quirrenbach, Ansgar Reiners, Paul Robertson, Nuno C. Santos, David Sawyer, Damien Segransan, Alessandro Sozzetti, Tilo Steinmetz, Andrew Szentgyorgyi, Stéphane Udry, Jeff A. Valenti, Sharon X. Wang, Robert A. Wittenmyer, and Jason T. Wright. State of the Field: Extreme Precision Radial Velocities. *PASP*, 128(964):066001, June 2016.
- [145] Brendan P. Bowler. Imaging Extrasolar Giant Planets. *PASP*, 128(968):102001, October 2016.
- [146] Matthew T Penny, B Scott Gaudi, Eamonn Kerins, Nicholas J Rattenbury, Shude Mao, Annie C Robin, and Sebastiano Calchi Novati. Predictions of the wfirst microlensing survey. i. bound planet detection rates. *The Astrophysical Journal Supplement Series*, 241(1):3, 2019.
- [147] Anna-Christina Eilers, David W Hogg, Hans-Walter Rix, and Melissa K Ness. The circular velocity curve of the milky way from 5 to 25 kpc. *The Astrophysical Journal*, 871(1):120, 2019.
- [148] Konrad Kuijken and Gerard Gilmore. The mass distribution in the galactic disc—ii. determination of the surface mass density of the galactic disc near the sun. *Monthly Notices of the Royal Astronomical Society*, 239(2):605–649, 1989.
- [149] Johan Holmberg and Chris Flynn. The local density of matter mapped by hipparcos. *Monthly Notices of the Royal Astronomical Society*, 313(2):209–216, 2000.
- [150] Jo Bovy and Scott Tremaine. On the local dark matter density. *The Astrophysical Journal*, 756(1):89, 2012.
- [151] Katelin Schutz, Tongyan Lin, Benjamin R Safdi, and Chih-Liang Wu. Constraining a thin dark matter disk with g a i a. *Physical review letters*, 121(8):081101, 2018.
- [152] Axel Widmark. Measuring the local matter density using gaia dr2. *Astronomy & Astrophysics*, 623:A30, 2019.

- [153] Morgan Bennett and Jo Bovy. Vertical waves in the solar neighbourhood in gaia dr2. *Monthly Notices of the Royal Astronomical Society*, 482(1):1417–1425, 2019.
- [154] T Antoja, A Helmi, M Romero-Gómez, D Katz, C Babusiaux, Ronald Drimmel, DW Evans, F Figueras, Eloisa Poggio, C Reylé, et al. A dynamically young and perturbed milky way disk. *Nature*, 561(7723):360–362, 2018.
- [155] Amina Helmi, Carine Babusiaux, Helmer H Koppelman, Davide Massari, Jovan Veljanoski, and Anthony GA Brown. The merger that led to the formation of the milky way’s inner stellar halo and thick disk. *Nature*, 563(7729):85–88, 2018.
- [156] Aakash Ravi, Nicholas Langellier, David F Phillips, Malte Buschmann, Benjamin R Safdi, and Ronald L Walsworth. Probing dark matter using precision measurements of stellar accelerations. *Physical Review Letters*, 123(9):091101, 2019.
- [157] Hamish Silverwood and Richard Easther. Stellar accelerations and the galactic gravitational field. *Publications of the Astronomical Society of Australia*, 36, 2019.
- [158] Sukanya Chakrabarti, Jason Wright, Philip Chang, Alice Quillen, Peter Craig, Joey Territo, Elena D’Onghia, Kathryn V Johnston, Robert J De Rosa, Daniel Huber, et al. Toward a direct measure of the galactic acceleration. *The Astrophysical Journal Letters*, 902(1):L28, 2020.
- [159] David F Phillips, Aakash Ravi, Reza Ebadi, and Ronald L Walsworth. Milky way accelerometry via millisecond pulsar timing. *Physical Review Letters*, 126(14):141103, 2021.
- [160] Sukanya Chakrabarti, Philip Chang, Michael T Lam, Sarah J Vigeland, and Alice C Quillen. A measurement of the galactic plane mass density from binary pulsar accelerations. *The Astrophysical Journal Letters*, 907(2):L26, 2021.
- [161] Jo Bovy. A purely acceleration-based measurement of the fundamental galactic parameters. *arXiv preprint arXiv:2012.02169*, 2020.
- [162] Lars Hernquist. An Analytical Model for Spherical Galaxies and Bulges. *ApJ*, 356:359, June 1990.
- [163] Masanori Miyamoto and Ryuzaburo Nagai. Three-dimensional models for the distribution of mass in galaxies. *Publications of the Astronomical Society of Japan*, 27:533–543, 1975.
- [164] Julio F. Navarro, Carlos S. Frenk, and Simon D. M. White. The Structure of Cold Dark Matter Halos. *ApJ*, 462:563, May 1996.
- [165] B. Paczynski. Gravitational Microlensing by the Galactic Halo. *ApJ*, 304:1, May 1986.
- [166] E. Hog, I. D. Novikov, and A. G. Polnarev. MACHO photometry and astrometry. *A&A*, 294:287–294, February 1995.
- [167] M. Miyamoto and Y. Yoshii. Astrometry for Determining the MACHO Mass and Trajectory. *AJ*, 110:1427, September 1995.
- [168] Mark A. Walker. Microlensed Image Motions. *ApJ*, 453:37, November 1995.
- [169] B. Paczynski. Gravitational Microlensing of the Galactic Bulge Stars. *ApJ*, 371:L63, April 1991.
- [170] Kim Griest, Charles Alcock, Timothy S. Axelrod, David P. Bennett, Kem H. Cook, Kenneth C. Freeman, Hye-Sook Park, Saul Perlmutter, Bruce A. Peterson, Peter J. Quinn, Alexander W. Rodgers, Christopher W. Stubbs, and MACHO Collaboration. Gravitational Microlensing as a Method of Detecting Disk Dark Matter and Faint Disk Stars. *ApJ*, 372:L79, May 1991.
- [171] Shude Mao and Bohdan Paczynski. Gravitational Microlensing by Double Stars and Planetary Systems. *ApJ*, 374:L37, June 1991.

- [172] A. Udalski, M. Szymanski, J. Kaluzny, M. Kubiak, M. Mateo, W. Krzeminski, and B. Paczynski. The Optical Gravitational Lensing Experiment. The Early Warning System: Real Time Microlensing. *Acta Astron.*, 44:227–234, July 1994.
- [173] I. A. Bond, F. Abe, R. J. Dodd, J. B. Hearnshaw, M. Honda, J. Jugaku, P. M. Kilmartin, A. Marles, K. Masuda, Y. Matsubara, Y. Muraki, T. Nakamura, G. Nankivell, S. Noda, C. Noguchi, K. Ohnishi, N. J. Rattenbury, M. Reid, To. Saito, H. Sato, M. Sekiguchi, J. Skuljan, D. J. Sullivan, T. Sumi, M. Takeuti, Y. Watase, S. Wilkinson, R. Yamada, T. Yanagisawa, and P. C. M. Yock. Real-time difference imaging analysis of MOA Galactic bulge observations during 2000. *MNRAS*, 327(3):868–880, November 2001.
- [174] Seung-Lee Kim, Chung-Uk Lee, Byeong-Gon Park, Dong-Jin Kim, Sang-Mok Cha, Yongseok Lee, Cheongho Han, Moo-Young Chun, and Insoo Yuk. KMTNET: A Network of 1.6 m Wide-Field Optical Telescopes Installed at Three Southern Observatories. *Journal of Korean Astronomical Society*, 49(1):37–44, February 2016.
- [175] D. Spergel, N. Gehrels, C. Baltay, D. Bennett, J. Breckinridge, M. Donahue, A. Dressler, B. S. Gaudi, T. Greene, O. Guyon, C. Hirata, J. Kalirai, N. J. Kasdin, B. Macintosh, W. Moos, S. Perlmutter, M. Postman, B. Rauscher, J. Rhodes, Y. Wang, D. Weinberg, D. Benford, M. Hudson, W. S. Jeong, Y. Mellier, W. Traub, T. Yamada, P. Capak, J. Colbert, D. Masters, M. Penny, D. Savransky, D. Stern, N. Zimmerman, R. Barry, L. Bartusek, K. Carpenter, E. Cheng, D. Content, F. Dekens, R. Demers, K. Grady, C. Jackson, G. Kuan, J. Kruk, M. Melton, B. Nemati, B. Parvin, I. Poberezhskiy, C. Peddie, J. Ruffa, J. K. Wallace, A. Whipple, E. Wollack, and F. Zhao. Wide-Field Infrared Survey Telescope-Astrophysics Focused Telescope Assets WFIRST-AFTA 2015 Report. *arXiv e-prints*, page arXiv:1503.03757, March 2015.
- [176] J. R. Lu, E. Sinukoff, E. O. Ofek, A. Udalski, and S. Kozłowski. A Search For Stellar-mass Black Holes Via Astrometric Microlensing. *ApJ*, 830(1):41, October 2016.
- [177] N. Kains, A. Calamida, K. C. Sahu, S. Casertano, J. Anderson, A. Udalski, M. Zoccali, H. Bond, M. Albrow, I. Bond, T. Brown, M. Dominik, C. Fryer, M. Livio, S. Mao, and M. Rejkuba. Microlensing Constraints on the Mass of Single Stars from HST Astrometric Measurements. *ApJ*, 843(2):145, July 2017.
- [178] Krzysztof A. Rybicki, Łukasz Wyrzykowski, Jakub Klencki, Jos de Bruijne, Krzysztof Belczyński, and Martyna Chruślińska. On the accuracy of mass measurement for microlensing black holes as seen by Gaia and OGLE. *MNRAS*, 476(2):2013–2028, May 2018.
- [179] Kailash C. Sahu, Jay Anderson, Stefano Casertano, Howard E. Bond, Pierre Bergeron, Edmund P. Nelan, Laurent Pueyo, Thomas M. Brown, Andrea Bellini, Zoltan G. Levay, Joshua Sokol, Martin Dominik, Annalisa Calamida, Noé Kains, and Mario Livio. Relativistic deflection of background starlight measures the mass of a nearby white dwarf star. *Science*, 356(6342):1046–1050, June 2017.
- [180] A. Zurlo, R. Gratton, D. Mesa, S. Desidera, A. Enia, K. Sahu, J. M. Almenara, P. Kervella, H. Avenhaus, J. Girard, M. Janson, E. Lagadec, M. Langlois, J. Milli, C. Perrot, J. E. Schlieder, C. Thalmann, A. Vigan, E. Giro, L. Gluck, J. Ramos, and A. Roux. The gravitational mass of Proxima Centauri measured with SPHERE from a microlensing event. *MNRAS*, 480(1):236–244, October 2018.
- [181] Casey Y. Lam, Jessica R. Lu, Andrzej Udalski, Ian Bond, David P. Bennett, Jan Skowron, Przemek Mróz, Radek Poleski, Takahiro Sumi, Michał K. Szymański, Szymon Kozłowski, Paweł Pietrukowicz, Igor Soszyński, Krzysztof Ulaczyk, Łukasz Wyrzykowski, Shota Miyazaki, Daisuke Suzuki, Naoki Koshimoto, Nicholas J. Rattenbury, Matthew W. Hosek, Fumio Abe, Richard Barry, Aparna Bhattacharya, Akihiko Fukui, Hirosane Fujii, Yuki Hirao, Yoshitaka Itow, Rintaro Kirikawa, Iona Kondo, Yutaka Matsubara, Sho Matsumoto, Yasushi Muraki, Greg Olmschenk, Clément Ranc, Arisa Okamura, Yuki Satoh, Stela Ishitani Silva, Taiga

- Toda, Paul J. Tristram, Aikaterini Vandorou, Hibiki Yama, Natasha S. Abrams, Shrihan Agarwal, Sam Rose, and Sean K. Terry. Supplement: “An Isolated Mass-gap Black Hole or Neutron Star Detected with Astrometric Microlensing” (2022, ApJL, 933, L23). ApJS, 260(2):55, June 2022.
- [182] Kailash C. Sahu, Jay Anderson, Stefano Casertano, Howard E. Bond, Andrzej Udalski, Martin Dominik, Annalisa Calamida, Andrea Bellini, Thomas M. Brown, Marina Rejkuba, Varun Bajaj, Noé Kains, Henry C. Ferguson, Chris L. Fryer, Philip Yock, Przemek Mróz, Szymon Kozłowski, Paweł Pietrukowicz, Radek Poleski, Jan Skowron, Igor Soszyński, Michał K. Szymański, Krzysztof Ulaczyk, Łukasz Wyrzykowski, Richard K. Barry, David P. Bennett, Ian A. Bond, Yuki Hirao, Stela Ishitani Silva, Iona Kondo, Naoki Koshimoto, Clément Ranc, Nicholas J. Rattenbury, Takahiro Sumi, Daisuke Suzuki, Paul J. Tristram, Aikaterini Vandorou, Jean-Philippe Beaulieu, Jean-Baptiste Marquette, Andrew Cole, Pascal Fouqué, Kym Hill, Stefan Dieters, Christian Coutures, Dijana Dominis-Prester, Clara Bennett, Etienne Bachelet, John Menzies, Michael Albrow, Karen Pollard, Andrew Gould, Jennifer C. Yee, William Allen, Leonardo A. Almeida, Grant Christie, John Drummond, Avishay Gal-Yam, Evgeny Gorbikov, Francisco Jablonski, Chung-Uk Lee, Dan Maoz, Ilan Manulis, Jennie McCormick, Tim Natusch, Richard W. Pogge, Yossi Shvartzvald, Uffe G. Jørgensen, Khalid A. Alsubai, Michael I. Andersen, Valerio Bozza, Sebastiano Calchi Novati, Martin Burgdorf, Tobias C. Hinse, Markus Hundertmark, Tim-Oliver Husser, Eamonn Kerins, Penelope Longa-Peña, Luigi Mancini, Matthew Penny, Sohrab Rahvar, Davide Ricci, Sedighe Sajadian, Jesper Skottfelt, Colin Snodgrass, John Southworth, Jeremy Tregloan-Reed, Joachim Wambsganss, Olivier Wertz, Yiannis Tsapras, Rachel A. Street, D. M. Bramich, Keith Horne, Iain A. Steele, and RoboNet Collaboration. An Isolated Stellar-mass Black Hole Detected through Astrometric Microlensing. ApJ, 933(1):83, July 2022.
- [183] Klüter, J., Bastian, U., and Wambsganss, J. Expectations on mass determination using astrometric microlensing by gaia. *A&A*, 640:A83, 2020.
- [184] I-Kai Chen, Marius Kongsore, and Ken Van Tilburg. Detecting Dark Compact Objects in Gaia DR4: A Data Analysis Pipeline for Transient Astrometric Lensing Searches. *arXiv e-prints*, page arXiv:2301.00822, January 2023.
- [185] F. Delplancke, K. M. Górski, and A. Richichi. Resolving gravitational microlensing events with long-baseline optical interferometry. Prospects for the ESO Very Large Telescope Interferometer. *A&A*, 375:701–710, August 2001.
- [186] Klüter, J., Bastian, U., Demleitner, M., and Wambsganss, J. Prediction of astrometric microlensing events from gaia dr2 proper motions. *A&A*, 620:A175, 2018.
- [187] Leonidas Moustakas, Matthew O’Dowd, Timo Anguita, Rachel Webster, George Chartas, Matthew Cornachione, Xinyu Dai, Carina Fian, Damien Hutsemekers, Jorge Jimenez-Vicente, et al. Astro2020 science white paper-quasar microlensing: Revolutionizing our understanding of quasar structure and dynamics. *arXiv preprint arXiv:1904.12967*, 2019.
- [188] Marie Treyer and Joachim Wambsganss. Astrometric microlensing of quasars-dependence on surface mass density and external shear. *Astronomy & Astrophysics*, 416(1):19–34, 2004.
- [189] Walsh Dennis, Robert F Carswell, and Ray J Weymann. 0957+561 a, b: twin quasistellar objects or gravitational lens? *Nature*, 279(5712):381–384, 1979.
- [190] John Huchra, Marc Gorenstein, Stephen Kent, Irwin Shapiro, Graeme Smith, Edward Horine, and Richard Perley. 2237+ 0305: A new and unusual gravitational lens. *The Astronomical Journal*, 90:691–696, 1985.
- [191] CS Kochanek. Quantitative interpretation of quasar microlensing light curves. *The Astrophysical Journal*, 605(1):58, 2004.
- [192] Naohisa Inada, Masamune Oguri, Robert H Becker, Min-Su Shin, Gordon T Richards, Joseph F Hennawi, Richard L White, Bartosz Pindor, Michael A Strauss, Christopher S

- Kochanek, et al. The sloan digital sky survey quasar lens search. ii. statistical lens sample from the third data release. *The Astronomical Journal*, 135(2):496, 2008.
- [193] Ana M Mosquera and Christopher S Kochanek. The microlensing properties of a sample of 87 lensed quasars. *The Astrophysical Journal*, 738(1):96, 2011.
- [194] Masamune Oguri and Philip J Marshall. Gravitationally lensed quasars and supernovae in future wide-field optical imaging surveys. *Monthly Notices of the Royal Astronomical Society*, 405(4):2579–2593, 2010.
- [195] M Jaroszynski, J Wambsganss, and B Paczynski. Microlensed light curves for thin accretion disks around schwarzschild and kerr black holes. *The Astrophysical Journal*, 396:L65–L68, 1992.
- [196] Kevin P Rauch and Roger D Blandford. Microlensing and the structure of active galactic nucleus accretion disks. *The Astrophysical Journal*, 381:L39–L42, 1991.
- [197] Joachim Wambsganß, B Paczynski, and Peter Schneider. Interpretation of the microlensing event in qso 2237+ 0305. *The Astrophysical Journal*, 358:L33–L36, 1990.
- [198] RL Webster, AMN Ferguson, RT Corrigan, and MJ Irwin. Interpreting the light curve of q2237+ 0305. *The Astronomical Journal*, 102:1939–1945, 1991.
- [199] L. L. R. Williams and P. Saha. Improper Motions in Lensed QSOs. *AJ*, 110:1471, October 1995.
- [200] Geraint F Lewis and Rodrigo A Ibata. Quasar image shifts resulting from gravitational microlensing. *The Astrophysical Journal*, 501(2):478, 1998.
- [201] R Kayser, S Refsdal, and R Stabell. Astrophysical applications of gravitational micro-lensing. *Astronomy and Astrophysics*, 166:36–52, 1986.
- [202] Xiaohui Fan, Feige Wang, Jinyi Yang, Charles R Keeton, Minghao Yue, Ann Zabludoff, Fuyan Bian, Marco Bonaglia, Iskren Y Georgiev, Joseph F Hennawi, et al. The discovery of a gravitationally lensed quasar at $z = 6.51$. *The Astrophysical Journal Letters*, 870(2):L11, 2019.
- [203] A. M. Ghez, B. L. Klein, M. Morris, and E. E. Becklin. High proper-motion stars in the vicinity of sagittarius a*: Evidence for a supermassive black hole at the center of our galaxy. *The Astrophysical Journal*, 509(2):678, dec 1998.
- [204] A. M. Ghez, S. Salim, N. N. Weinberg, J. R. Lu, T. Do, J. K. Dunn, K. Matthews, M. R. Morris, S. Yelda, E. E. Becklin, T. Kremenek, M. Milosavljevic, and J. Naiman. Measuring Distance and Properties of the Milky Way’s Central Supermassive Black Hole with Stellar Orbits. *ApJ*, 689(2):1044–1062, December 2008.
- [205] S. Gillessen, F. Eisenhauer, S. Trippe, T. Alexander, R. Genzel, F. Martins, and T. Ott. Monitoring Stellar Orbits Around the Massive Black Hole in the Galactic Center. *ApJ*, 692(2):1075–1109, February 2009.
- [206] Marios Galanis et al. In preparation, 2023.
- [207] Kip S. Thorne and Roger D. Blandford. *Modern Classical Physics*. Princeton University Press, Princeton, NJ, 2017.